UNIVERSIDAD COMPLUTENSE DE MADRID
FACULTAD DE CIENCIAS FÍSICAS
DEPARTAMENTO DE ÓPTICA

TESIS DOCTORAL

Light harvesting using photonic crystals for photovoltaic applications

Recolección de luz mediante cristales fotónicos para aplicaciones fotovoltaicas

MEMORIA PARA OPTAR AL GRADO DE DOCTOR

PRESENTADA POR

Jerónimo Buencuerpo Fariña

DIRECTORES

José M. Llorens Montolio
María Luisa Dotor Castilla
José María Ripalda Cobián

Madrid, 2017

UNIVERSIDAD COMPLUTENSE DE MADRID

FACULTAD DE CIENCIAS FÍSICAS

Departamento de Óptica

TESIS DOCTORAL

Recolección de luz mediante cristales fotónicos para aplicaciones fotovoltaicas

Light harvesting using photonic crystals for photovoltaic applications

MEMORIA PARA OPTAR AL GRADO DE DOCTOR

PRESENTADA POR

Jerónimo Buencuerpo Fariña

Directores

José M. Llorens Montolio

María L. Dotor Castilla

José M. Ripalda Cobián

Madrid (España), 2016

A María, y a mi familia.

Agradecimientos

Llegado el momento de depositar, el último paso es siempre poner los agradecimientos. El último clavo que apuntala la época que en la que has estado realizando la tesis. La situación emocional que puede esperar uno es euforia, pero a la vez hay incertidumbre, ya que durante estos años todos tus esfuerzos, desvelos y preocupaciones giraban en torno a la finalización de este proyecto. Ahora sientes alivio y cautela hacia los nuevos retos que te puedas encontrar. Al fin y al cabo, las páginas de agradecimientos recuerdan mucho a despedida.

Durante el tiempo de la tesis, las relaciones laborales se suelen convertir en relaciones cercanas, y llegado el final, te das cuenta de que has llegado hasta aquí no sólo porque te apoyes en *hombres de gigantes*, sino por el apoyo más directo que has recibido es el de las personas que te rodean. Esas personas van desde tu pareja, familiares, directores de tesis, amigos y compañeros hasta gente incluso que no pensabas que te podrían haber ayudado en ciertos momentos.

Quisiera dar mi especial agradecimiento a Ripalda por haberme inculcado que la ciencia es en si siempre el objetivo. También querría agradecer a Marisa su resolución y confianza en los retos experimentales a los que me he enfrentado. Por último, querría agradecer a Llorens haberme inculcado esa rigurosidad en el pensamiento analítico que le caracteriza. Esta tesis no sería la misma sin esa escuela que me han inculcado, y tengo claro que es algo muy importante que agradecer.

También agradezco mucho a mi familia, a mi padre por haberme apoyado todos estos años en que hiciese *lo que me gusta*, mi hermana por siempre endulzar mi carácter, no pocas veces agrio y a mi madre por inculcarme el valor de la ciencia y la academia en la sociedad. Realmente estudiar y dedicarme a la ciencia es algo que he podido realizar gracias a ellos. Por otro lado, no puedo desligar estos años

de todo el apoyo que he recibido siempre de mi compañera y *contraria*, María, que creo es la segunda persona que más se ha desvelado y sufrido con esta tesis, después del que escribe. Siempre ha sido más comprensiva y generosa de lo que yo merecía, y no puedo más que agradecérselo.

Hacer la tesis requiere de muchas horas, y esas horas agradezco haber estado en tan buena compañía de los que fueron mis compañeros de mi primer despacho Ryu, Lukasz, Luis, David. Polonia siempre será un buen recuerdo de estos años. También quisiera agradecer esos momentos de buena conversación con Mario, Alicia, Andrés y Joselo. No puedo olvidarme tampoco de Jesús, Iván y Fuster que siempre estaban ahí cuando se les necesitaba. También quisiera agradecer a Benito, Fernando, Yolanda y Luisa por haberme mostrado muchas veces el camino correcto.

No querría dejar de nombrar a otros becarios del IMM como Valerio, Malvar, Bego, Marta, Estela, Miguel, Jaime Andrés, Pedro, Diana, Blanca, Etor y otros tantos. También a las técnicos del instituto Raquel, Lorena y Carmen con las que ha sido un placer colaborar y compartir los tiempos muertos del laboratorio. Tampoco puedo olvidarme tanto de Margarita por su maravillosa acidez que la hace una persona digna con la que discutir, como de la candidez y bondad de Manuel, que siempre esta ahí demostrando cada día su buen hacer. También a Antonio por esos momentos de discusión amenos en el patio y Olga con la que ha sido un placer colaborar. En general el IMM ha sido mi casa todos estos años, y puedo decir que he aprendido mucho de todas las personas que trabajan en el.

Por último querría agradecer a mis amigos, Gabriel, Andrés, Cristian y Javier por estar siempre ahí desde que empecé mis estudios en física, como a todo mis amigos de *tribunal populo* que me han aguantado y apoyado durante estos años.

Por último decir que *son todos los que están, pero no están todos los que son.*

Contents

Resumen

Las células fotovoltaicas basan su funcionamiento en el atrapamiento eficiente de luz para su posterior conversión en energía eléctrica mediante la separación de cargas. Habitualmente, los sistemas usados para minimizar las perdidas por fotones no absorbidos se basan en láminas delgadas interferenciales y/o en aumentar el espesor del medio activo. En los últimos años dentro de la comunidad fotovoltaica existe un interés creciente en usar diversos tipos de nanoestructuras para aumentar la eficiencia, ya sea minimizando la reflexión o aumentando la absorción. Estas técnicas son conocidas como *light-trapping* o de atrapamiento de luz.

El uso de nanostructuras ópticas periódicas, es decir cristales fotónicos, puede ser muy beneficioso frente a las laminas interferenciales convencionales y así justificar las posibles desventajas derivadas de necesitar una fabricación más compleja. De hecho, los cristales fotónicos presentan una mayor flexibilidad a la hora de diseñar la respuesta óptica del sistema: reflexión, transmisión y absorción. Esto permite mejorar la eficiencia, ya sea reduciendo la reflexión del sistema y/o incrementando la absorción mediante el aumento del camino óptico efectivo.

Esta tesis se centra en el diseño de cristales fotónicos para células basadas en materiales III-V. Estos materiales son los que alcanzan una mayor eficiencia en la conversión de luz a electricidad. Existe un alto interés en mejorar la ya de por si elevada eficiencia de esta tecnología, con el objetivo de reducir el coste de la electricidad producida en terminos de kWh/$. Una característica importante a tener en cuenta es que estos materiales son usados de forma habitual en sistemas ópticos de concentración, con la consecuencia de que la superficie de la capa semiconductora puede reducirse tres ordenes de magnitud con respecto a la de módulos convencionales. Esto obviamente abarata el coste de introducir nanoestructuras en el proceso de fabricación.

Como es habitual, en el Capítulo 1 se hace una introducción de los fundamentos y la motivación del uso de cristales fotónicos en células fotovoltaicas. El resto de la tesis esta organizada en cuatro capítulos presentando los resultados publicados, un capítulo de conclusiones y dos apéndices detallando los métodos utilizados. En este resumen se presenta una sinopsis de cada capítulo.

En el Capítulo 2, mediante cálculos numéricos, se muestra que usando cristales fotónicos ya sea en la parte frontal y/o en la parte posterior de una célula de arseniuro de galio (GaAs) bajo concentración se consigue en el mejor de los casos un incremento de un 1 % en eficiencia con respecto a una estructura convencional. Este diseño es novedoso frente a la mayoría de las propuestas de la literatura ya que la nanostructura está en las capas adyacentes a la capa activa. Evitar nanostructurar la capa activa previene que incremente la recombinación en la superficie de la nanostructura, y hace que este diseño sea más compatible con los dispositivos actuales.

Las estructuras en la parte trasera incrementan la fotocorriente, pero aparece una penalización en el voltaje. En cambio, las estructuras en la parte frontal incrementan la fotocorriente pero no presentan esta disminución en el voltaje. El tamaño de las estructuras óptimas en la parte frontal es tal que se beneficia de tener un periodo más pequeño que la longitud de onda mínima del rango espectral utilizado, pero lo suficientemente grande para permitir el confinamiento de luz y el aumento de camino óptico dentro del sustrato de mayor índice de refracción. Esta regla de diseño es utilizada en el Capítulo 3 como punto de partida.

El Capítulo 3 se centra en diseñar un anti-reflectante nanoestructurado para células solares tándem. Estas células utilizan la mayor parte del espectro solar, lo que representa un reto a la hora de minimizar las perdidas por reflectividad. La estructura optimizada para minimizar la reflexión esta inspirada en el ojo de una polilla (*moth-eye*) y es por ello que consta de conos nanométricos dispuestos en una red periódica. Esta estructura se caracteriza por absorber eficientemente la luz, dado que las polillas son generalmente nocturnas. Obviamente, la estructura propuesta presenta grandes cambios con respecto a la encontrada a la naturaleza. Esto es debido a que las condiciones de operación son distintas en los dos casos, fundamentalmente el sustrato usado en una tandem tiene un mayor indice de refracción que el que puede tener el ojo del insecto. Esto dificulta en gran medida

el acoplo luz desde el medio incidente.

La estructura optimizada tiene un diseño sencillo de dos capas, con sólo una de ellas nanoestructurada parcialmente. Este diseño tiene una transmisión del 99 % del espectro (1 % en perdidas por reflectividad y absorción de la capa anti-reflectante). En comparación, una capa interferencial estándar tiene una transmisión de un 95.5 %. Por otro lado, la superioridad de la nanoestructura frente a la capa interferencial se mantiene para ángulos de incidencia fuera de la normal. Esta mejora de la transmisión es resultado de la combinación de los efectos de índice gradual y al confinamiento parcial de la luz en el dieléctrico, que es un efecto puramente fotónico. Éste hallazgo, sustenta la idea de que el camino hacia mejorar la transmitividad de estas capas debe estar basado en la combinación de efectos 3D, como los modos fotónicos del cristal, con efectos 1D como lo es el índice gradual. Por otro lado, cabe destacar que esta nanoestructura es capaz de aumentar el camino óptico efectivo dentro de la célula pudiendo permitir en un futuro adelgazar las capas activas de la célula.

En el Capítulo 4 demostramos la viabilidad de la nanoestructura diseñada en el capítulo anterior. Se realiza una fabricación de esta nanoestructura en el laboratorio, usando tecnologías compatibles con la industria: litografía interferométrica láser y ataque por plasma reactivo. La estructura fabricada no ideal, reduce las pérdidas por reflectividad a tan sólo un 1.4 % para el rango espectral en el que trabaja una célula de GaAs (400-870 nm). Esto representa un 15 % de mejora relativo frente a haber utilizado un anti-reflectante estándar. Si consideramos un rango más amplio de longitudes de onda (400-1800 nm), esta estructura puede reducir las pérdidas por reflectividad a tan sólo un 3.1 %, (un 31 % de mejora frente a la lamina interferencial estándar) demostrando el potencial de este diseño. En cualquier caso, el diseño utilizado puede alcanzar mejores resultados con un mayor control de las tecnologías de fabricación.

En el último capítulo, 5, se explora el uso de estas nanoestructuras para tecnologías fotovoltaicas no convencionales como es el caso de una célula termo-iónica asistida por una capa semiconductora. En este capítulo se combinan las estructuras de los Capítulos 2 y 3 para incrementar la absorción y actuar como anti-reflectante de la lamina semiconductora. La tecnología de estos dispositivos no esta tan avanzada como en el caso de las células convencionales, por ello en este capítulo se

exploran las posibles mejoras mediante modelos analíticos de absorción aparte de los numéricos. El análisis analítico de la absorción demuestra que la viabilidad de este dispositivo pasa por atrapar la luz eficazmente en capas ultrafinas de menos de 100 nm.

Finalmente en el Capítulo 6 se presentan las conclusiones finales y una perspectiva global de los resultados.

En los Apéndices A y B se detallan respectivamente los métodos experimentales y los métodos numéricos utilizados en esta tesis. En concreto durante su desarrollo se diseño y realizó un montaje experimental de litografía interferométrica de bajo coste (Apéndice A.1), que sirvió para la fabricación mostrada en el Capítulo 4.

En resumen, esta tesis se centra en diseñar, analizar y fabricar estructuras fotónicas para tecnologías fotovoltaicas basadas en materiales III-V.

Summary

Photovoltaic solar cells base their operation on the efficient light absorption and the subsequent conversion into electricity by separation of electric charges. Generally, solar cells use interferencial layers and/or thick absorbers to minimize the optical losses. In recent years, the photovoltaic community has a growing interest in using various types of nanostructures to increase the efficiency, minimizing either the reflectivity and/or increasing the absorption. These techniques are known as light trapping. The use of nanostructures with periodic permittivity, i.e. photonic crystals, can be very beneficial compared to the conventional interferential layers and this enhancement justifies the possible disadvantage of requiring a more complex fabrication. Indeed, photonic crystals have great flexibility in designing the optical response of a system, namely the reflection, transmission and absorption. This flexibility allows to improve efficiency, either by reducing the reflection of the cell and/or increasing the absorption by increasing the effective optical path.

This thesis focuses on the design of photonic crystals for III-V solar cells. These cells achieve the greatest efficiency in converting light to electricity. There is a high interest in improving the already high efficiency to reduce the cost of the produced electricity in terms of kWh/$. These materials are generally used with optical concentration systems, with the consequence that the surface of the semiconductor layer can be reduced three orders of magnitude in comparison to conventional solar cells. This factor obviously lowers the cost of using nanostructures in concentration technology.

As usual, in Chapter 1 an introduction to the motivation and fundaments of using photonic crystals in photovoltaics is made. The rest of the thesis is organized into four chapters presenting the results, a conclusion chapter and two appendices detailing the methods used. This summary provides an overview of each chapter presented.

In Chapter 2 we have modeled gallium arsenide solar cell (GaAs) under concentration and we have introduced the photonic crystals in the analysis. By using either photonic crystals on the front and/or back of cell an increase of 1% in efficiency is achieved in the best case compared to a conventional device. The novelty of this design against most of the proposals in the literature is that the nanostructure is in the adjacent layers to the active layer. Avoiding nanostructuring the active layer prevents an increase in charges recombination on the surface of the nanostructure, and it makes this design more compatible with existing devices. The optimal structures at the back increase the photocurrent, but a penalty on the voltage appears, whereas the front structures introduce also an increase in the photocurrent but without a reduction on voltage. The size of the front nanostructure benefits from having a smaller lattice parameter than the minimum wavelength of the spectral range used, but having a period large enough to allow light confinement and increasing the optical path within the substrate with higher refractive index. This design rule is used in Chapter 3 as starting point.

Chapter 3 focuses on designing an anti-reflective coating for a tandem solar cell. These cells use most of the solar spectrum, which represents a challenge when minimizing the reflection losses. The structure optimized is inspired in nature, the moth eye. It is composed by cones peridically distributed. This structure is characterized by efficiently absorbing light, since moths need to see at night. Obviously, the structure proposed has major changes from the one found in nature. This is because the operating conditions are quite different in the two cases, in particular the substrate used in a III-V tandem has a higher refractive index than the one that can be found inside the eye of the insect. This greatly hinders coupling light from the incident medium to the semiconductor. The final optimized structure has a simple design of two layers, with only one partially nanostructured. This design has a transmission spectrum 99% (1% losses due to the reflectivity and absorption of the anti-reflective layer). In comparison, an standard interferential layer has a transmission of 95.5%. Furthermore, the superiority of the nanostructure against interferential layer is maintained for angles out of the normal direction. This improvement in the transmission is result of combining graded index effects effects and light confinement in the dielectric, which is a purely photonic effect. These findings support the idea that the best way to improve the transmissivity of these layers must be based on the combination of 3D effects, such as the photonic

crystal eigenstates, with 1D effects like the graded index. Also, this nanostructure is able to increase the effective optical path within the cell, so it may allow in the future to thin the active layers of the cell.

In Chapter 4 we demonstrate the viability of the nanostructure designed in the previous chapter. The nanostructure fabrication is done in the laboratory, using compatible technologies with the industry, as the laser interferometric lithography and reactive ion etching. The reflectivity of the structure made achieves a loss of only 1.4% for the spectral range of GaAs cell (400-870 nm). This represents an improvement on 15% versus the standard anti-reflective coating. If we considered a wide spectrum (400-1800 nm), this nanostructure attains a reflectivity loss of only 3.1%, (31% improvement over standard interferential coating) demonstrating the potential of this design. In any case, the design used can achieve better results (1% optical loss) with further optimization of the fabrication process, as shown in Chapter 3.

In the last chapter, Chapter 5, these nanostructures are used for a non conventional photovoltaic technology such as the photo-enhanced thermo-ionic cell. In particular we have combined the structures from Chapter 2 and Chapter 3 and optimize to this device. The technology of these devices is not as advanced as in the case of conventional cells, so in this chapter we explore possible improvements by analytical models apart from the fully numerical models. The analytic studies show that the viability of this device requires that the device must effectively absorb light using ultra-thin layers with less than 100 nm.

Finally, in Chapter 6 the final conclusions and outlook of the results are presented.

In the Appendix A and Appendix B the experimental methods and numerical methods used in this thesis are detailed. In particular, in Appendix A.1 the laser interferometric lithography setup built for fabricating the nanostructures of Chapter 4 is detailed.

In summary, this thesis focuses on design, analysis and fabrication of photonic crystals for photovoltaic technologies based on III-V materials.

Chapter 1

Introduction

1.1 Solar energy outlook

In the following decades the global population is expected to rise from 7000 million people in 2015 to 8500 million by 2030.[1] Also, it is foreseen that the comforts of modern society will expand to high population countries as India or China. As a consequence, the energy demand will increase exponentially. To solve the problem, we should not rely on oil/carbon for the forthcoming years, as we would surely increase the CO_2 emissions and the air pollution. Also, we should not depend on nuclear energy because it represents a perilous road, as demonstrated by accidents like Fukushima or Chernobyl. Therefore, if we want to maintain and improve our way of life as an modern society, renewable energies are completely necessary. Photovoltaics represents one of the technologies with more potential to support the increasing energy demand. In fact, one of the advantages of solar cells is its availability: the sun radiation is present over the whole globe, see Fig. 1.1. As a consequence, the energy can be produced next to the demand, even for remote areas. A typical single family home with 100 m^2 requires around 10 m^2 of solar panels to satisfy its energy demand. But photovoltaics is also suitable for large scale production, and several solar plants with capacity over 500 MW are in operation.[2–4]

The first functional PV device was made by Fritts in 1883.[6] Although, the modern semiconductor p-n junction solar cell can be attributed to Bell Labs works in the 1950s, when they introduced a silicon solar cell with 6% efficiency.[7] Photovoltaics has been under heavy development since then.[8, 9]. In most cases,

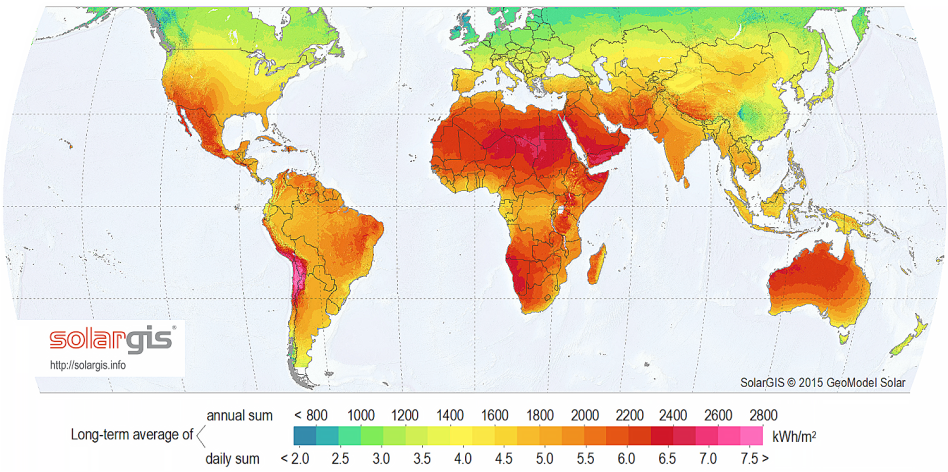

Figure 1.1: Global solar radiation map from SOLARGIS[5]

quantitative performance metrics of advanced technologies increase monotonically with accumulated production. This is known as the *learning curve*, the most famous example being Moore's law for transistor density as a function of time. [10–12] In most cases, decades pass before a new technology reaches a level of maturity that makes it competitive with well established technologies. Nowadays, with initial investment costs of the order of 1$/Watt.[12, 13], photovoltaics starts to be competitive with other energy sources, like fossil fuels.

Thermodynamics will of course limit the efficiency in the process of obtaining work, i.e. electricity. In this Carnot cycle the sun is the hot source (6000 K approx.) and the solar cell is the cold sink (300 K approx.). Under these conditions the upper limit of the efficiency is 95%. But more stringent limits are set by the details of the energy conversion mechanism inside a photovoltaic diode. We have to consider the semiconductor energy gap, the absorptivity and emissivity, the recombination processes, and the diode equation in order to calculate the so called detailed balance efficiency limit. This was done by Shockley and Queisser in their seminal paper, Ref. [14]. They established an upper limit of 30% for a single junction solar cell without optical concentration. Afterwards, equivalent limits were established for multijunction devices, namely multiple gaps, increasing the upper limit to 86.8%. [15, 16] The Shockley-Queisser limit is derived for a single gap semiconductor and it plays a vital role in photovoltaics, as it helps to understand the fundamental

losses in a photovoltaic device.

1.2 Shockley-Queisser limit

Except for a few atmospheric absorption bands, the spectrum from the sun resembles that of an ideal blackbody at 5760 K. Photon absorption within the semiconductor will create electron-hole pairs that can be used to generate work by extracting the charge carriers through charge polarity selective contacts. One of the fundamental loss mechanisms is due to photons with energy higher than the bandgap generating electron hole pairs that will thermalize to the band edges; whereas the photons with energy lower than the bandgap will not be absorbed in the active part of the device. Using these conditions, we can establish an ultimate efficiency for a single junction:

$$\begin{aligned} \mathcal{U} &= E_g \, Q_s / P_s = \\ &= E_g \frac{2\pi}{hc^3} \int_{E_g}^{\infty} \frac{E^2}{\exp(E/kT_s) - 1} \mathrm{d}E \Big/ \int_0^{\infty} \frac{E^3}{\exp(E/kT_s) - 1} \mathrm{d}E, \end{aligned} \tag{1.1}$$

being P_s the total number of incident photons from the sun, Q_s the number of quanta of energy from the sun greater than E_g, i.e. the energy bandgap, T_s the temperature of the sun (5760 K) and k the Boltzmann constant. This is the so called *ultimate efficiency*. It is maximum for a band gap of 1.1 eV yielding an efficiency of a 44 %. Yet, we have not introduced the temperature of our solar cell, and therefore, this limit will be only true for an ideal cell at 0 K.

Introducing the temperature of the solar cell will also add two processes to the analysis: the non-radiative and radiative recombination of charges. For the sake of simplicity, we will assume that the non-radiative recombinations are avoidable, and therefore will not appear in the upper limit. On the other hand, the radiative recombinations are unavoidable in this upper limit as the solar cell at some temperature will be another blackbody itself. The radiation upon and from the solar cell will subtend different solid angles and as a consequence we have to introduce a geometrical factor f_i. This factor will be $f_w = 2.18\ 10^{-5}$ for radiation from the sun without concentration and f_c=1 for radiation from the solar cell.

Following the notation of Ref. [14], we introduce the photon fluxes:

$$F_i = A_i f_i(\theta) Q_i(T, E, \theta) \simeq A_i f_i Q_i(T, E), \tag{1.2}$$

A_i being the area of emission/absorption of the solar cell: A the surface collecting photons and $2A$ the emitter surface. Also, we will assume that the radiation flux, Q_i is constant with θ for simplicity, but this is not constant in general, as detailed in Chapter 2. From Eq. (1.2) the sun photon flux is:

$$F_\mathrm{s} = A f_\mathrm{w} Q_\mathrm{s}(T_\mathrm{s}, E), \tag{1.3}$$

and the flux from the solar cell surface at equilibrium:

$$F_\mathrm{c0} = 2A f_\mathrm{c} Q_\mathrm{s}(T_\mathrm{s}, E). \tag{1.4}$$

At this point, we have to introduce the diode physics in the limits to obtain the photon fluxes and current from the solar cell out of equilibrium. We introduce the diode equation for the current without illumination:

$$I_\mathrm{dark} \equiv I_0(1 - \exp(qV/kT_\mathrm{c})) = qF_\mathrm{c0}(1 - \exp(qV/kT_\mathrm{c})), \tag{1.5}$$

where we have assumed that the charge densities (n, p, n_i) follows a Maxwell distribution, $F_\mathrm{c}(V) = F_\mathrm{c0} np/n_i^2 = F_\mathrm{c0} \exp(qV/kT_c)$.

Also, we can define the current under illumination at zero voltage, namely the short-circuit photocurrent, I_sc. The number of photogenerated charge carriers will match the absorbed photons from the sun minus the emitted photons from the cell:

$$I_\mathrm{sc} = q(F_\mathrm{s} - F_\mathrm{c0}). \tag{1.6}$$

Combining Eq.(1.5) and Eq.(1.6), we are able to obtain the photocurrent at any voltage:

$$I(V) = I_\mathrm{sc} + I_\mathrm{dark}(V). \tag{1.7}$$

From Eq. (1.7) we can choose an operation voltage, V_op that will maximize the

output power, $\max(I(V)V)$, so the efficiency will be:

$$\eta = I(V_{\mathrm{op}})V_{\mathrm{op}}/P_{\mathrm{inc}}, \tag{1.8}$$

where $P_{\mathrm{inc}} = Af_{\mathrm{w}}P_{\mathrm{s}}$, in other words the incident power over the solar cell.

Before analyzing the different strategies to increase the efficiency, it is useful to also define the open circuit voltage, substituting $I = 0$ in Eq. (1.7):

$$V_{\mathrm{oc}} = kT_{\mathrm{c}}/q \ \ln(F_{\mathrm{s}}/F_{\mathrm{c0}}). \tag{1.9}$$

Once we have obtained Eq. (1.8) we can start to analyze the optical losses of a solar cell. Overall, we have assumed that the absorption is perfect, and obviously this is not realistic. The absorption will limit the photon flux usable by the solar cell, and therefore mainly affects the short circuit photocurrent. The incident photon flux can be increased using an optical concentrator, namely $f_{\mathrm{w},X} = Xf_{\mathrm{w}}$, where X is the concentration factor. The photocurrent will increase $\propto X$ whereas voltage will increase $\propto \log(X)$, as can be seen in Eq. (1.6) and Eq. (1.9), respectively. Increasing F_{s} using concentration increases the efficiency of the solar cell because the concentration factor does not affect F_{c0}, as f_{c} remains the same independently of X. This way, we are modifying the ratio between geometric factors, which boils down to the fact that the area collecting light from the sun and the area of the solar cell are not the same anymore. Maximum concentration is mathematically similar to what we would obtain if we were able to redirect the emitted and/or the incident light so that the emission cone from the solar cell is the same as the incident cone.

From Fig. 1.2 we could see the how the different strategies affect the efficiency. The absorption obviously plays a decisive role in a photovoltaic device, whereas by using concentrator systems or photon recycling schemes the efficiency can be increased above the 30%.[1]

In summary, the fundamental optical losses in a solar cell are: limited absorption

[1] One consequence of using only one semiconductor is that we are losing photons with energies below the band gap. Also, the photons with energy above the band gap, that will be absorbed, will thermalize. In other words, the left-over energy will be lost as heat. Still, this can be effectively reduced using tandem solar cells, namely combining more than one semiconductor, and therefore band-gaps, as its explained in [16].

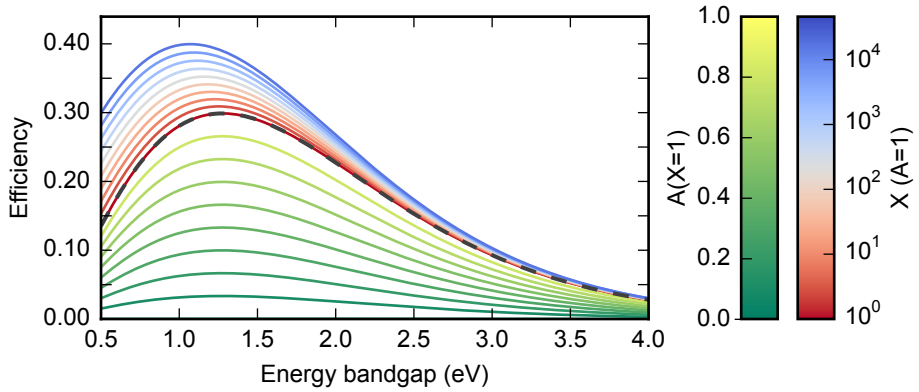

Figure 1.2: Efficiency of a solar cell (T_c = 300 K) under illumination (T_s = 5760 K) as a function of the energy bandgap. From green to yellow, the efficiency is calculated as a function of the absorption without concentration (X=1). From red to blue the efficiency is calculated as a function of the concentration factor (X), with perfect absorption (A=1). The efficiency at X=1 and A=1 is the black dashed line.

and emission losses. To minimize the former we will need to design structures capable of reducing the reflectivity while increasing the absorption in the semiconductor, whereas, the latter can be effectively mitigated by using concentrators.

Non-radiative recombinations such as Shockley-Read-Hall recombination [17, 18] or Auger recombination [19] were not taken into account in the previous calculation. It may be desirable to minimize bulk non-radiative recombination, by using a thin film device. But, the absorber thickness will reduce the absorption, as it is expected by the Beer-Lambert law. However, absorption can be increased in such thin absorbers by using nanostructures [20, 21] which is in fact, one advantage of using photonic crystals [22].

1.3 Molding the flow of light: Photonic crystals

One possibility to tweak the response of an optical layer is to generate a periodic distribution of the dielectric permittivity, i.e. use a photonic crystal [23, 24]. A 1D-photonic crystal is for example a Bragg reflector, where the dielectric media is

periodic along one direction. The effects of a 2D photonic crystal are markedly different for light propagating in the crystal plane or perpendicularly to it, in which case the structure can be understood as a diffraction grating. Examples of 3D photonic crystals are opals and wood piles.[25] The periodic distribution of permittivities impose boundary conditions in the Maxwell equations and as a consequence the dispersion of the light waves would be different from that in a homogeneous medium, i.e. the wave vector to frequency relation is not simply a inverse relationship. Indeed, we can engineer energy band gaps where the photons cannot propagate, as in the Bragg reflector, or design flat bands so that we can have *slow light* traveling through the photonic crystal.[25–27] Photonic crystals have been used typically for narrow band applications as lasers, or LEDs as they rely on the interference of waves.[28–30] It represents a challenge to use a photonic crystal in a broadband application like solar cells. Nevertheless, nanostructuring the surfaces of solar cells has been proposed several times in the literature as a promising option to increase the efficiency, the so called *light trapping*. [31–65] Two trends are clearly followed *light trapping*: (i) nanostructuring the semiconductor layers of the device [31–58], and (ii) nanostructuring the antireflective coating or the contacts.[59–65] The former is typically focused on increasing the absorption in thin film solar cells, as the high refractive index contrast in semiconductor/air nanostructures leads to intense photonic effects. [22] Generally, these works are targeting silicon or organic solar cells, as these materials are weak absorbers for energies near the band gap. The structures studied are typically simple 1D, 2D square or hexagonal diffraction gratings, namely grooves, nanopillars and nanoholes [31–48], locally disordered structures[51–53], and quasi-random structures [54, 55]. On the other hand, the second trend, focused on nanostructuring the contacts or the antireflective coatings, generally deals with reducing the *shadow* from the contacts, or minimizing the reflectivity of the structure [59–62, 66–69]. An enhancement of the absorption is also expected when nanostructuring this outer layers of the device. In this thesis, we have mostly used the latter approach for III-V solar cells, as both the material absorptance, and surface recombination rates are high. Nevertheless, we have also used the former approach (semiconductor nanostructures) for the hybrid thermo-ionic cell presented in the last chapter, because in this particular device there is a need to minimize the thickness of the semiconductor. Apart from

these periodic structures, also random nanostructures have been proposed in the literature as homogeneous scatterers or presenting an effective gradual refractive index [70–72]. However, this type of structures have not been studied in this thesis, as we are after the understanding and fine control of the optical fluxes.

In order to minimize the optical losses in a solar cell, we must engineer the optical response of the device. Typically, two main strategies have been used in the literature:

1. Minimizing the reflectance of the solar cell by using destructive interference in multilayers,[73, 74] or a graded index layer[75, 76].

2. Increasing the optical path by using microstructures,[77–79] and/or adding a mirror at the back side.

Nanostructuring the surfaces of the solar cell presents the opportunity to engineer the optical response with more degrees of freedom than using only flat layers. The two fundamental ideas behind using nanostructures in solar cells are increasing the optical path within the active layer [20–22], and engineering the nanostructured layer effective refractive index to couple the incident light [76, 80]. The *conventional* and nanostructure based strategies are graphically illustrated on Figure 1.3.

The first step in designing the nanostructure is to obtain some general rules extracted from basic analysis. For illustrative purposes we will treat the optical response for a 2D diffraction grating with square symmetry on top of an optically thick substrate. For simplicity, the diffraction grating and the substrate have the same permittivity, ϵ_s. We can assume an incident plane wave, with frequency ω and wavevector $\mathbf{k}$:

$$\begin{aligned} \mathbf{k} &= (k_x, k_y, k_z). \\ k_x &= \omega/c \ \sin(\phi)\cos(\theta), \\ k_y &= \omega/c \ \sin(\phi)\sin(\theta), \\ k_x &= \omega/c \ \cos(\theta). \end{aligned} \tag{1.10}$$

The 2D periodic structure couples the incoming light with all Bragg harmonics of

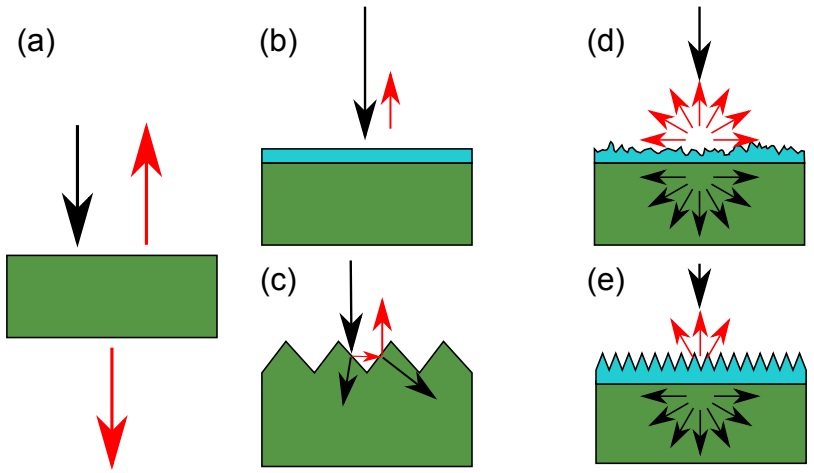

Figure 1.3: Black arrows represent input channels, whereas red arrows represent losses. (a) Simple case of a bare layer. Loses are just the reflection and the transmission at the semiconductor/air interface. (b) Interference thin film coating to minimize the reflection (c) Microstructures such as pyramids to make the rays bounce several times before reflection. (d) Random nanostructures are able to reduce the reflection and increase the absorption by the uniform distribution in angle in the incident medium and the substrate (Lambertian scattering). (e) A periodic 2D photonic crystal on top of the substrate which excites more diffraction orders in the substrate than in the incident medium. The *transmission* losses can be mitigated by using light trapping schemes, (c)-(e), which increase the optical path length. The reflectivity losses can be reduced by using subwavelength arrays in (d) and (e).

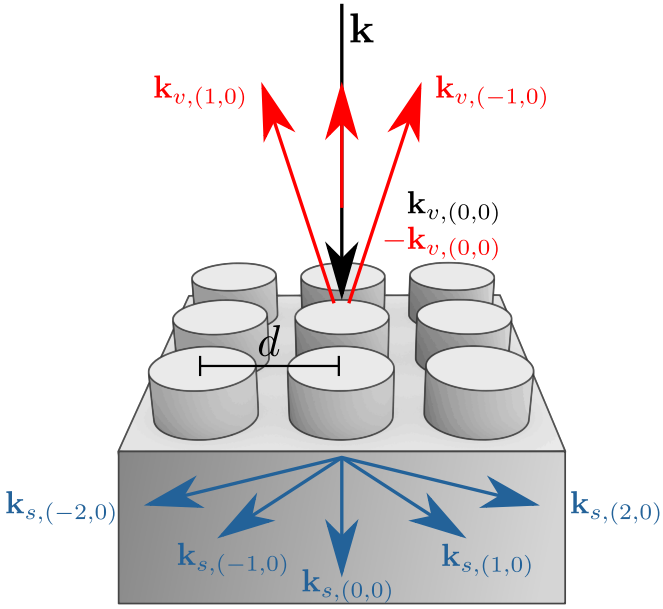

Figure 1.4: 2D Photonic crystal with lattice parameter d on top of an infinite substrate. The incoming light, $\mathbf{k}$ is diffracted by the diffraction grating. The diffraction orders $k_a(g_x, g_y)$ that are in the plane $\mathbf{k}$-$\mathbf{G}_x$, are represented in red for reflected light, and in blue for transmitted light. The diffraction orders with $G_y > 0$ are not represented.

the same frequency ω and wavevector:

$$\begin{aligned}
\mathbf{k}^{\pm}_{\mathrm{G},a} &= (k_{x,\mathrm{G}}, k_{y,\mathrm{G}}, \pm k_{z,\mathrm{G},a}).\\
k_{x,\mathrm{G}} &= k_x + G_x,\\
k_{y,\mathrm{G}} &= k_y + G_y,\\
k_{z,\mathrm{G},a} &= \sqrt{\frac{\omega^2 \epsilon_a}{c^2} - [(k_x + G_x)^2 + (k_y + G_y)^2]}.
\end{aligned} \tag{1.11}$$

where $a = v$ for vacuum and $a = s$ for the substrate, and

$$\mathbf{G} = \frac{2\pi}{d}(g_x, g_y, 0), g_x, g_y = 0, \pm 1, \pm 2, .. \tag{1.12}$$

G being the reciprocal lattice vector and d the lattice parameter. The tuple (g_x, g_y) corresponds to the diffraction orders of the diffraction grating. This model is graphically illustrated in Fig. 1.4. Using Eq. (1.11) and Eq. (1.12) we can analyze the

flow of light in the system. Indeed, analyzing k_z we can identify three regimes for $|\mathbf{G}| > 0$:

1. $k^2_{z,\mathrm{G},a=v,s} > 0$ the corresponding harmonics are purely real, which implies the light propagates in both mediums.

2. $k^2_{z,\mathrm{G},a=v,s} < 0$ the corresponding harmonics are purely imaginary, which implies the light exponentially decays in both mediums.

3. $k^2_{z,\mathrm{G},v} < 0$, $k^2_{z,\mathrm{G},s} > 0$ the corresponding harmonics are purely imaginary in vacuum but purely real in the substrate, which implies the light exponentially decays in vacuum, but propagates in the substrate.

The first condition is met when the associated diffraction orders appear in the substrate and in vacuum. Therefore, the diffraction grating can effectively modify the flow of light, and the diffracted orders within the substrate will increase the optical path length in comparison with the zero-th order ($g_x = g_y = 0$). The second condition represents the opposite, the incident wavevector is not affected by the diffraction grating, and only the zero-th order, propagates in both mediums. Nevertheless, this is not necessarily bad for our case, by tweaking the filling factor of the photonic crystal we can engineer the effective refractive index of this layer, so an interference layer design can be used for long wavelengths. The third condition is the most interesting, as light will be diffracted inside the substrate, whereas in vacuum it will be not. In this case, we will have only one channel in the incident medium, the zero-th order of the diffraction grating, and several orders in the substrate. Therefore, the incident medium will have only one loss channel, whereas the optical path will be increased in the substrate due to the diffraction orders. The first and third conditions are the most favorable for increasing the light path in the substrate, whereas the second and the third conditions are the most desirable ones to reduce the reflectivity, as we have to only adjust one *channel*. In fact, to reduce the reflectivity of the zero-th order we can optimize the layer thickness to interfere destructively as the reflected wave propagates in the same direction as the incident wave. To conclude, this reasoning leaves the third condition as the optimal for light trapping schemes. These regimens are graphically illustrated in Figure 1.5.

This analysis gives us some hints about the lattice parameter that we will need in

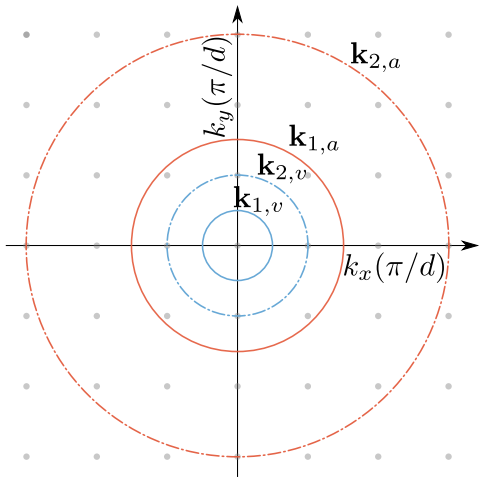

Figure 1.5: Representation of the light cones for normal incidence in the reciprocal space (μm^{-1}) for a square lattice with d=0.5μm. Light cone for $\lambda_1 = 1\mu$m,$\mathbf{k}_{1,v} = 1\mu$m^{-1} (thick lines) and $\lambda_2 = 0.5\mu$m, $\mathbf{k}_{2,v} = 2\mu$m^{-1} (dash-dotted). The diffraction orders inside each light-cone have $\mathbf{k}_z^2 > 0$, so they can propagate. Blue circles are light cones for the incident medium (air) whereas the red circles represent light cones in the substrate, n=3.

the photonic crystals for solar cells: it should be big enough to propagate diffraction orders in the substrate, although it should be small enough to avoid diffraction orders in the incident medium, to avoid opening channels that potentially can increase the reflectance.

We have explored the propagation of light in the incident medium and the substrate, but it is left out how the light propagates inside the photonic crystal itself, where the bands appear. Using an effective refractive index, the photonic crystal can be approximated as a waveguide. The dispersion relation for light propagation inside the photonic crystal can be reconstructed in the first Brillouin zone, as described in [81]. These bands represent the eigenstates of the photonic crystal and are responsible for the band gaps and the slow light phenomenon. However, we cannot generally design these bands with the analysis presented above. Generally, engineering the photonic bands is done by using numerical methods to solve the Maxwell equations in 3D, as done in Chapter 3 of this thesis.

In summary, engineering the optical response of the photonic crystal can be guided by the rule of thumb of choosing a period that is smaller than the smallest *u*seful wavelength of light in the incident medium to avoid back diffraction, but

comparable or slightly larger than the wavelength in the substrate so that there is diffraction, and therefore an increase of the optical path. The filling factor and the thickness of the photonic crystal should be chosen to maximize destructive interference of the reflections at the front and back interfaces, using the effective refractive index approximation to determine the wavelength inside the photonic crystal. Yet, designing the filling factor will affect the diffractive regime, so we must optimize globally the structure and find the right balance between the subwavelength and diffractive regimes.

1.4 Goals and overview of this thesis

The goal of this thesis is to study the possible application of photonic crystals to reduce various loss mechanisms in solar cells.

The reflection and absorption problems are addressed for a single GaAs junction in Chapter 2 and for a broadband anti-reflective coating for tandem solar cells in Chapter 3. The photonic crystals designed in Chapter 3 are fabricated and optically characterized in Chapter 4. The fabrication of the photonic crystals has been performed by an in-house laser interferometric lithography system. The design and assembly of the experimental set-up is one of the tasks of this thesis, Appendix A.1. The other experimental methods used are briefly described in Appendix A.3.

In Chapter 5 a photonic design is optimized for a hybrid between a thermal emitter and a photovoltaic system, a Photon Enhanced Thermionic Emitter.

All photonic designs are optimized using 3D models for the propagation of light, rigorous coupled-wave analysis or scattering matrix method, as described in Appendix B.

Chapter 2

Photon management for GaAs concentrator solar cells

The main motivation of this Chapter is to explore the potential of one the design trends described in the Introduction: increase the solar cell efficiency without nanostructuring the active material. For this purpose we introduce the use of front and back nanostructures to increase the efficiency of a 1 μm thick GaAs solar cell under concentration, $X = 500$ suns. Optimizing the feature sizes of dielectric nanostructures on the top (ZnS) and bottom (SiO_2) surfaces we obtain a higher efficiency (34.4%) than a similar cell with a state of the art bilayer antireflection coating and a planar mirror (33.2%). The back side nanostructure increases the photocurrent due to enhanced optical path length inside the semiconductor, while the nanostructure on the front side increases the photocurrent due to lower reflectance losses. This work was published in [68].

2.1 Introduction

Solar cells made of III-V compounds are the most efficient,[82] but still far below the Shockley-Queiser limit.[14] In the last 40 years most of the research on concentrator solar cells has been focused on increasing the quality of the semiconductor material and improving the matching of the band gaps with the solar spectrum in multijunction tandems. However, another fundamental aspect concerning the performance of a solar cell is the photon management, i.e. the optical design. Efficiency limitations related to photon management are: reflection losses, the limited absorptivity of the semiconductors, and photon reemission. Rather than nanostructuring the semiconductor active layers as in previous works found in the literature,[31, 34, 48, 83, 84] we propose to introduce dielectric nanostructures on top of concentrator solar cells, leaving the active layers intact. The results are applicable to most PV technologies, however the added cost of nano-fabrication is most advantageous in high concentration devices, where the impact of solar cell cost on the cost of the produced electricity is divided by the concentration factor.

2.2 Methods

We have used the detailed balance theory for calculating the open circuit voltage, the short circuit current, and the efficiency.[14] The Sun and the solar cell are modeled as blackbody emitters. Following the notation used by Shockley,[14] we have

$$F_{\mathrm{s}}(E,\theta,T) = \iint_0^{\theta_{\max}} dE\, d\Omega\; a(E,\theta) b(E,T) \cos(\theta)/\pi, \tag{2.1}$$

F_{s} being the total absorbed photon flux from the Sun. The incidence polar angle $\theta < \theta_{\max}$ is limited by the concentration ratio and centered around the surface normal. The blackbody spectrum $b(E,T)$ at $T = 6000$ K is used as a simplified model of solar spectrum. The solar cell is also a blackbody with thermal photon emission. The total radiative flux per unit area from the solar cell at zero bias voltage is F_{c0}, and is given by the same expression as F_{s}, but with $T = 300$ K and $\theta_{\max} = \pi/2$.

For a solar cell in equilibrium or with constant quasi-fermi levels ($\mu = qV$) within the semiconductor, the absorptance $a(E,\theta)$ is equal to the emittance $e(E,\theta)$. [85] A reduced absorptance for incident angles outside the integration range of F_s, i.e. $\theta > \theta_{max}$ reduces F_{c0} without affecting F_s, yielding a higher open circuit voltage. The absorption of one photon with energy above the semiconductor gap is assumed to produce one hole/electron pair.[1]

The photocurrent density J is given by:

$$J = J_{sc} + qF_{c0}(1 - \exp(qV/kT_c)). \tag{2.2}$$

The previous equation defines a short circuit current $J_{sc} = q(F_s - F_{c0})$, and an open circuit voltage, V_{oc}:

$$V_{oc} = \frac{kT_c}{q} \log\left(\frac{F_s - F_{c0}}{F_{c0}}\right). \tag{2.3}$$

The efficiency (η) of the solar cell, with surface A_c, is defined as the ratio between the maximum output power, P_{out}, and the incident power, P_{inc}:

$$\eta = P_{out}/P_{inc} = \frac{\max(J(V)V)A_c}{P_{inc}}. \tag{2.4}$$

Our proposal is to use dielectric periodic nanostructures and optimize their performance by calculating the resulting photocurrent, voltage, and efficiency. We have modeled a single junction GaAs solar cell with two periodic nanostructures, one made of nanostructured ZnS on the top of the semiconductor to act as antireflection layer, and another at the rear contact acting as a diffraction grating in order to achieve a light trapping system. The cases studied (Fig. 2.1) are front nanostructure only (FNO), back nanostructure only (BNO) and front and back nanostructure (FBN). These designs are more compatible with state of the art concentrator solar cell technology than previous proposals,[34, 83, 84] as nanostructuring the active layer increases surface recombination and complicates current extraction. Similarly, nanostructuring the window layer inevitably increases parasitic absorption losses, as the semiconducting materials used in window layers have much higher absorption than those used in dielectric

[1] Our calculations overestimate the photocurrent for energies above 3 eV as the absorption from the ARC is added to the absorption from the GaAs.

antireflective layers.[48]

The absorptance is calculated using the scattering matrix method,[86, 87] in particular we have used the ISU-TMM code with standard refractive index data.[88] The efficiency was maximized using a local optimization algorithm with the nanostructure dimensions as adjustable variables.[89]

2.3 Results

All modeled solar cells have a 1 μm thick GaAs active layer, a lossless mirror on the back side as back contact, and a lossless concentrator with a geometrical concentration of X = 500 suns. The reference system (Fig. 2.1(a)) has an optimized MgF_2/ZnS bilayer as antireflection coating (ARC) on the front side with thicknesses of 85.15 nm and 43.14 nm, respectively.[74] In the FNO (Fig. 2.1(b)) and FBN cases (Fig. 2.1(d)) the top nanostructure is a square lattice of ZnS nanopillars on top of a ZnS thin film with thickness d. For BNO (Fig. 2.1(c)) and FBN (Fig. 2.1(d)), the back nanostructure is a square lattice of SiO_2 nanopillars acting as diffraction grating embedded in the metallic back contact. Each nanostructure is defined by its lattice parameter a, nanopillar height h, and the radius of the nanopillars r. Other nanostructures like nanoholes and different types of lattices like triangular were also considered for the FNO case. Lower efficiencies were obtained and therefore these structures were disregarded from the current study.

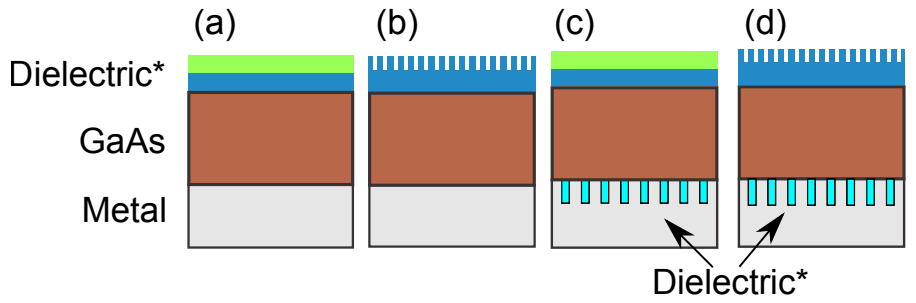

Figure 2.1: (a) Bilayer antireflection coating made of ZnS and MgF_2 (Reference System). (b) Front ZnS nanostructure only (FNO). (c) A bilayer as antireflection coating and a back nanostructure only (BNO). (d) Front and back nanostructures on the same device (FBN). Dielectric*: MgF_2 (top green), ZnS (blue) or SiO_2 (bottom cyan).

Table 2.1: Summary of optimal structural parameters

Case	h (nm)	d (nm)	a (nm)	r (nm)
FNO	110.7	44.8	343.7	111.3
BNO	451.8	-	637.9	274.16

Table 2.2: Summary of efficiencies, short circuit currents and open circuit voltage for the systems studied

Case	$\eta(\%)$	V_{oc}(V)	J_{sc}(A/cm^2)
Reference	33.2	1.331	20.836
FNO	34.0	1.331	21.349
BNO	33.8	1.329	21.219
FBN	**34.4**	1.329	21.631

The feature sizes of the nanostructures in the FNO and BNO cases were optimized following 3 steps:

1. The parameters h and d were optimized keeping fixed values for a and r.
2. Conversely a and r were optimized keeping fixed the optimal values found in step 1.
3. Finally h, d, a and r were optimized using the values found in steps 1 and 2 as seed.

In the BNO case the ARC is the same as in the reference system. The feature sizes of the final nanostructures are shown in Table 2.1. The efficiency, short circuit current density and open circuit voltage for each system are shown in Table 2.2.

2.4 Discussion

The nanostructured devices show higher efficiencies (34.0% vs 33.2%) and higher short-circuit currents (21.35 vs 20.83 A/cm^2) than the reference system. In the FNO case, the enhancement comes mainly from lower reflection losses, as shown in Fig. 2.3(a). There are reflectance oscillations at energies near the GaAs band gap in

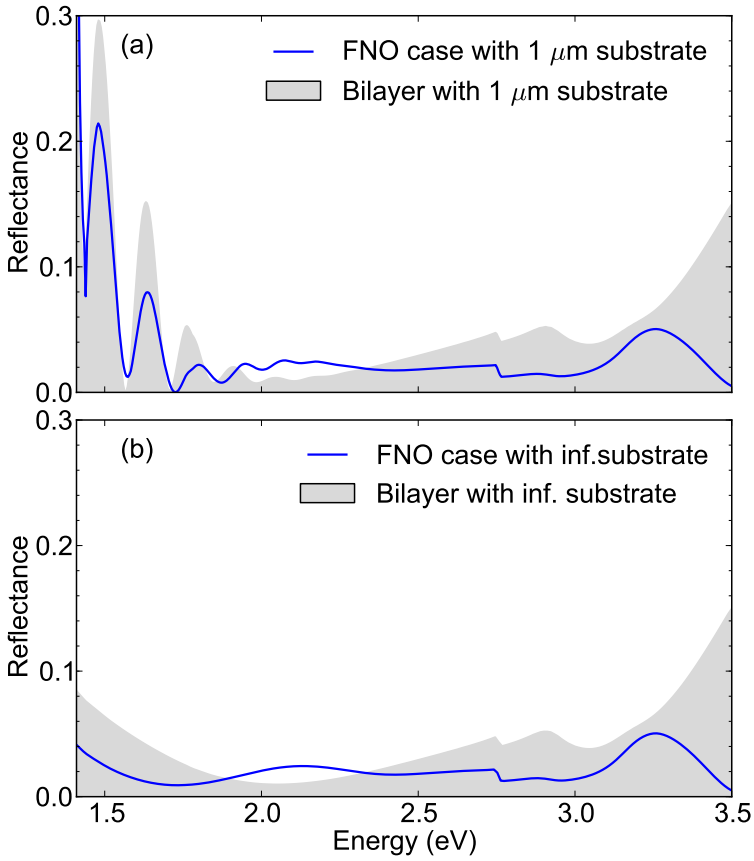

Figure 2.2: Normal incidence reflectance for the reference structure, bilayer (shadowed area) and FNO, (a) with 1 μm GaAs substrate, and (b) with infinite GaAs substrate.

the reference and FNO case, which are Fabry-Pérot resonances. The oscillations dissapear in an infinite substrate as can be seen in Fig. 2.2.

The cause of the lower reflectivity in the FNO case is twofold. The periodicity of the nanostructure (a = 343.70 nm) is such that only the zeroth diffraction order is reflected back into air at normal incidence (the first diffraction order appears at 3.6 eV), whereas several diffraction orders are excited within the solar cell due to the higher refractive index of the semiconductor. The ratio of available diffraction orders inside vs. outside of the solar cell plays an important role in solar cell light trapping.[22, 31] Because of the low diffraction efficiency in the FNO case, the optical modes inside the slab are not significantly perturbed and the Fabry-Pérot resonances dominate at low energies, where the GaAs absorptivity

is low. Additionally the FNO nanostructure at low energies can be described as an effective medium and behaves as a dielectric layer with an effective index.[90] This refractive index can be optimized by modifying the nanostructure dimensions, i.e. the nanostructure has an additional degree of freedom compared to the bilayer, and a lower reflectivity can be achieved.

The BNO structure is able to diffract the transmitted light and the optical Fabry-Pérot modes are perturbed as is shown in Fig. 2.3 (a). The coupling of diffraction channels to the guided modes of the semiconductor slab are responsible for the low energy narrow peaks in Fig. 2.3 (a),[31, 59, 84] leading to an increase in the absorptance and consequently an increase in efficiency. For the BNO case, J_{sc} and η are enhanced as the back diffraction grating increases the optical path length. A drawback of this scheme is the enhanced luminescence coupling at large emission angles away from the surface normal, and in this case leads to a small decrease in V_{oc} compared to the reference system.

In concentration the photon flux from the Sun reaches the cell only at relatively small incidence angles, thus increasing the absorptance at incidence angles $\theta > \theta_{max}$ not only does not increase the generated photocurrent, but reduces the output voltage as it increases the luminescence photon flux F_{c0}, which is detrimental to the voltage as shown in Eq. (2.3). A solar cell that uses a light trapping scheme to maximize absorption, such as a Lambertian scatterer,[21] and/or an antireflection coating, is likely to pay a voltage penalty due to luminescence at angles outside the incoming light cone.[91] To clarify the balance between increased photocurrent and reduced voltage due to emission losses, we present in Table 2.3 the values for F_s (absorbed sunlight flux) and F_{c0} (blackbody emission from the cell at zero bias) for each of the studied cases normalized to the reference values. The increment in F_{c0} is responsible for the emission losses and if it is not associated with a similar increment in F_s, a degraded V_{oc} results, as shown in Eq. (2.3). The FNO case presents an increment of 4.8% in F_{c0} and a 3.0% increment in F_s, thus FNO case does not present significant losses in V_{oc}. In the BNO and FBN cases, the increment in F_{c0} is 10.6% and 12.2% respectively, but the increments of F_s are only of 2.7% and 4.9%, and therefore V_{oc} decreases. This behavior is expected for light trapping schemes where the absorptance/emittance is enhanced isotropically, the increment in efficiency being limited by emission losses. For example, we have calculated a similar case but with an ideal ARC with zero reflection regardless of

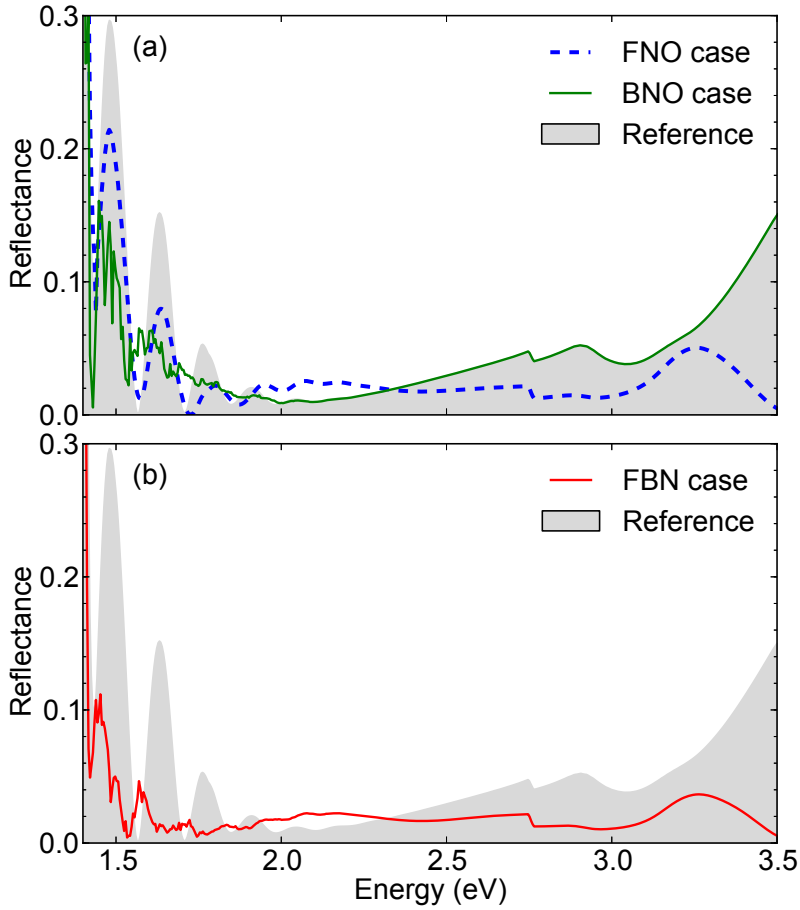

Figure 2.3: Normal incidence reflectance for the reference structure (shadowed area) and (a) FNO (blue dashed line) and BNO (green line) cases, (b) FBN case (red line).

the incidence angle. Such device has 34.6% efficiency and V_{oc} = 1.332 V. Adding on top a Lambertian diffuser that isotropically scatters light increases the efficiency to 35.1% due to the increased optical path length, but reduces the V_{oc} to 1.326 V due to the increased luminescence losses.

Table 2.3: Ratio between the photon fluxes from the nanostructured cases (FNO, BNO and FBN) and photon flux from the reference

$F_{c0}^{FNO}/F_{c0}^{Ref.}$	$F_{c0}^{BNO}/F_{c0}^{Ref.}$	$F_{c0}^{FBN}/F_{c0}^{Ref.}$
1.048	1.106	1.122

$F_{s}^{FNO}/F_{s}^{Ref.}$	$F_{s}^{BNO}/F_{s}^{Ref.}$	$F_{s}^{FBN}/F_{s}^{Ref.}$
1.030	1.023	1.049

To further analyze the emittance in the systems proposed we present plots of the emittance as a function of energy and angle in Fig. 2.4. In the critical spectral region for luminescence, i.e. at energies near the band gap, the FNO is similar to the reference case, therefore the output voltage is not significantly affected. The emittance is almost one for near normal incidence angles and decreases to less than 0.8 for angles larger than 75°. The emittance is increased for low energies near the band gap and for angles between cases 0-60 degrees in cases BNO and FBN, producing a slight loss in voltage due to radiative recombination. At near normal incidence only the zeroth diffraction order exists in air, while several orders exist inside the semiconductor for all angles due to the higher refractive index. The reflectance is increased as more diffraction orders open in the incident medium, and so the emittance decreases.

Overall, as seen in Table 2.2, the real impact of these changes in V_{oc} is rather small. In the case of 1 μm thick GaAs cells operating at 500 suns, the non-radiative losses are of the same order of magnitude as radiative losses [92]. Therefore, as the former are unaffected by the solar cell modifications here proposed, the slight decrease in output voltage are of less practical importance. In fact, these changes in V_{oc} can be expected to be even smaller in thicker devices. In Figure 2.5 we compare the Auger recombination current and the Shockley-Read-Hall recombination current with the radiative recombination current calculated according to the Shockley-Queisser model for our reference system. In practice, the impact of radiative recombination

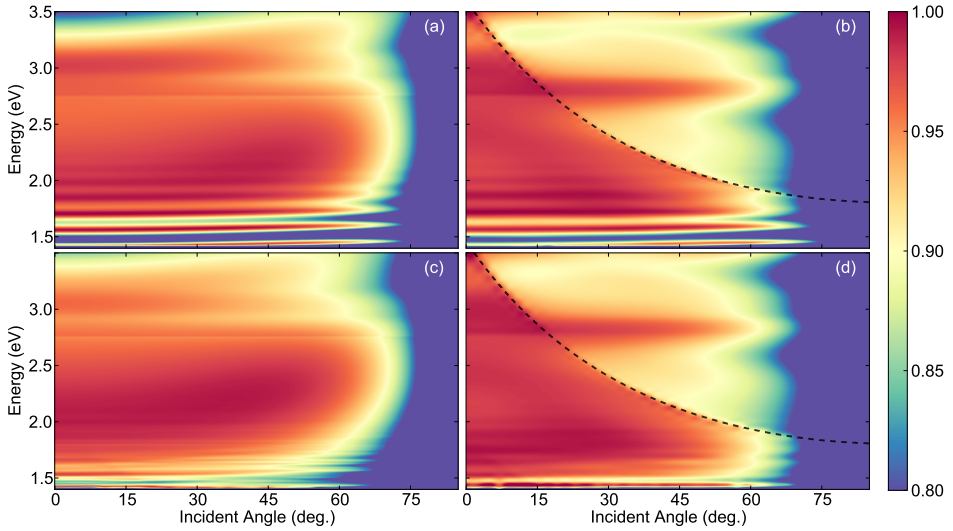

Figure 2.4: Emittance as a function of the incidence angle for the Reference (a), FNO (b), BNO (c), and FBN (d) cases. The dashed line indicates the threshold for the onset of higher diffraction orders in air.

losses would only be crucial in solar cells highly optimized for light trapping, with junction widths of a few hundred nm at most, as non-radiative recombination is proportional to junction width.

Finally, we try to exploit the benefits of the FNO and BNO devices by combining them into a single one, the front and back nanostructure (FBN) case. Its design starts from the optimized values of the FNO and BNO structural parameters (Table 2.1) without any further optimization.[2] The complicated angle and energy dependence observed in Fig. 2.4 (c) is smoothed out when the effects of both the front and back nanostructures are combined in Figs. 2.3(b) and 2.4 (d). The FBN system shows an increase of 1.2% efficiency and 0.8 A/cm^2 in short-circuit current, see Table 2.2. Hence, the FBN case results in a significant reduction in reflectance losses and increases the optical path length resulting in an increase of the photocurrent. The resulting voltage is the same as in the BNO case and

[2] In order to be able to use periodic boundary conditions with a simple unit cell in the FBN case, the period of the back nanostructure was changed from the optimal value of 637.9 nm found in the BNO case to 687.4 nm, i.e., twice the optimal value found in the FNO case. To minimize the impact of this change, the ratio between lattice parameter and nanopillar radius was kept the same as in the BNO case.

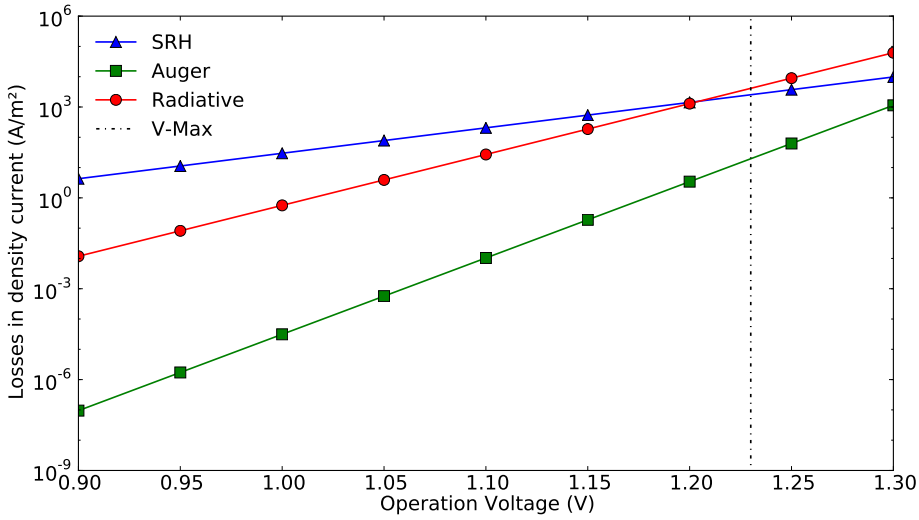

Figure 2.5: Shockley-Read-Hall recombination current (blue triangles), Auger recombination current (green squares) from [92], and the radiative recombination current calculated according to the Shockley-Queisser model for our reference system (red circles). V_{max} (dashed line) corresponds to the maximum power operating voltage of our ideal reference system in the absence of non-radiative currents, and thus represents an upper limit for the operation voltage, while the typical operation voltage of state of the art concentrator GaAs junctions is 1.1 V.

slightly reduced in comparison to the FNO and reference cases, as expected due to the higher emittance at angles out of the incidence cone (Fig. 2.4 (d)).

2.5 Conclusions

In conclusion, we have studied solar cells embedding optimized periodic nanostructures in front and back-side dielectric coating layers (ZnS and SiO_2) to increase the efficiency in concentrator solar cells without nanostructuring the active layer. Two complementary approaches were calculated: nanostructures at the top, and nanostructures at the bottom of a 1 μm GaAs solar cell. The physical mechanisms enabling increased efficiencies in the present proposal can be summarized as: 1) the restriction of the open diffraction channels in air to the zeroth order while simultaneously exciting several diffraction channels inside the

semiconductor, 2) the coupling of the diffraction channels to guided modes in the semiconductor slab, and 3) the index matching with the incident medium due to the effective refractive index of the nanostructure. The top nanostructure is clearly a better antireflection coating than the standard, state of the art bilayer coatings, and there was no significant degradation in the voltage due to the inevitably higher luminescence. The bottom nanostructure increases absorption due to longer optical path lengths inside the semiconductor, and consequently increases the short circuit current. Finally a solar cell nanostructured on both sides has been proposed showing an absolute efficiency increase of 1.2% compared to a reference cell using state of the art antireflection coatings and a perfect backside mirror.

Chapter 3

Broadband antireflective nano-cones for tandem solar cells

In this chapter different designs for a broadband nanostructured antireflective coating are presented. They are made of nano-cones in square lattice made of ZnS, TiO_2 and Si_3N_4. In the best case, the spectrally integrated transmittance (accounting for both reflection and dielectric absorption losses) for direct solar radiation is 99 %, which represents a four-fold decrease in transmission losses in comparison to a standard antireflective coating bilayer. The dependence of the transmission as a function of nanostructure dimensions is studied, showing a wide maximum, thus leading to a high tolerance for manufacturing errors. This high transmittance is also robust against deviations from normal incidence. Our analysis suggests that the high transmittance is due not only to an effective gradual index effect, but is also due to light coupling to quasiguided modes in the photonic crystal leaking mostly towards the substrate. This work was published in [69].

3.1 Introduction

The high refractive index of most semiconductors used as active materials in solar cells leads to the challenge of avoiding reflectance losses at the semiconductor surface. In the particular case of silicon solar cells, it is practical to texture the surface with pits or pyramids much larger than the light wavelength. The effect of such texturing can be understood on the basis of ray tracing, as reflected rays are likely to strike the device surface repeatedly [79]. In other cases, reflection losses are addressed by coating the device with transparent index matching layers [93–95]. The refractive index of each thin film must be the geometric mean of the refractive indices of its surrounding layers to meet the condition of interference. This presents the difficulty of finding new materials with appropriate refractive index. A viable approach is based on porous or mixed layers, where the filling factor determines the effective index of each layer [96, 97]. Another approach is to create a gradual index layer, which minimizes the reflection through a progressive refractive index toward the substrate [98]. The here proposed antireflective coatings (ARCs), could be seen as a similar approach to create an effective refractive index gradient to reduce the reflectance. The proposed periodic nanostructures work as an effective medium for wavelengths larger than the lattice parameter, as a photonic crystal (PC) for wavelengths close to the lattice parameter, and a as diffraction grating for wavelengths shorter than the lattice parameter.

The bio-inspired moth-eye structure, i.e. a compact distribution of nano-cones , has has been recently applied to solar cells. [46, 47, 56, 99, 100] In [99, 100] high index dielectric nanostructures have been designed with some local optimizations and fabricated. The structures show a reflectance weighted with the solar spectrum of 6.2% from 350 to 900 nm [99] and 6.7% from 350 to 1000 nm [100]. Also nanostructures in the window layer have been fabricated with lower average reflectance, 2.7 % over GaAs from 450 nm to 1650 nm and 2.1 % over a GaInAs-N from 320 to 1800 nm. [46, 47] However, nanostructures in the window layer are expected to increase the absorption and the surface recombination within it.

Perl et al. have previously simulated various ARCs based on periodic nanostructures, but these were modelled as gradual index multilayer, without including the physical effects due to the photonic crystal periodicity [61, 62]. Here we show that such

effects significantly can contribute to lower reflectance losses in properly optimized structures. We present three dimensional rigorous coupling wave analysis (RCWA) simulations [101] of fully optimized nanostructures in a square lattice. The dielectric nanostructure is modelled on top of one or two intermediate index matching layers sitting on top of a high index semiconductor, i.e GaInP as a top cell in a tandem solar cell. The integrated spectrum reflectance for the optimized ARC is of 0.54% from 350 to 1800 nm: a four fold decrease in reflection losses in comparison to state of the art bilayer ARCs. We expect the here proposed ARCs to contribute to progress toward 50% efficient solar cells [102].

The optical band studied spans most of the usable solar spectrum in multijunction devices. The cell is modeled with air as the incident medium, and a $Ga_{0.49}In_{0.51}P$ substrate, lattice matched to GaAs. The window layer is modelled as a 15 nm AlInP layer. The losses (L_x) are weighted using the AMG1.5 direct and circumsolar solar spectrum [103]:

$$L_x = \frac{\int_{\lambda_0}^{\lambda_1} x(\lambda) I_{\mathrm{AMG}}(\lambda) \mathrm{d}\lambda}{\int_{\lambda_0}^{\lambda_1} I_{\mathrm{AMG}}(\lambda) \mathrm{d}\lambda}, \tag{3.1}$$

with λ_0=350 nm and λ_1=1800 nm . The analysis is done including not only reflectance losses [L_{R}, $x(\lambda) = R(\lambda)$], but also absorption in the ARC [L_{ARC}, $x(\lambda) = A_{\mathrm{ARC}}(\lambda)$] and absorption in the window layer [L_{W}, $x(\lambda) = A_{\mathrm{W}}(\lambda)$]. The optimizations maximize the weighted integrated transmittance through the interface of the ARC with the window layer, $T = 1 - L_{\mathrm{R}} - L_{\mathrm{ARC}}$. However, the window layer is not part of the optical design because its thickness is constrained by the confinement of the minority charge carriers. The dielectric constants of the materials are taken from [88, 104–106], including absorption, see Figure 3.1.

To use the RCWA algorithm the nanostructure needs to be defined as layers ergo the cone is sliced in coaxial cylinders with an increasing radius, 9 levels for the global optimization and 50 for the analysis. The nano cones have a linear profile. For the particular geometries and materials in our study, we find that deviations from a linear profile do not lead to a significant improvement of the transmission. It is quite possible that further increasing the number of free parameters in the model would lead to slightly increased transmission, as suggested by the previous

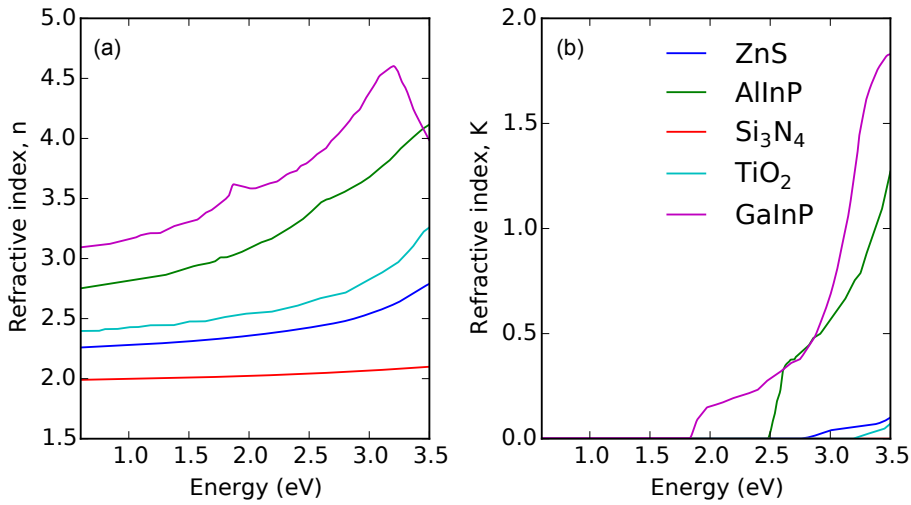

Figure 3.1: Refractive index used in this chapter,(a) real part n, (b) imaginary part k.

works by [76, 107] on the basis of one dimensional models and effective index gradients.

This chapter is organized as follow: firstly in Sec. 3.2 the optimized results are exposed and studied. Also these results are tested against out of normal incidence, Sec. 3.2.1 and stability of the optimum with fabrication errors, Sec. 3.2.2 . Secondly, in Sec. 3.3, we have studied the ability of these structures to increase the optical path inside the solar cell, i.e. a light trapping structure. Finally, in Sec. 3.4, a representative structure of the optimized results is analyzed, studying the physics involved in the PC transmittance.

3.2 Optimization results

We compare four different optimized structures based on ZnS and TiO_2 as a high index materials, and Si_3N_4 as low index material. Two of the structures are based on a high refractive index PC, Fig. 3.2(a), and two others are based on a low index PC on top of an additional index matching layer, Fig. 3.2(b). Even though the refractive index of ZnS and TiO_2 are quite similar, we decide to analyze both systems given their technological relevance in ARCs. The unit cell is defined by the

lattice parameter a enclosing a cone with circular base of radius R and height h, and a thin film of thickness d made of the same material as the cones. For the low index PC structure the thickness of the matching index layer is d_0. An upper and lower bound limit each geometrical parameter which define the PC in the optimization: a is optimized from 0.2 to 1.0 μm, the filling factors (R/a) from 0.1 to 0.5; the height of the cone, the thickness of the nanostructure and the index matching layer (h, d and d_0), from 0.0 to 1.0 μm. The algorithm used is a global optimization (Controlled random search with local mutation, [108, 109]). The reference used to compare all the nanostructures is a standard bilayer made of MgF_2-ZnS, with 107 nm and 52 nm of thickness respectively [93].

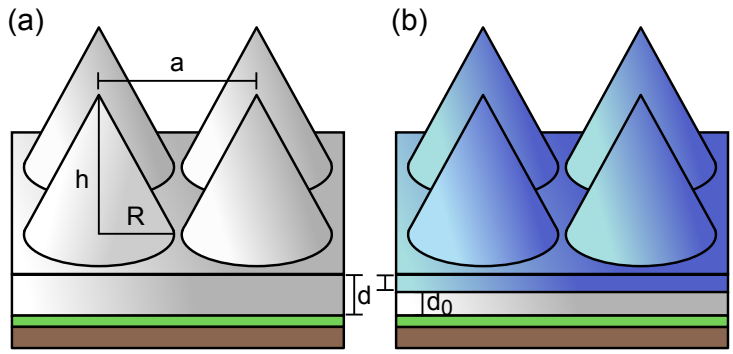

Figure 3.2: Sketch of the simulation cell, the high index PC (a) and the low index PC (b). The solar cell is simulated as an infinite substrate made of GaInP (brown) with a window layer made of AlInP (green) 15 nm thick, in both cases. The high index PC is made of ZnS or TiO_2, (grey), and the low index is made of Si_3N_4 (blue), with a high index matching layer made of the same materials as the high index PC.

The optimal geometric parameters which maximize the transmittance of each structure are shown in Table 3.1, whereas the losses and transmittance for each system are shown in Table 3.2.

It is quite surprising that the fill factor at the base of the optimized structures, except for the TiO_2 case, does not tend to be as big as possible to reduce the effective index step with the substrate. The fundamental reason for such behavior is the size of the optimal lattice parameter of the structure. It is not small enough to consider it sub-wavelength for the propagating medium due to its high refractive index, therefore, the physics at play cannot be described in terms of effective index

Table 3.1: Optimal dimensions of the PC ARCs.

System	a(nm)	R(nm)	h(nm)	d(nm)	d_0(nm)
ZnS	580	263	540	26	-
TiO_2	444	222	534	43	-
Si_3N_4/ZnS	350	163	555	42	53
Si_3N_4/TiO_2	344	163	512	51	49

Table 3.2: The calculated losses, and transmittance for the reference and for each nanostructure. L_W is not included in the transmittance of the ARCs.

System	L_R (%)	L_{ARC} (%)	T(%)	L_W(%)
Reference	3.86	0.62	95.52	2.58
ZnS	1.76	2.32	95.92	2.52
TiO_2	0.74	1.04	98.22	2.99
Si_3N_4/ZnS	0.97	0.91	98.12	3.01
Si_3N_4/TiO_2	0.54	0.34	99.12	3.20

media. Intuitions based on well known results for 1D gradient index optimizations [76, 107] do not take into account diffraction phenomena. It is therefore necessary to optimize the structures on the basis of full 3D modelization.

Figure 3.3 shows the reflectance of each case. There is an enhancement in the infrared region, from 0.69 to 1.55 eV (1800-800 nm), compared to the reference structure and in the blue and near ultraviolet regions, from 2.75 to 3.5 eV (450-350 nm). However, in the region between 1.55 eV and 2.75 eV only the Si_3N_4/TiO_2 PC has similar reflectance to the reference and outperforms it out of this range.

Table 3.2 shows that all the nanostructured systems have lower losses for the integrated reflectance, L_R, than the reference, and a higher transmittance. However the L_{ARC} is higher for the nanostructured cases, except for the low index PC made of Si_3N_4/TiO_2. In special L_{ARC} in the ZnS PC is the highest, lowering the possible increase in transmittance. The ZnS PC leads to an increase in transmittance of only 0.40 % compared to the reference. The PC induces resonances which intensify the electric field not only inside it but also in its surroundings leading to an increase in L_{ARC}. This phenomenon is used in light trapping schemes for materials with a weak

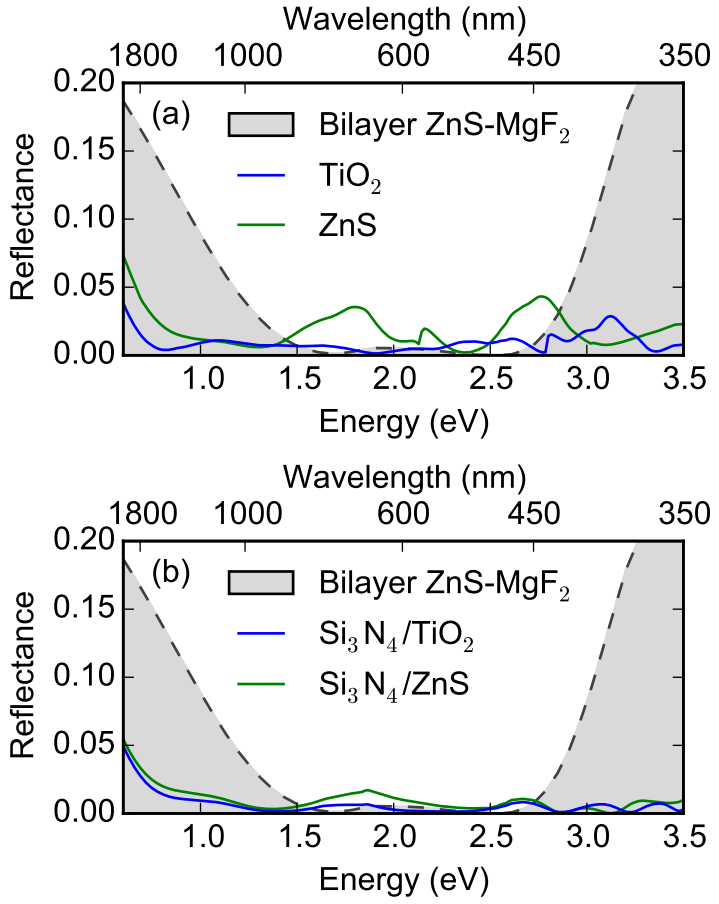

Figure 3.3: (a) Reflectance for a TiO_2 PC (blue) and a ZnS PC (red) compared with the reference MgF_2-ZnS bilayer (shadowed gray) (b) Reflectance for the Si_3N_4/TiO_2 PC (blue) and Si_3N_4/ZnS PC (red) compared with the reference MgF_2/ZnS bilayer (shadowed gray).

absorptance [22, 33, 34, 84] but is detrimental for an ARC, where the transmission to the semiconductor is the objective. According to this, the materials comprising the nanostructured ARC are constrained to transparent dielectrics. The TiO_2 PC leads to an increase in transmittance of 2.70% and 2.30% compared to the reference and the ZnS PC respectively. The cause of the higher transmittance of the TiO_2 PC is twofold; firstly the absorption edge for the TiO_2 (3.2 eV) appears at higher energies than in the ZnS , which entails a smaller L_{ARC}; secondly the refractive index of TiO_2 appears to better match the air to the semiconductor leading to a smaller L_{R}. To confirm this the optimized structure of the ZnS was simulated using the TiO_2 instead of ZnS without further optimizations obtaining L_{R}=1.22%, lower than the ZnS optimized structure were L_{R}=1.76%.

Low index PCs are able to reduce L_{ARC} in comparison to the high PCs made with the same material of the index matching layer, Table 3.2. The resonances of the low index PC appear inside the absorption-less Si_3N_4 instead of the TiO_2 or ZnS, cutting down the L_{ARC}. In particular for the low index PC with ZnS as index matching layer, the L_{ARC} is reduced to less than a half compared to the high index PC of ZnS. This impacts positively in the transmittance where low index PCs show an increase compared to the reference of 3.60% for the Si_3N_4/TiO_2 and 2.60% for the Si_3N_4/ZnS PCs. The losses in the window layer, L_{W}, increase in all nanostructured cases, except the ZnS PC, in part because of a minimization in the reflectance also entails an increase in the photon flux in the front face of the window. However the transmittance to the GaInP substrate (transmittance of the ARC minus the L_{W}) is higher for the nanostructured systems than the reference as can be obtained from the values in Table 3.2. This increase is related with the distribution of the electromagnetic fields near the nanostructure. The PCs confine light in the PC quasiguided modes which overlap with the window layer, increasing absorption losses.

The magnetic energy density, shown in Fig. 3.4, gives information about the field distribution inside the PC, and its impacts in the different losses processes. It is more concentrated inside the nanostructure made of TiO_2 than in the Si_3N_4/TiO_2 at the same energies. This can be seen comparing the contrast between the surroundings (air and substrate) and the nanostructure, Fig. 3.4(a)–3.4(h). An spatial concentration of the magnetic energy inside the ARC suggest that the incident light couples to the PC quasiguided modes [34, 110]. These field confinement can

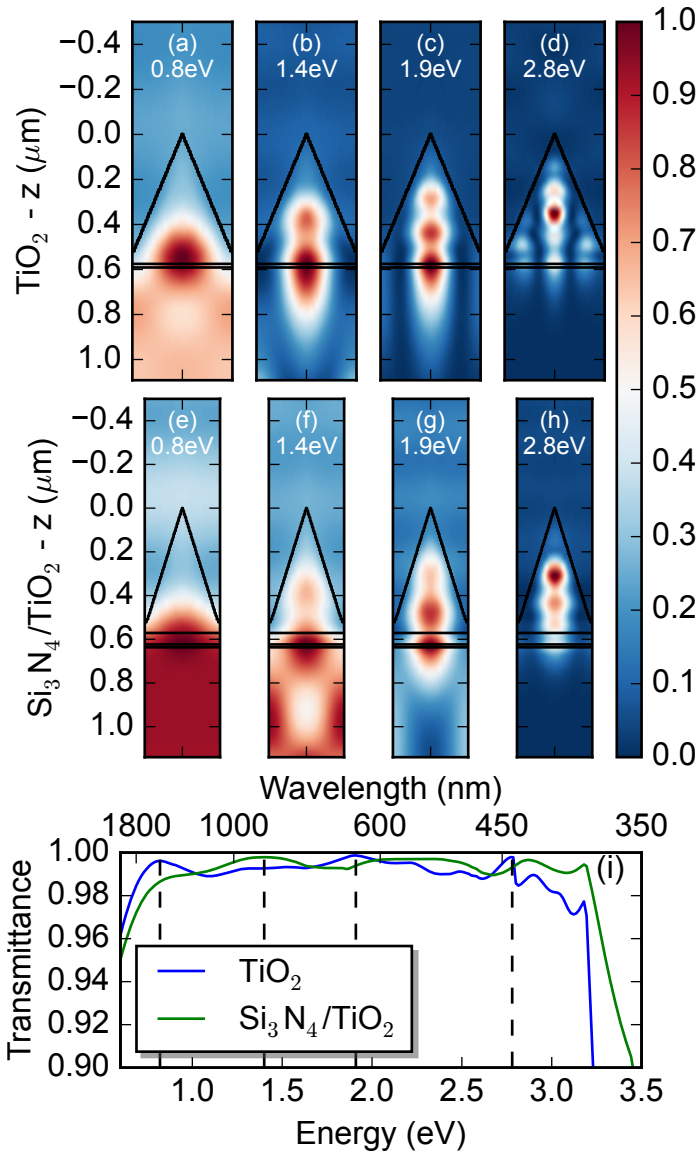

Figure 3.4: Unit cell cross sections along the z-y plane of the normalized magnetic field energy density for normal incidence with S polarization ($\mathbf{H}^2$). (a) to (d) are the TiO_2 ARC and (e) to (h) are the Si_3N_4/TiO_2 ARC. In black contour lines the nanostructure. (c) The transmittance for the Si_3N_4/TiO_2 (blue) and TiO_2 (green) ARC. The dashed lines in (i) correspond to the energies of the $\mathbf{H}^2$ plots (a-h).

be further confirmed by the sudden drop of transmittance at energies above the TiO_2 bandgap, 3.2 eV, as seen in Fig. 3.4(i).

3.2.1 Transmittance as function of the incident angle

The Si_3N_4/TiO_2 PC is the system which exhibits the best reflectance and transmittance. The design of previous section was done only for normal incidence. However, concentrator optics leads to an incidence angle distribution [95]. It is important to consider the effect of oblique incidence in the performance of our best structure. The Si_3N_4/TiO_2 PC is tested for incidence angles from 0 to 85 degrees and compared to the reference. In Fig. 3.5(a) the transmittance as a function of the energy and the angle is shown.

The PC exhibits better transmittance for out of normal angles than the reference. This increase can be seen comparing Fig. 3.5(a) with Fig. 3.5(b) and in the integrated transmittance Fig. 3.5(c). This is an expected results, given that the inclined face of the cone help in coupling out-of-normal light.

3.2.2 Effect of fabrication errors on transmittance

We have tested the sensitivity of the transmittance to small variations of the nanostructure dimensions, and the results are represented for the case of the Si_3N_4/TiO_2 PC in Fig. 3.6. The variables have been grouped in three pairs having in mind the fabrication sequence, a deposition of the materials (h, d_0) a lithography step (a, and R), and an etch or regrowth step (h, d).

A 10% change in any of the explored parameters has a negligible impact in the transmittance (<0.05%). Only changes in the filling factor can result in a 10% reduction of performance [Fig. 3.6(a)].

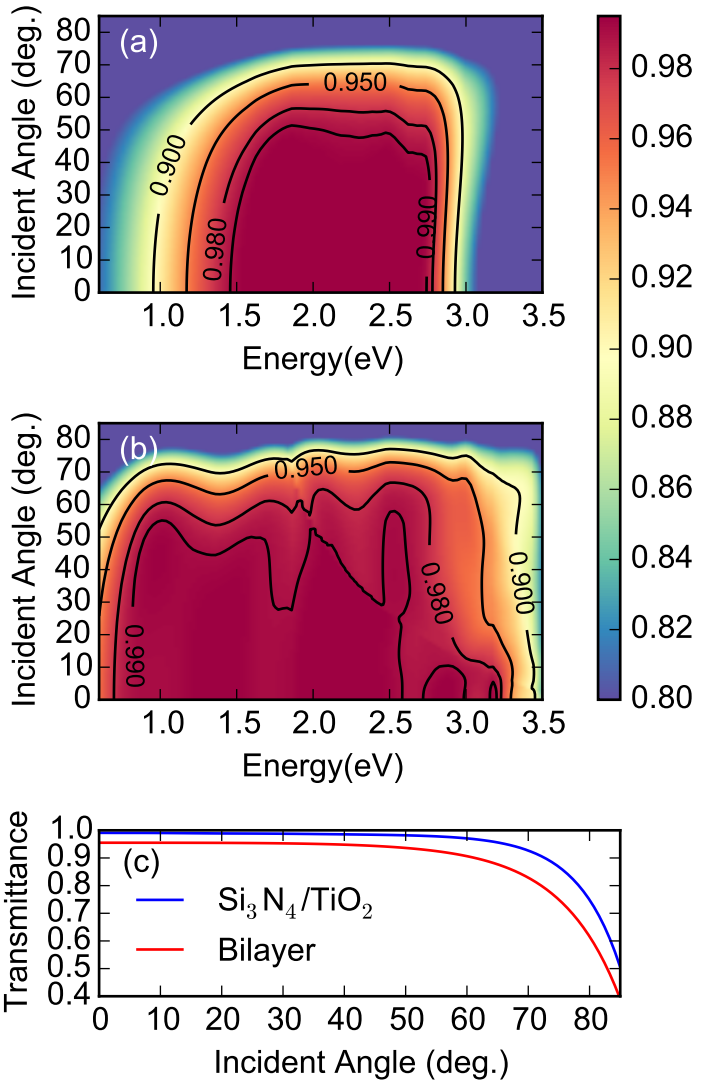

Figure 3.5: Transmittance as a function of the incident angle of the reference bilayer (a) and the Si_3N_4/TiO_2 PC (b). Integrated transmittance of the reference bilayer (red) and the Si_3N_4/TiO_2 PC (blue) (c).

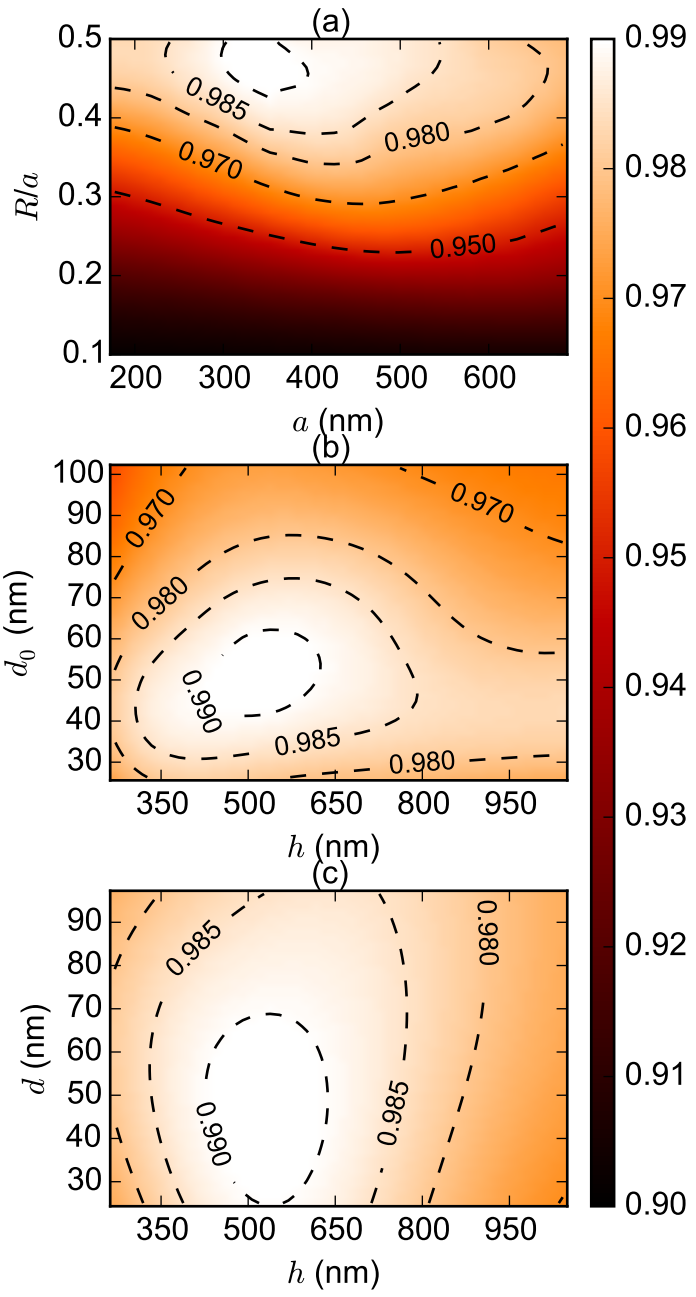

Figure 3.6: Transmittance, T, for the optimum Si_3N_4/TiO_2 nanostructure with modified size parameters from the optimum. (a) T for a fixed h, d, d_0 from the optimum varying a and the relation with the radius (R/a). (b) T for a fixed a and R, radius and d varying h, and d_0. (c) T for a fixed a, R, and d modifying h, and d.

3.3 Light trapping and diffraction orders

The excitation of the diffraction orders inside the solar cell is beneficial to enhance the absorption due to the increased optical path length. In contrast, the diffraction orders excited in the incident medium lead to increased reflectance [22, 57, 68]. The increase in the optical path inside the solar cell allows for thinner junctions without reducing the absorption. This is of interest to lessen the impact of limited minority carrier diffusion lengths, and semiconductor material costs. From the lattice parameters in Table 3.1, the diffraction orders in air show-up only for high energies at normal incidence: the first order appears at wavelengths equal to the lattice parameter, 444 nm for the TiO_2 PC, whereas the first order in the GaInP substrate appears at 1392 nm. We show in Fig. 3.7(a) the distribution of energy for the zeroth order, first order and higher orders. It is instructive to see that the optimized structure forces the removal of energy from the zeroth order. Indeed, there is a minimum at 2 eV, very close to the maximum of the solar irradiance spectrum. Around this energy, the first order has a maximum, confirming the benefits of the increase in optical path length. For higher energies, such distribution of energy is more pronounced and the higher orders become dominant.

In addition to a qualitative analysis, it is possible to quantitatively analyse the optical path length enhancement factor defined as:

$$l_e = \frac{(D - D_0)}{D_0}, \tag{3.2}$$

with D_0 being the optical path length without diffraction and D the optical path with diffraction.

Using the diffraction efficiency of each order and the diffraction angle an average optical path length enhancement factor $< l_e >$ can be obtained [57].

To calculate the $< l_e >$, we have to obtain first the diffraction angle. The diffraction angle θ_i for each order is calculated as:

$$\theta_i = \arcsin\left(\frac{\lambda_0 \sqrt{(g_x^2 + g_y^2)}}{a\sqrt{\epsilon_s}}\right), \tag{3.3}$$

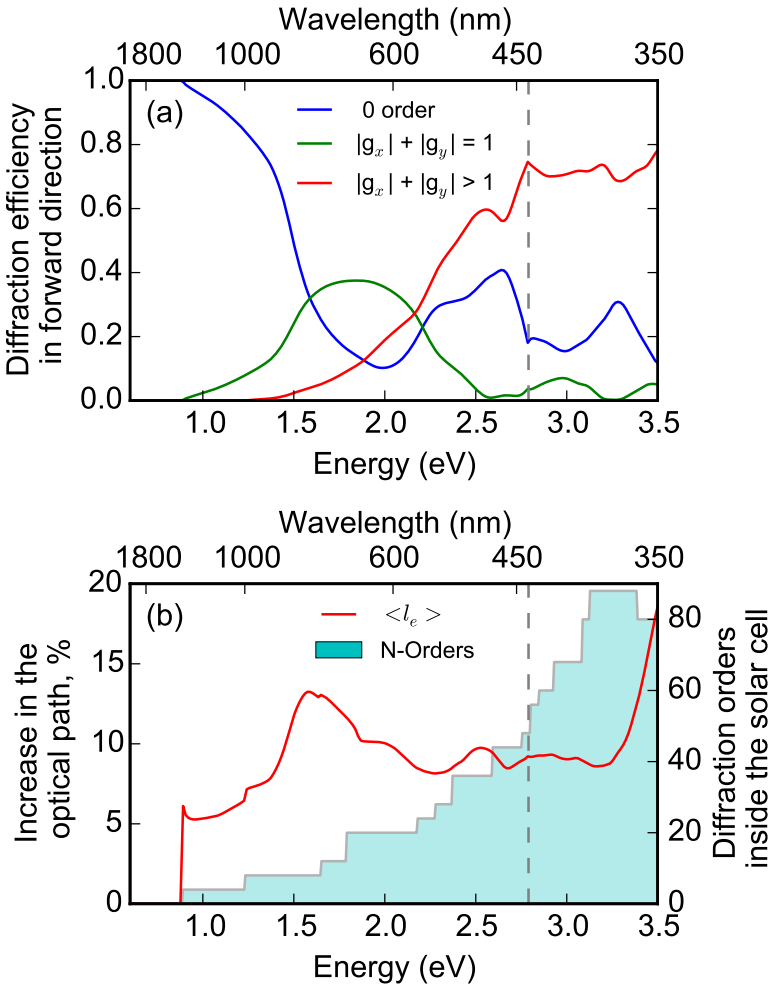

Figure 3.7: Relative diffraction efficiency for each set of diffraction orders (a) in the forward direction, dashed in gray the energy where the first diffraction orders appear in air. Effective optical path for the TiO_2 PC (b) the mean of each diffraction order intensity and angle (red) and the excited diffraction orders inside the semiconductor in solid (cyan).

with λ_0 being the wavelength of the light in vacuum, g_x and g_y being the index of the Bragg harmonics ($g_x, g_y = 0, \pm1, \pm2, \dots$), and ϵ_s the dielectric constant of the substrate. Then the enhancement in the optical path will be:

$$< l_e >= \sum_{i=0}^{N} d_i / \cos(\theta_i), \tag{3.4}$$

being d_i the diffraction efficiency of each order.

In Fig. 3.7(b) the increase in the optical path is shown. The effective optical path in the range between 1.4 to 2.5 eV is important because it could help to have thinner middle and top junctions. For light typically absorbed in GaAs (1.4 to 1.87 eV) the light path is increased 5-10%. For light typically absorbed in GaInP (1.87 to 3.1 eV) the path is increased 10-15%. From 3.25 eV to 3.5 the light trapping rapidly increases towards 19% at 3.5 eV. The optical path tends to increase at higher energies. This is related with the appearance of diffraction orders inside the substrate, as seen in Fig. 3.7(b).

3.4 Quasiguided Modes inside the ARC

The photons reaching the PC are either transmitted to the substrate, reflected to air, or coupled to a PC quasiguided mode [81]. The quasiguided modes inside the PC leak to the air and to the substrate. To understand how these modes are actually contributing to the transmittance, a simplified case is studied. In contrast with the previous optimizations, non-dispersive and non-absorbing materials are used to simplify the analysis, and the thin film below the cone and window layers are removed, leaving only the previously optimized TiO_2 PC and the GaInP substrate. The refractive index inside the cone is n_c= 2.62 and for the substrate n_s=3.67, which are the average values of the TiO_2 and the GaInP refractive index between 0.69 eV and 3.5 eV, respectively. The PC made of cones, is compared with a gradual index multilayer (GIM) . Each layer in the stack is characterized by an effective refractive index, n_G, which results of the homogenization of a slice of the unit cell containing the cone. The effective dielectric constant, $\overline{\epsilon}$, is calculated using the Bruggeman

approximation for cylinders,[111]

$$1 - c = \frac{\epsilon_2 - \overline{\epsilon}}{\epsilon_2 - \epsilon_1} \sqrt{\epsilon_1 / \overline{\epsilon}}. \tag{3.5}$$

being c the filling factor, ϵ_1 and ϵ_2 the dielectric constants of the air and inside the nanostructure respectively.

To understand how the light propagates inside the ARC the energy density, $u(x,y,z) = \frac{1}{2}(\mathbf{E}^2\epsilon_\mathbf{i} + \mathbf{H}^2/\mu)$, is calculated in and outside the nanostructure; being x and y the parallel directions to the substrate surface and z the perpendicular to it; μ and ϵ_i are the magnetic permeability and dielectric permittivity respectively, being a non-magnetic media with $\mu = \mu_0$. The GIM is constant in the $x - y$ directions due the laminar configuration, i.e. $\epsilon_G(z)$, whereas in the cone structure is dependent in the three directions, $\epsilon_C(x,y,z)$.

The transmittance for the cone nanostructure and the GIM are shown in Fig. 3.8(a). The transmittance of both structures are similar at low energies, but the effective index transmittance is about 5% lower. The poor performance of the GIM is because of the lower refractive index of the GIM compared to the substrate at the interface, $n_G(0)$ = 2.06 for the GIM whereas n_S = 3.67 for the substrate. The lower refractive index is because of two reasons. Firstly, a circular base cone in square lattice can not fully fill the unit cell, increasing the step between the GIM and the substrate. Secondly, an effective index medium only can be as higher as the medium with higher refractive index, in this case n_c = 2.63. The GIM structure can provide a lower reflectivity if the discontinuity at the GIM-substrate interface is removed. At higher energies the GIM has a flatter transmittance spectrum than the PC. Also the transmittance for the nanostructure exhibit steep changes in the curvature for the energies where the first diffraction order appears, in the substrate at 0.89 eV and in the air at 2.79 eV. The transmittance of the PC exhibit broad peaks that are correlated with the quasiguided modes inside the structure. The energy densities as a function of distance to the surface are shown in Fig. 3.8(b) and 3.8(c). There is a higher energy density inside the PC than inside GIM. The energy density gradient in both structures is expected due to the continuous increment in effective dielectric permittivity ϵ_i with depth. The PC quasiguided modes lead to energy density peaks at certain depths and energies combinations, which can be seen easily with the levels curve in Fig. 3.8(c). This peaks can be interpreted as resonances,

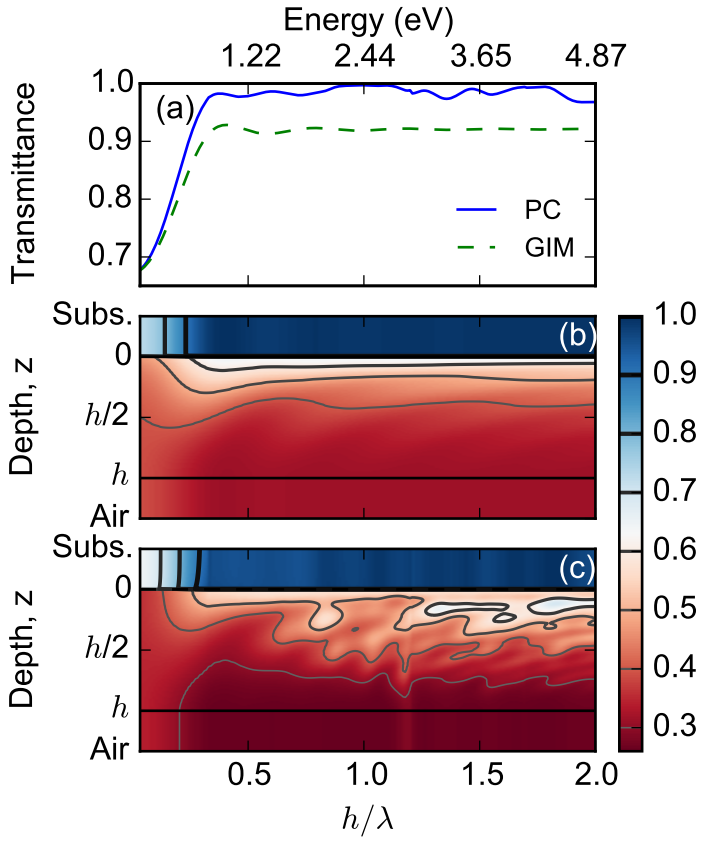

Figure 3.8: (a) Transmittance for the non-dispersive structures a GIM, green line dashed, and a PC made of cones, blue line. Energy density normalized for the GIM and for the PC made of cones (b) and (c) respectively. To compare both structures, the energy density of the PC is integrated in the $x - y$ direction.

which explain the higher L_{ARC} found for the ZnS and TiO_2 PCs presented in Table 3.2, and the peaks found in the transmittance. These increments in the energy density are related with the higher density of states of the PC compared to the multilayer. The modes inside the nanostructure are the energy repositories within the system. These modes are quasiguided and can be found in the complex space of energies/frequencies as the poles of the determinant of the scattering matrix. The real part of each pole is related to the mode frequency, and the imaginary part to the width of the mode or the inverse of the lifetime.

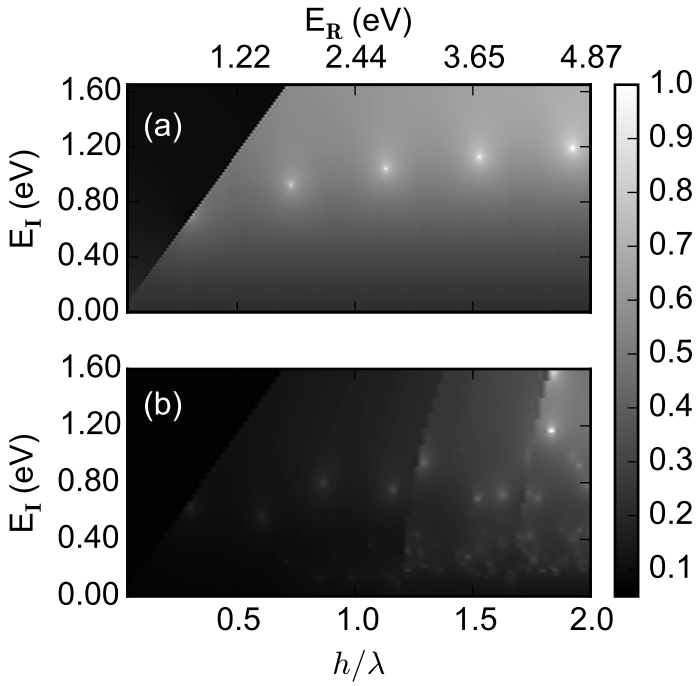

Figure 3.9: Logarithm of the determinant of the scattering matrix normalized, being E_R and E_I the real part and the imaginary part of the energy respectively. Calculated for the GIM (a) and of the PC made of cones (b).

The poles of the determinant of the scattering matrix of both structures are shown in Fig. 3.9(a) and 3.9(b) respectively. The poles of the GIM have a high imaginary part. Indeed the Fabry-Perot resonances of a slab are much broader than the quasiguided modes [112]. The poles found for the effective media occur at slightly shifted energies when compared to the maxima found in the transmittance spectrum. The

shift is related to the interference between overlapping modes [113]. The PC shows two sets of resonances; the first one is analogous to the broad resonances found in the GIM, a set that starts at low energies with high imaginary parts; the second one is a set high energy resonances with small imaginary parts, meaning narrow resonances. The flatness of the GIM above 1.8 eV is attributed to the lack of the second set of resonances in the structure.

3.5 Conclusions

Summarizing an optimal antireflective nanostructure made of Si_3N_4 on top of a TiO_2 thin film is found with a transmittance of 99% for a broadband spectrum ranging from 0.69 to 3.5 eV. The low reflectance is due to the optimal effective medium gradient index and the quasiguided modes excited in the PC. By comparing with simulations based on a effective index gradient, we show that the obtained high transmission cannot be accounted for disregarding the PC resonances. The obtained transmittance is very robust against fabrication errors with a 10% error in any dimension having a negligible effect on transmittance (< 0.05%). For all angles, the transmittance is above that of the standard bilayer typically used in III-V multijunction tandems. On the other hand, a TiO_2 PC was also found which exhibits good transmittance 98% without additional index matching layers. As an additional benefit, these nanostructures excite diffraction orders which increase the optical path. The increment in the optical path is around 10% from 1.5 eV to 3 eV, allowing for thinner semiconductor layers, and thus reduced costs and increased efficiency due to the lesser impact of limited minority carrier diffusion lengths.

Chapter 4

Nano-cones for broadband omnidirectional light coupling to semiconductors

In this chapter the fabrication and characterization of the optimized Moth-eye nanostructure in Chapter 3 is presented. The Moth-eye structure has been proposed several times as an antireflective coating to replace the standard optical thin films and we experimentally demonstrate the feasibility of a dielectric Moth-eye structure as an antireflective coating for high-index substrates, like GaAs. The fabricated photonic crystal has Si_3N_4 cones in a square lattice, sitting on top of a TiO_2 index matching layer. This structure attains 1.4% of reflectance power losses in the operation spectral range of GaAs solar cells (440-870 nm), a 12.5% relative reduction of reflection power losses in comparison with a standard bilayer. The work presented here considers a fabrication process based on laser interference lithography and dry etching, which are compatible with solar cell devices. The experimental results are consistent with scattering matrix simulations of the fabricated structures. In a broader spectral range (400-1800 nm), the simulation estimates that the nanostructure also significantly outperforms the standard bilayer coating (3.1% vs. 4.5% reflection losses), a result of interest for multijunction tandem solar cells.

4.1 Introduction

Nanostructured antireflective coatings have been proposed several times in the literature as a promising alternative, [21, 22, 46, 56, 61–65, 76, 114–121] but their full potential is yet to be achieved. This approach presents the opportunity to engineer the optical response from the top layer by modifying the in plane structures. The bio-mimetic moth-eye nanostructure typically presents low reflectance as previous research has documented. [46, 56, 63, 64, 115–118] However, the previous studies did not consider the case of transparent dielectric nanostructures on high index substrates such as Si, GaAs or GaInP. In particular, in Refs. [64, 117, 118] the nanostructure sits on top of a relatively low index substrate, relaxing the requirements of the anti-reflective coating. A key limitation of these proposals is that they cannot be directly applied to inorganic solar cells given the high refractive index of the semiconductor. On the other hand, the nanostructures in Refs. [46, 56, 63, 115] sit on top of high index substrates, but the semiconductor material itself is nanostructured rather than a transparent dielectric. As we have already mention in Chapter 2 the major drawback of nanopatterning the semiconductor is increasing surface recombination, [122] so an electrical degradation of the device is expected and a better passivation is needed. In conclusion, nanostructuring laterally some of the layers is increasingly seen as a requirement for optimal solar cell efficiency, as evidenced by recent literature.[21, 22, 46, 56, 61–65, 76, 114–121]

Not every nano-lithography technique is suitable for low cost fabrication of large area devices such as solar cells. We have chosen laser interference lithography (LIL) for its capability to uniformly pattern large areas ($> 1\ \mathrm{m}^2$).[123, 124] Electron beam lithography (EBL) and focused ion beam (FIB) are often used for fabricating high quality photonic crystals, but these techniques are not suitable for large area applications due to the use of finely focused beams to define the patterns point by point. Besides its large area capability, another considerable advantage of LIL is that it is a mask-less technique, in contrast with nano-imprint lithography, and therefore, it is compatible with preexisting patterns such as solar cell electrical contacts. Furthermore it does not present the problems associated with template degradation by particle contamination that are often associated with nano-imprint and contact photolithography.

In this work, we have fabricated a Moth-eye nanostructure made with a transparent dielectric (Si_3N_4) on a high index substrate, GaAs. The design was globally optimized using 3D simulations in the previous chapter, Chapter 3.[69]. The design consists of Si_3N_4 nano-cones in a square lattice with the following optimal dimensions: period a = 344 nm, height H = 512 nm, and radius R = 163 nm. Between the nanostructure and the substrate there are two index matching thin films, one made of Si_3N_4 (d = 49 nm), like the nanostructure, and one of TiO_2 (d_0 =51 nm). These dimensions were used as a target for fabrication.

4.2 Experimental methods

Our structure is fabricated on a GaAs substrate and optimized for III-V tandem solar cells. These cells generally operate in optical concentration conditions, allowing to reduce the semiconductor area by up to three orders of magnitude. Still, the fabrication techniques used in this paper are fully compatible with large area solar cell production. The TiO_2 deposition is done using atomic layer deposition (ALD) and the Si_3N_4, using plasma enhanced deposition (PECVD). Both techniques are extensively used in electronics and photovoltaics.[125–130] On the other hand, the nanostructure is patterned by LIL and it is transferred to silicon nitride by reactive ion etching (RIE). LIL is suitable for photovoltaics as discussed in the introduction, whereas RIE is widely used in photovoltaics and microelectronics. [72, 131–134] The LIL setup used in this chapter is detailedin Appendix A.1.

The initial step for the fabrication was the deposition of 51 nm of TiO_2 using ALD. Subsequently 616 nm of Si_3N_4 were deposited using PECVD. Both layers were deposited at a relatively low temperature (200 °C) to ensure process compatibility with a range of photovoltaic technologies. The samples were covered with a diluted positive photoresist (S1805 + PGMEA 1:1) by spin coating at 5000 rpm for 60 seconds and baked at 115 °C for one minute before exposure. The obtained photoresist thickness was 150 nm. We did not use a bottom antireflective resist, as the sample itself is a better ARC.

An auxiliary pattern consisting of an array of 50 μm wide lines with a period of 500 μm was defined by exposing the photoresist using conventional proximity mask UV lithography. This pattern was used to measure the height after the etching step

using a profilometer. The sample was then exposed using LIL with a Lloyd mirror configuration and a 12 mW, 405 nm semiconductor diode laser on a temperature controlled mount. The light from the laser was spatially filtered using a lens ($f = 4$ mm) and a pin hole (5 μm) at the focal plane. A distance of 35 cm separated the pin hole from the sample and the aluminum mirror. The exposure intensity over the sample was controlled using a GaP photodiode mounted below the sample mount.

To obtain a square lattice (2D) the pattern must be exposed twice in two orthogonal directions. The pattern inside the unit cell will be similar to a square or a circle depending one the exposure dose. [135] We have aimed at fabricating a circular nanostructure, so the exposure dose was near to the saturation of the photoresist. After the exposure, the sample was immersed in the developer 15 seconds to obtain the pattern. Fig. 4.1(a) presents the sample after the lithography. The thickness of the photoresist was reduced by the developing process (100 nm) since the nanostructure size is below the resolution specified by the manufacturer of the photoresist and the stability of the photoresist is compromised for patterns smaller than 500 nm. This limits the final nanostructure height, as the photoresist was used as mask for the etching step.

The pattern was transferred to the Si_3N_4 layer using RIE with a 200 W, 460 V, 10 mTorr plasma with a gas flow of 25 sccm of N_2 and 25 sccm of CHF_3.[136]. The attack rates obtained were 55-60 nm/min for the Si_3N_4 and 15-20 nm/min for the photoresist. In order to avoid excessive thermal damage to the photoresist, the attack was pulsed following a periodic sequence of 30 seconds of plasma, 2 minutes of vacuum, 1 minute of N_2 flux and 1 minute of vacuum. To complete the dry etching the loop was repeated 20 times, namely 10 minutes of plasma. The final height of the nanostructure was measured using a profilometer, obtaining 390±10 nm. Fig. 4.1(b) shows the sample after the etching process. After the dry etching, the sample was cleaned using a 50 W O_2 plasma during 30 seconds to remove possible photoresist residues.

The experimental setup used for measuring the reflectance is detailed in Appendix A.2. The reflectance was measured using the light from a halogen lamp dispersed by a 0.3 m focal length monochromator. Temporal fluctuations of the excitation beam were compensated with a reference silicon photodiode. The beam was modulated at 477 Hz with a chopper to allow for lock-in signal detection. A

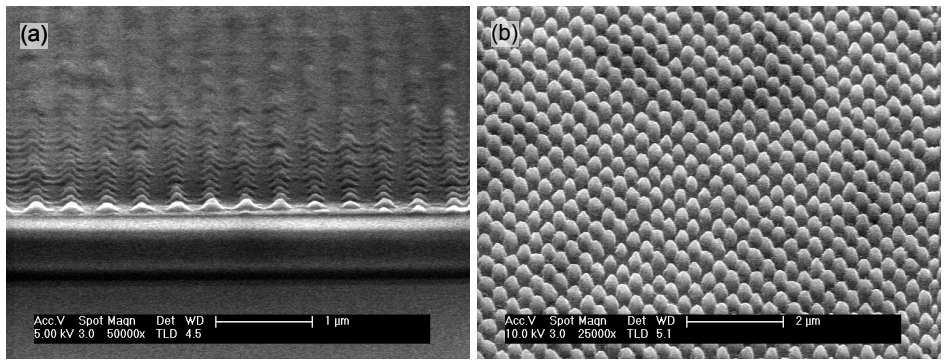

Figure 4.1: (a) SEM image of the photoresist nanopatterned before the RIE etching step. (b) SEM image of the nanostructure after the RIE etching.

200 micron core size multi-mode optical fiber was used to allow for mechanical decoupling of the monochromator and the rest of the set up. The collimated excitation beam was aligned with a Glan-Thompson polarizer at one the horizontal arms of a 45 degree beam splitter, and then focused to a 30 μm diameter spot using a 20X magnification objective lens (NA = 0.4) at the lower vertical arm of the beam splitter. The signal reflected from the sample was collected by the objective and sent through the beam splitter to a lens focused on a silicon photodiode on the upper arm of the beam splitter. For measurements at wavelengths above 700 nm, a dichroic filter was used to block short wavelength light due to the second diffraction order from the monochromator. For our experimental set up we choose optical elements optimized for visible and near infrared transmission. The bounds of our experimental spectra (440 nm to 870 nm) are also limited by the position of the GaAs absorption edge and the spectral distribution of our illumination source.

4.3 Results and Discussion

The reflectivity measurements were compared with the simulations results obtained using the scattering matrix method (SMM)[101]. The refractive indices of the materials were taken from Refs. [88, 105, 106, 137]. The most rigorous comparison between experiment and simulation would require the simulation of a super-cell of the measured nanostructure (a spot of ~30 μm radius), as the

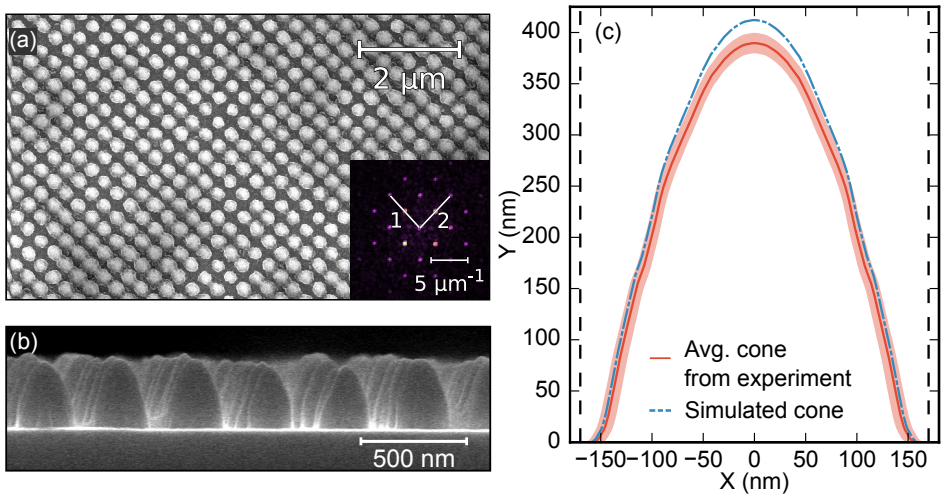

Figure 4.2: (a) SEM image of the nanostructure, inset Fast Fourier transform (FFT) of the structure where 1 and 2 (white-lines) are the (2,0) and (0,2) lattice vectors, whose moduli correspond to a periodicity of 339 ± 3 nm. (b) Cross sectional SEM image used to estimate the mean profile. (c) Mean profile of the cones, scaled to the experimental data (red line), and optimal profile extracted from the reflectance fitting (blue dash-dotted line). The optimal lattice parameter is a=340 nm (vertical dashed black).

fabricated nanostructure is not perfectly homogeneous, see Fig. 4.1(b) and Fig. 4.2(b). Unfortunately, this would require huge computational resources. Alternatively, an average unit cell can quantitatively describe the reflectance of the system. The dimensions describing this unit cell should be representative of the distribution of the real nanostructures. An initial set of dimensions describing the size and shape of the nanostructures was obtained from electron microscopy images and profilometer measurements and then slightly refined by fitting the simulations to the experimental reflectivity. The lattice parameter, a, was extracted from Fig. 4.2(a). We have used Fig. 4.2(b) to estimate an average profile of the fabricated cone. This average profile was smoothed using a Savitzky-Golay filter assuming that the average profile has rotational symmetry around a vertical axis, see Fig. 4.2 (c). The cone is approximated in the SMM code as a stack of 50 concentric cylinders. The SEM image from Fig. 4.2(a) is digitally masked, and it is used to obtain the average radius. In Fig. 4.3 the mask and the histogram of the spatial distribution is presented. The radius obtained is R=156.5 ± 8.4 nm, after analyzing 494 cones. The topographical measurements and the fitted model are

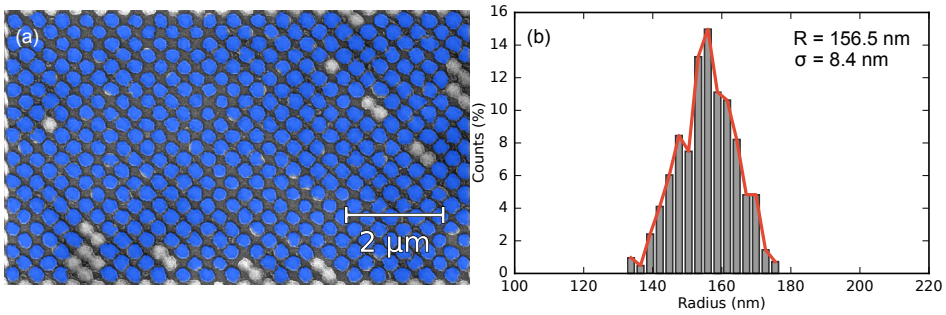

Figure 4.3: (a) Masked SEM image (blue) to determine the cones radius distribution. (b) Histogram of the radius from panel (a), (494 Counts).

System	a (nm)	R (nm)	H (nm)	d (nm)	d_0 (nm)
Experiment	336-342$^{(1)}$	148-165 $^{(2)}$	380-400$^{(3)}$	16-66$^{(4)}$	51$^{(5)}$
Simulation	340	159	413	15	45

Table 4.1: Nanostructure dimensions obtained from sample topography measurement ("Experiment"), and dimensions obtained from fitting the simulations to the reflectance data ("Simulation"). $a^{(1)}$ and $R^{(2)}$ are obtained from Fig. 4.2(a) (The radius distribution is presented in the supplementary materials); $H^{(3)}$ is obtained from profilometer measurements, $d^{(4)}$ is obtained from the etch ratios from the RIE, and $d_0^{(5)}$ is obtained from the deposition by ALD.

presented in Table 4.1.

The experimental and simulated reflectance data are shown in Fig. 4.4(a). The fitting accurately reproduces the experimental results without large deviations in the fit parameters from their expected values, see Table 4.1. The experimental thickness for the TiO_2, d_0, is 5 nm bigger than the fitted one. This small difference is most likely a result of the GaAs native oxide not being included in our simulations. An important question might arise in view of the SEM images presented in Figs. 4.1 and 4.2: the role of the inhomogeneities introduced during fabrication. Our structures show an excellent uniformity in the lattice period, denoted by the sharp peaks in the Fourier transform shown in the inset of Fig. 4.2(a). We have also achieved a high uniformity in the height of the nanostructures, as can be inferred after inspecting Figs. 4.1 (b) and Fig. 4.2(b). The only parameter showing some non-uniformity is the filling factor, i.e. the base radius of the cone. Many studies

have been performed around the role of the disorder in the performance of a nanostructured light-trapping structure. These studies are mostly focussed on the impact of disorder in the lattice period, while disorder in the pattern size generally plays a secondary role. Indeed, as Burresi et al. indicated in Ref. [138], the low order Mie resonances of the nanostructures are spectrally very broad and these resonances are the most relevant ones in this context, given that this antireflective coating operates in the subwavelength regime. In terms of light scattering, this means when the wavelength is larger than the size of the scatterer. A few studies support this operating principle. It has been shown that in disordered 1D structures, the reflection losses decrease with the degree of disorder of the groove width at low degree of disorder of the period.[51] Similar results have been reported for 2D structures,[52, 139] like the one studied here. Hence, the non-uniformity in the filling factor does not necessarily introduce a penalty in the performance of the AR, on the contrary, it might be beneficial to reduce the reflection losses. From our numerical analysis of the reflection data, we conclude that the local changes in the filling factor do not have a noticeable impact in the global performance of the structure.

Fig. 4.4(b) shows the reflectance resulting from our fitting in an extended spectral range from 400 to 1800 nm in comparison with the optimized bilayer. To estimate the total power loss due to reflection we have integrated the reflectance weighted with the solar spectral irradiance:

$$L_{\mathrm{R}} = \frac{\int_{\lambda_0}^{\lambda_1} R(\lambda) I_{\mathrm{AMG}}(\lambda)\, d\lambda}{\int_{\lambda_0}^{\lambda_1} I_{\mathrm{AMG}}(\lambda)\, d\lambda}, \tag{4.1}$$

being $I_{\mathrm{AMG}}(\lambda)$ the spectral irradiance, and $R(\lambda)$ the reflectance.

In the visible and near infrared range of the spectrum ($\lambda_0 = 440$ nm and $\lambda_1 = 870$ nm), the nanostructures lead to a 12.5% relative reduction of reflection power losses in comparison with a standard bilayer (1.4% vs. 1.6% absolute power loss). Extending the integration range to $\lambda_0 = 400$ nm and $\lambda_1 = 1800$ nm, our simulations predict a reflection power loss of 3.1%, while the bilayer leads to a 4.5% power loss. Thus, a 31% relative reduction of power losses is expected. As seen in Fig. 4.4(b), the nano-

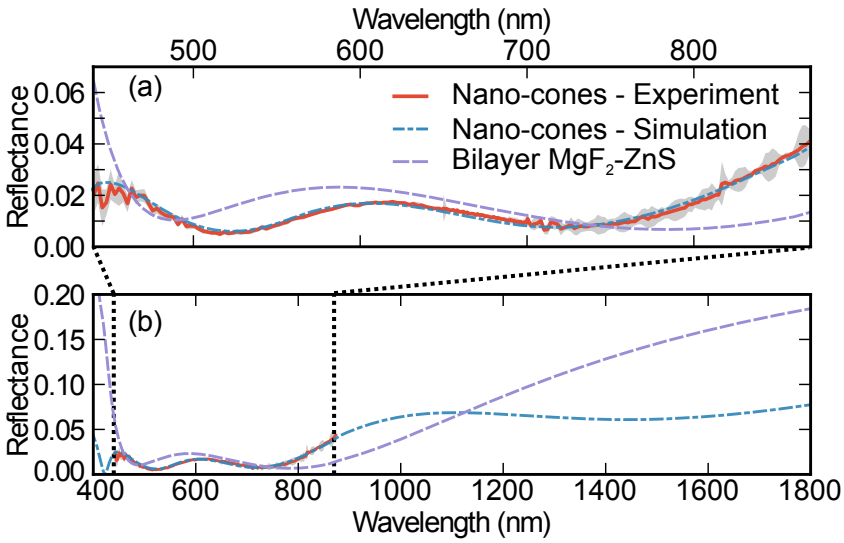

Figure 4.4: (a) Experimental reflectance (red), experimental standard deviation (light gray), theoretical reflectance (dashed-dotted blue) and theoretical reflectance of an optimal bilayer (MgF_2/ZnS) (dashed purple). (b) Theoretical reflectance in an extended spectral range.

cones significantly outperform the bilayer at the shortest wavelengths. However, as the light wavelength shortens the reflectance is expected to become sensitive to the exact shape and size of the nanostructures, thus extending the integration range to shorter wavelengths would have introduced larger uncertainties in the obtained power losses. On the other hand, for long wavelengths, the nanostructure is averaged, and we are able to estimate the results for a broader spectrum. For long wavelengths, the nanostructure has lower reflectance from 1120 to 1800 nm.

The absorption losses can be estimated by replacing the reflectivity with the absorption of the ARC layers in Eq. (4.1).[69] For the wider spectral range (400-1800 nm) the absorption loss of the nanostructured and the bilayer ARC are 0.09% and 0.29%, respectively. In both cases absorption only occurs for wavelengths shorter than 440 nm and in the higher index layers: TiO_2 (nano-cones ARC) and ZnS (bilayer). The higher absorption in the bilayer results from the higher extinction coefficient of ZnS vs. TiO_2. In fact, the measured extinction coefficient of our TiO_2 layers (see Supplementary Material), discards the possibility of significant absorption losses in the ARC.

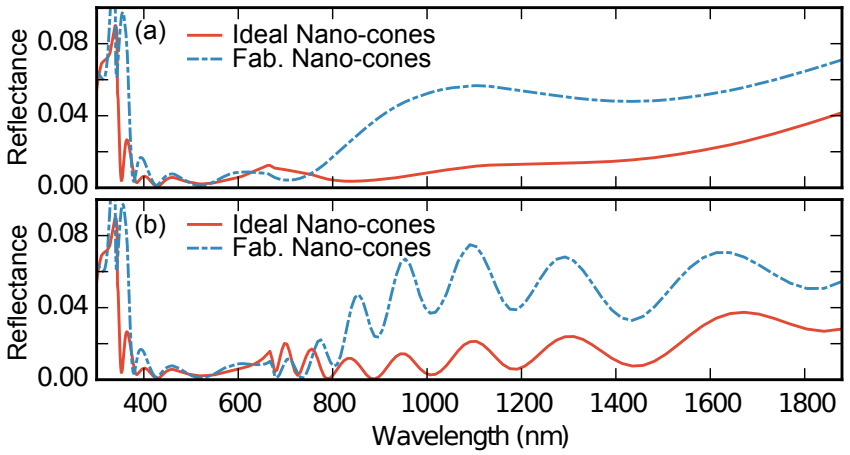

Figure 4.5: Theoretical reflectance for the ideal cone (red) and for the fabricated alike cone (blue dash-dotted) over an infinite GaInP substrate (a), and over a GaInP (1μm)-GaAs substrate(b).

This design has been proved to be superior compared to a standard bilayer, but it is important to put it in the context of state of the art designs presented in the literature. Perl *et al.* reported in Ref. [120] a theoretical 1% power loss integrated over the whole solar spectrum on a GaInP substrate and a 2.8% experimental reflectance loss on a 1 μm thick GaInP layer on a GaAs substrate. This design is based on a SiO_2 cone-like nanostructure on top of a stack of 7 SiO_2 and TiO_2 layers. To enable a direct comparison, we have replaced the GaAs substrate in our simulations of the fabricated structure with the GaInP and GaInP/GaAs substrates used in Ref. [120], as the higher refractive index of GaAs leads to higher optical power losses. For a graphical comparison of this two cases see Fig. 4.5.

The reflectance power loss of our optimal structure on a GaInP substrate is 0.9%, and 1% on GaInP/GaAs. [69] The nanostructures resulting from our fabrication efforts are shorter, narrower, and less sharp than the optimal ones resulting from our simulations. Simulating our fabricated nanostructures on top of the substrates used by Perl *et al.*, the resulting reflection losses are 2.4% on GaInP and 2.5% on GaInP/GaAs. Based on these results it can be concluded that our design results in similar reflectance losses than those of the hybrid design proposed by Perl *et al.* The main difference is that the here proposed structure requires a single TiO_2 layer rather than a SiO_2/TiO_2 multilayer under the nanostructures. Our

previously published analysis suggests that photonic effects such as coupling to quasi-guided modes are fundamental to achieving a very low reflectance with our relatively simple design. [69] Such effects are not expected in the case of the structure proposed by Perl *et al.* due to the very low refractive index contrast of SiO_2 with air. In our case, the use of fully 3D simulations in the optimization of the nanostructures allowed for the tuning of photonic effects beyond the simple graded effective index effect that has been studied in previous efforts based on 1D simulations.

4.3.1 Reflectance vs. the incident angle

Although, as we have already presented in the previous chapter, Section 3.2.1 the reflectance of the ideal design for out of normal incident angles, here we present the reflectance vs. the incident angle for the fabricated model nanostructure for the sake of completeness. The reflectance as a function of the incident angle is illustrated in Fig. 4.6 (a) and (b), for the nanostructure and the bilayer respectively, whereas the integrated power losses for both cases are shown in Fig. 4.6 (c). As seen in Fig. 4.6(a), the low reflectance of the nanostructure is kept for oblique incident angles. In fact, the reflectance power losses for the nanostructure is below 5% from 0 to 57 degrees of incident angle, whereas the standard coating reach 5% power losses from 34 degrees and above, see Fig. 4.6(c). These results for the fabricated cone structure are very similar to those found for the ideal cone structure,[69] which supports the robustness of the design.

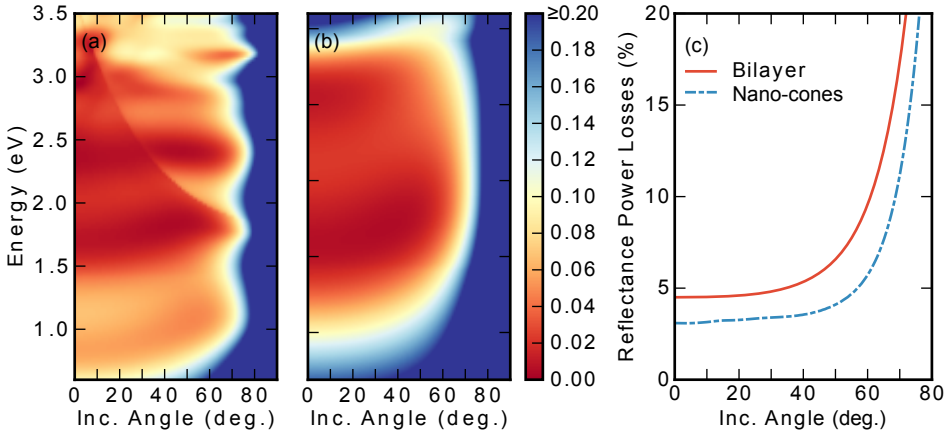

Figure 4.6: Theoretical reflectance as a function of the incident angle of the cone nanostructure (a) and for the optimized bilayer (b). (c) Reflectance power losses as a function of the incident angle of the cone nanostructure (blue dash-dotted) and the optimized bilayer (red line)

Conclusions

In conclusion, our results indicate that it is possible to significantly decrease the reflectance losses on high index substrates using an optimized Moth-eye photonic crystal. In fact, the nano antireflective coating has proved to obtain lower reflectance losses than a standard coating. The fabricated nanostructured antireflective coating represents a 31% relative reduction of reflection power losses over the standard bilayer ARCs. Still, ample room for improvement exists by further optimizing the here proposed fabrication process. In particular, a shorter wavelength laser and a higher resolution photoresist might improve the lithography. A thicker mask for the RIE dry etching step would lead to taller nanostructures. Our simulations predict that further progress along this line of research should lead to solar cells with optical losses under 1% using the here proposed antireflective nanostructures.

Chapter 5

Light-trapping in photon enhanced thermionic emitters

In this chapter we combine the structures presented in Chapter 2 and in Chapter 3 to increase the efficiency in a photon enhanced thermoionic emitter. The photonic crystal structures are optimized for this device to increase the absorption. With realistic parameter values to describe a p-type GaAs device we find an efficiency above 10%. The light-trapping structures increases the efficiency by 2% (20% relative enhancement) over an optimal bilayer anti-reflective coating. We find a device efficiency which is only slightly lower than that of an ideal Lambertian absorber. We also find that the vacuum gap must be dimensioned according to the concentration factor of the solar irradiance. This work was published in [140]. [1]

[1] This work was done in collaboration with the IIT, *Istituto di Tecnologia*. In particular the optical simulation and the transport within the semiconductor were done at the IMM, while the charge cloud calculations where done by IIT.

5.1 Introduction

Power generating devices operating in extreme conditions are of great interest for pushing the current exploration limits in the solar system. An illustrative and highly challenging example is harvesting solar energy in a near Sun orbit. The upcoming European Space Agency's Bepi Colombo mission to Mercury (0.30–0.47 AU) [141] will be exposed to high-energy particle fields and light intensities of up to 10.6 suns, resulting in operating temperatures as high as 500 K. Standard space photovoltaic solar cell systems however exhibit degraded performance above a maximum steady-state operating temperatures of 420 K. For the future, even closer observation missions are planned [142], with ESA's Solar Orbiter at 0.28 AU and NASA's Solar Probe Plus set to perform multiple close approaches at 0.04 AU. At this distance, the surface temperature can easily reach 1700 K. In both concepts, specially screened photovoltaics are foreseen to be used during the outer part of the orbit trajectories, where the heat flux is considered manageable. Key to enhance mission performance is therefore to extend the capability to higher operating temperatures. In this study, we propose the use of a photon-enhanced thermionic emitter (PETE) [143] as an alternative to conventional solar cells with the capability to operate in a temperature range beyond 500 K.

In its original conception [144], a thermionic energy converter (TEC) operates as a thermoelectric device where a vacuum gap is introduced to preserve the temperature difference between the hot and cold terminals (see Chap. 13 of [145] for a historical review). The material removal has a detrimental impact on the current crossing the device given that the electrons must be emitted from the cathode to the anode instead of relying on the conventional drift and diffusion mechanisms and an electrostatic potential builds-up by the emitted electrons in the gap. Depending on materials, a practical TEC requires emitter temperatures in the range 1600–2000 K [146].

In the PETE design, Schwede et al. proposed to use a cathode comprising a semiconductor in order to increase the conduction band population through photon absorption [143]. In this way, the performance could be enhanced at lower temperatures by optimally combining thermal and photovoltaic processes. Fundamentally, the maximum attainable efficiency converges to the efficiency of a

solar thermal converter and can surpass 60% at a concentration of 1000 suns [147]. Very recently the efficiency limit has been reviewed by Segev et al. in [148] taking as a reference the Shockley-Queisser (SQ) limit [14]. The efficiency of an isothermal operating PETE device, can be described as a Metal Insulator Semiconductor (MIS) solar cell [149] which is bounded by the SQ limit. A PETE might exceed both the SQ limit and the ideal thermal limit if operated non-isothermally at high temperatures. However, Segev et al. recognize that the optimal operating temperatures largely exceeds the limiting temperature of actual semiconductor devices.

In this study, we discuss the feasibility of achieving a high efficiency PETE in the intermittent temperature range of 500–800 K. We concentrate our effort in providing an optimized cathode structure integrating photon absorption, carrier transport and surface emission. The photon absorption is enhanced with the help of a front light-trapping structure (LTS) based on a periodic photonic crystal. As cathode material we have considered GaAs, which is a reference material in solar cell technology. Even though other materials might perform better than GaAs at higher temperatures (e.g. GaN) their optical properties are not that well characterized as a function of the temperature, a critical element in the design of an LTS. In addition, GaAs exhibits excellent technological advantages, like ultra-low surface recombination velocity at the GaAs/GaInP interface [150] and therefore has been used in recent experimental realizations of PETE devices [151, 152] We have explored four different structures combining dielectric cones and cylinders. The structures are optimized using a device model with a 1D electronic diffusion model [153, 154] adapted for an arbitrary generation profile. A semi-analytical approach is taken which allows an efficient calculation of the PETE performance in the optimization procedure. For comparison, we made use of two ideal physical systems: a Lambertian absorber and a single pass Beer-Lambert absorber. They constitute the upper and lower limits in terms of light absorbed without reflection losses, respectively. The maximum efficiency expected for a GaAs based PETE operating at 700 K is close to 16% for an ideal Lambertian-like cathode of ∼30 nm. In a realistic PETE with a light-trapping structure this value reduces to 11% to 12% and the thickness increases to ∼225 nm. We find that the distance to the Sun, or equivalently, the concentration factor is critical in determining the dimensions of the vacuum gap. If it is larger than 10 μm, the PETE efficiency is smaller than

10% at a concentration of 100 suns. A larger vacuum gap would require a lower concentration factor to not quench its performance.

5.2 Physical model

The PETE device consists on a p-type semiconductor hot cathode and a cold metal anode. The light impinges at the front surface (transmission configuration, [155]) and the photogenerated electrons diffuse towards the back surface where subsequently the emission takes place. In this study, a light-trapping structure is positioned at the front surface. Figure 5.1 shows a scheme of the different parts of the device. Contrary to conventional solar cells, it is not possible to enhance the absorption in the cathode by placing a mirror at the back surface, because it would complicate the thermionic emission process. For efficient emission, the semiconductor should have low electron-affinity (χ), or alternatively, its surface should be subjected to a Cs treatment [156]. As a final process, the emitted electron will create a electrostatic potential in the vacuum region. In summary, the physical model consists of four different elements: (i) first to compute the photon absorption along the cathode to determine the generation rate from absorbed light; (ii) to calculate the carrier concentration at the emission surface and the emitted current; (iii) to compute the electrostatic barrier height in order to get the net emitted current. In the current study we have not considered the heat balance between the Sun and an eventual PETE panel as we want to identify the optimal operational conditions of the device. As any service module in a satellite, its optimal temperature range of operation would be granted through a thermal management system which would emit or retain the heat radiation as a function of the orbit position and orientation with respect to the Sun or a near planet.

5.2.1 Optical Absorption

The optical absorption is computed by means of the Fourier Modal Method (FMM). In this method the electromagnetic fields are expanded on an eigenmode basis. The structure is approximated by slices of constant refractive index along the propagation direction. On each slice a scattering matrix is defined that relates

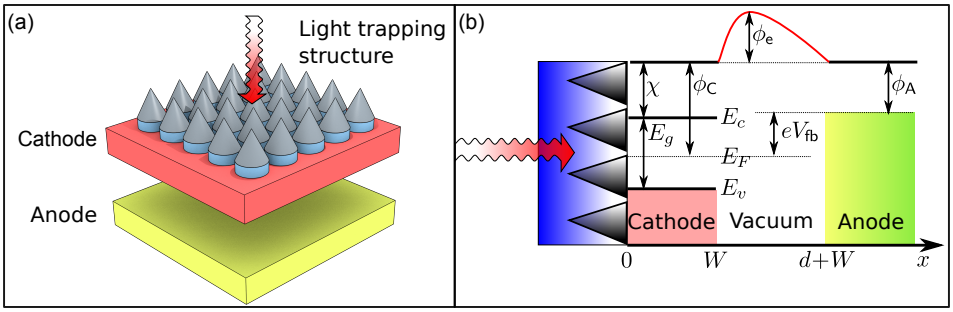

Figure 5.1: (a) Depiction of the different parts of a PETE device. Light impinges on the light-trapping structure (from above in (a) and from the left in (b)). (b) The band structure of the cathode and anode is depicted for a voltage at the flat-band condition. The red curve in the vacuum gap represents the charge-cloud electrostatic potential.

all the incoming channels with the outgoing channels. Combining the different scattering matrices allows to determine the scattering matrix of the full stack. This work uses the implementation of the method found in the open source software S^4 [101].

5.2.2 Transport model

A full description of the PETE transport model would require a 3D description of the generation process and drift-diffusion of the photogenerated carriers. This is a highly computationally demanding task. Andreani et al. have shown that to a great extent the device can be approximated by averaging the generation in the normal plane to the electron propagation direction [36]. In addition, finite-element-method simulations have also shown that the drift transport can be safely neglected in the range of voltages meaningful for the PETE [157]. To model the charge transport in the device, we have implemented the 1D diffusion model developed by Varpula and Prunilla [153]. The net current density results of the sum of the cathode and anode currents $J = J_C - J_A$. The current densities are described by the Richarson-Dushman equations [143]:

$$\begin{aligned} J_C &= A_C^* T_C^2 \exp\left(\frac{-\Delta E_C}{k_B T_C}\right) \frac{n}{n_{eq}}, \\ \Delta E_C &= \phi_C + \Theta(V - V_{fb}) e(V - V_{fb}), \end{aligned} \tag{5.1}$$

where A^*_C the Richardson constant, T_C the cathode temperature, k_B the Boltzmann constant, n the electron density at the emission surface, n_{eq} the electron density at equilibrium, ϕ_C the cathode work function and $\Theta(x)$ the Heaviside function. The work function is defined in terms of the electron affinity χ_C, conduction band edge E_c and Fermi energy E_F as $\phi_C = E_c - E_F + \chi_C$. The flat-band voltage is defined by the alignment of the cathode and anode work functions: $V_{fb} = (\phi_C - \phi_A)/e$. A similar expression to Eq. (5.1) is derived for the anode:

$$\begin{aligned} J_A &= A^*_A T_A^2 \exp\left(\frac{-\Delta E_A}{k_B T_A}\right), \\ \Delta E_A &= \phi_A + \Theta(V_{fb} - V) e (V_{fb} - V). \end{aligned} \tag{5.2}$$

Note that the expression of J_A corresponds to a pure thermionic emission and therefore the electron density is absent.

The electron density can be divided into two contributions, the electron density at equilibrium and the photogenerated electrons: $n(x) = n_{eq} + \Delta n(x)$. The diffusion law governing the electron transport can be expressed as [153]

$$D \frac{d^2 \Delta n}{dx^2} = \frac{\Delta n}{\tau} - G(x), \tag{5.3}$$

where D is the diffusion constant of the electrons, τ is the electron lifetime and $G(x)$ is the generation rate. A popular approach taken in the literature is to assume the generation created by the absorption of light following the Beer-Lambert law [153–155, 158]. In our case, the generation is computed from the x-component of the Poynting vector integrated over the area of the photonic crystal unit cell (S_x) obtained from the FMM:

$$G(x) = \int_{E_g}^{\infty} dE \frac{\Phi_{AM0}}{E} \left(-\frac{1}{S_0} \frac{dS_x}{dx}\right), \tag{5.4}$$

where E_g is the cathode bandgap, S_0 is the normalization flux considered in the FMM calculation and Φ_{AM0} is the zero air mass solar spectral irradiance. The solution of Eq. (5.4) is found after imposing the boundary conditions at the front

and back surfaces:

$$\left.\frac{d\Delta n}{dx}\right|_{x=0} = \frac{R_{S0}}{D}\Delta n(0), \tag{5.5a}$$

$$\left.\frac{d\Delta n}{dx}\right|_{x=W} = -\frac{R_{SW}}{D}\Delta n(W) - \frac{J}{qD}, \tag{5.5b}$$

where R_{S0} and R_{SW} are the surface recombination velocities of the front and back surfaces. The total current appears in the back boundary condition, meaning that there is a closed loop dependence between the excess carrier density and the net emitted current. The system of equations as formulated above is a boundary value problem (BVP) solvable with a mathematical symbolic software [159]. The integral of $G(x)$ in the cathode region is the only step that requires numerical evaluation. However, under high injection conditions ($\Delta n/p \gg 1$) the electron lifetime can not be assumed to be constant and its explicit dependence on radiative and Auger recombination processes therefore needs to be introduced in Eq. (5.3) thus resulting in a non-analytic BVP [154]. Although the numerical solution can be easily found, the computational cost of the optimization procedure is high. In this study the low injection condition is satisfied as can be seen in Fig. 5.5, where $n \ll N_{\mathrm{A}}$.

5.2.3 Space charge model

The charge cloud created by the emitted electrons can not be straightforwardly implemented in Eq. (5.3). Instead, we have independently solved the Poisson's equation to obtain the maximum of the electrostatic potential (ϕ_e) taking as starting point the saturation current (J at $V \ll V_{\mathrm{fb}}$) [146, 160]. Finally, we introduce ϕ_e in ΔE_c in Eq. (5.1) to recompute the JV curve introducing the reduction in the probability of emission due to the charge cloud. We will further develop this point in section 5.3.4.

5.2.4 Candidates to light-trapping structures

It has been already mentioned that we will rely on photonic structures to enhance the absorption in the cathode. In this way, a PETE with a thinner cathode can be used to minimize transport losses without sacrificing absorption. The front

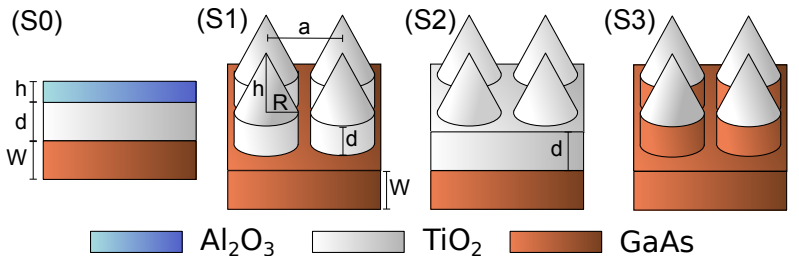

Figure 5.2: Sketch of the four structures proposed for light-trapping purposes. Each color corresponds to a different material.

material considered in the simulations is SiO_2, given that the PETE device needs to be encapsulated for protection from high energy irradiation. We have explored the performance of four different structures. We show a sketch of the different elements and materials defining each of the structures in Fig. 5.2.

A GaAs slab, as cathode, finished by an anti-reflective coating made of a bilayer (structure S0 in Fig. 5.2) will serve as a reference of the state-of-art technology employed in space for conventional solar cells. The other three structures include a photonic crystal of lattice parameter a. This photonic crystal contains two well differentiated layers. The top layer is common to all structures. It contains a dielectric cone of radius R and height h; a Moth-eye like structure which is well known to reduce the reflectance by reducing the refractive index mismatch between the SiO_2 cover and the GaAs cathode [46, 56, 69, 99, 118, 119]. The bottom layer is characteristic of each structure. In the structure S1, a dielectric (TiO_2) cylinder is placed below the top cone. Its presence is justified because this structure might help to increase the diffraction efficiency of higher diffractive orders, which are characterized by longer optical paths and hence a higher absorption in the cathode. In structure S2, the dielectric cylinder is substituted by a dielectric slab. We have seen in previous studies that a thin slab helps in coupling light to guided modes, which again will result in a higher absorption of the Sun light [69]. One problem of the structures S1 and S2 is the small refractive index contrast between TiO_2 and SiO_2. In general, the higher the contrast, the higher the diffraction effects. Therefore, we have considered structure S3, which is similar to S2, but the TiO_2 cylinder is substituted by a GaAs cylinder. In this structure, we are increasing the surface of the active device and therefore its surface recombination will be higher

Table 5.1: Parameters (Param.) and conditions used in the optimization. Parameters marked as † are extracted from [161]

Param.	Value	Param.	Value	Param.	Value
$D^{\dagger}$	200 cm^2/s	$m_n{}^{\dagger}$	0.067 m_e	ϕ_a	0.9 eV
R_{S0}	100 cm/s	$m_p{}^{\dagger}$	0.47 m_e	χ	0.4 eV
R_{SW}	0 cm/s	A_C	120 m_n = 8.04 A cm^{-2}	T_C	700 K
N_A	10^{18} cm^{-3}	A_A	120 A cm^{-2}	T_A	573.15 K
$\tau^{\dagger}$	5 ns	X	100 suns		

than in the case of the other structures. An additional shortcoming is that our 1D model can not accurately describe the transport along the cylinder. For this structure we have assumed that the cathode thickness is d+W instead of just W.

5.3 Results and discussion

5.3.1 Light-trapping structures optimization

The four photonic structures are optimized under the same conditions, using a global optimizer [108, 109] and the power ratio as figure of merit:

$$\eta^* = \frac{J(V_{\text{op}})V_{\text{op}}}{P_{\text{inc}}} \tag{5.6}$$

being V_{op} the operation voltage where the PETE delivers maximum power output and P_{inc} is the incoming solar irradiance.

The parameters defining the operating conditions of the PETE that we use in the optimization can be found in Table 5.1. To keep the model semi-analytic the lifetime and diffusion coefficients are kept constant in solving the output current. The surface recombination velocity at $x = 0$ is set to 100 cm/s.[2] On the other hand, the recombination surface at $x = W$ is taken as 0 cm/s, to illustrate that the emission rate dominates over the surface recombination. The anode temperature, T_A, is set to 573.15 K. Keeping the anode at a high temperature may allow to introduce

[2]This can be achieved using back surface field (BSF) [149, 154], or chemical surface passivation [162].

an auxiliary Carnot machine using another cold point to increase the final PETE efficiency [143]. A thorough analysis of the PETE performance for different values of χ, N_A, and X is reported in [153, 154]. In our study, we will take as realistic values $\chi = 0.4$ eV, $N_A = 10^{18}$ cm^{-3} and $X = 100$ suns. The latter might represent either the increase of the solar irradiance in a near Sun orbit or an optical concentration system or a combination of both. The cathode temperature is kept fixed at 700 K if not said otherwise. Later, the effect of the temperature will be analyzed between 350 K and 1000 K. We have verified by a simple thermal energy balance that this temperatures might be achieved at $X = 100$ suns. Similarly to [158] we have considered as source the incoming solar flux and as drain the work used to extract the electrons form the cathode, the radiation losses (assuming the cathode as black-body at temperature T_C with emissivity from E_g to higher energies, P_0) and an additional ideal IR coupler (also a black-body but with emissivity up to E_g, P_{IR}):

$$P_{inc} - J[\phi_C + \Theta(V_{op} - V_{fb})(V_{op} - V_{fb})] = P_0 + P_{IR}. \tag{5.7}$$

The equilibrium temperatures are 1000 K and 1100 K if the IR coupler is present or absent, respectively. Hence, the analysis shows that the solar flux provides enough power to cover the temperature range of our study.

The optimization of the size parameters corresponding to each structure is bounded between the following limits. The lattice parameters vary between 100 nm to 1 μm. The filling factor, defined as the ratio between the diameter of the cylinder and the lattice parameter, varies between 0.25 to 1. The height of the cone and cylinder share the same bounds between 0 μm to 1 μm. The cathode thickness is bounded between 1 nm to 20 microns. Finally, the spectral range chosen in the optimization spans from 1 eV to 4 eV, i.e. 310 nm to 1240 nm. It covers 80% of the solar irradiance AM0. The other 20% distributes as 1% at higher energies and 19% at lower energies. The lower energy contribution of the solar irradiation can not be directly absorbed by the semiconductor, therefore it has been proposed to use an infra-red filter as a heating system. The higher energy contribution can be absorbed by the semiconductor, but as we will see, at such high energies also the dielectrics compete in absorption. Once the upper and lower bounds are set, the optimizer evaluates directly η^* under the operating conditions defined in Table 5.1. The optimal parameters found by the optimizer are shown in Table 5.2 together

Table 5.2: Optimal dimensions of the PC ARCs and their corresponding efficiencies and ultimate efficiencies.

System	a (nm)	R (nm)	h (nm)	d (nm)	W (nm)	η^*	η_{ue}
S0	-	-	67.1	43.8	348	10.12	33.35
S1	584	292	814	21.7	224	11.48	34.97
S2	612	292	847	27.2	220	11.72	35.57
S3	387	147	123	209	28.4	12.43	38.25

with the η^* value. In addition, we have introduced the corresponding value of the ultimate efficiency η_{ue} [14]. This figure of merit is very popular in the design of optical coatings for conventional solar cells and it will serve to highlight the particularities of the PETE optimization.

As expected, Table 5.2 reveals that the introduction of a photonic crystal results in an increase of the PETE efficiency with respect to the bilayer structure, which constitutes the state-of-the-art in terms of optical coating. Structures S1 and S2 exhibit a very similar performance. Their size parameters are also very close in value, with a slightly larger lattice constant for S2. The absence of a cylinder as scatterer in S2 leads to a weaker diffraction, which is compensated by a larger lattice constant and a taller cone. Structure S3 brings remarkable differences with respect to structures S1 and S2. The lattice constant and filling factor are significantly smaller, a reduction of $\sim 35\%$ and $\sim 50\%$, respectively, and thus S3 mostly operates in the sub-wavelength regime. Another relevant feature of S3 is that it contains less TiO_2 than S1 and S2, which means smaller losses due to absorption in the dielectric. S1 and S2 present similar optimal thicknesses around 220 nm. It is remarkable that this value is around 38% thinner than the optimal value found for the bilayer. This is also the case for S3, $d + W = 237$ nm. However, a better comparison is obtained with the GaAs volume to unit cell area, $W + \pi R^2/a^2 d = 123$ nm. Meaning that S3 contains roughly a 50% less GaAs than S1 and S2. This result is very well known in the design of optical coatings for solar cells, as nanowire absorbing structures are extremely efficient [163, 164].

We show in Fig. 5.3 the optical absorption of the different structures. From a qualitative point of view, it is possible to recognize the diffractive character of S1 and S2, where the spectrum shows sharp resonances at low energies. The S3 spectrum,

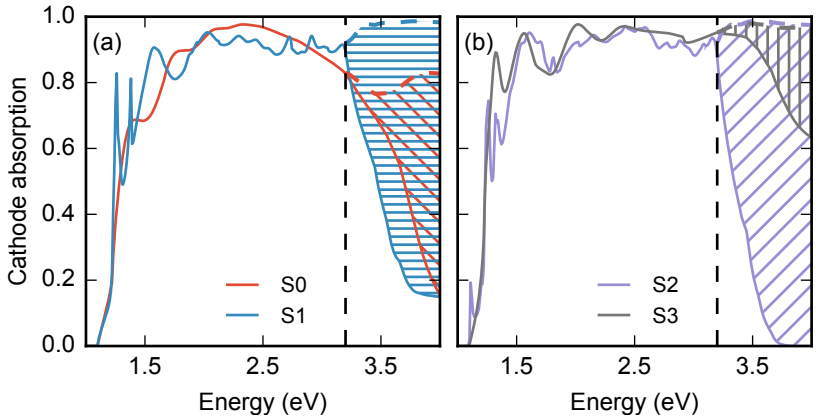

Figure 5.3: (a) Absorption in the cathode for the S0 (red) and S1 (blue) structures. The area between the dashed and the continuous line represent the losses due to the absorption of the TiO_2. The hatched area correspond to the losses of the S0 and S1 structures respectively. (b) Absorption in the cathode for the S2 (purple) and S3 (gray) structures. The area between the dashed and the continuous lines represents the losses due to the absorption of the TiO_2. The hatched area correspond to the losses of the S2 and S3 structures respectively. The vertical dashed line correspond to the gap of the TiO_2 at 300 K

instead, shows more smooth peaks typical of sub-wavelength structures. The ultimate efficiency η_{ue} results very helpful in comparing the absorption performance of each structure. From Table 5.2, there is a clear correlation between the η^* and η_{ue}, hence the higher the absorption, the higher the PETE efficiency. However, if we keep all the size parameters constant and let grow d and/or W, η_{ue} keeps increasing up to its maximum theoretical value ($\eta_{\text{ue,max}} = 43.5\%$), while η^* reduces monotonously. The optimization of η^* takes into account the loss of electrons in the diffusion process across the cathode. A further analysis of Fig. 5.3 permits to quantify the amount of light absorbed by the TiO_2. The dashed vertical line indicates the TiO_2 band edge. The dashed colored lines represent the absorption for a lossless TiO_2. Hence, the losses in the dielectric are the hatched areas. The losses are more critical in S1, and S2, whereas S3 does not present this problem. In our case the TiO_2 refractive index were temperature independent, therefore it is expected that the band-edge would red shift in a real device. We can conclude that S3 is the best solution as light-trapping structure as long as a dielectric of larger bandgap than TiO_2 at equal refractive index is not available.

5.3.2 Effect of the cathode thickness and temperature

The S0 structure strategy to enhance the absorption is to minimize the reflection losses. The strategy of structures S1 to S3 is two-fold. It consists in reducing the reflection losses together with increasing the optical path. The physical grounds of these two strategies can be represented by two different ideal physical models [91]:

- A single pass Beer-Lambert absorber (BLA) without reflection. The Poynting vector in a BLA is defined as:

$$S(x)_{\mathrm{BLA}} = \exp[-\alpha(E)\, x], \tag{5.8}$$

  where $\alpha(E)$ is the absorption coefficient.

- A Lambertian absorber (LA), also without reflection. For an LA, the Poynting vector is:

$$S(x)_{\mathrm{LA}} = \frac{1}{4n^2\alpha(E)x + 1}. \tag{5.9}$$

The evolution of η^* with the cathode thickness is shown in Fig. 5.4(a). We have kept fixed all size parameters except W. For the structure S3, we have assumed as cathode thickness the sum $d + W$, but keeping the same ratio d/W as in the case of the optimal structure of Table 5.2. The efficiency of S0 increases with W up to a thickness of ≈350 nm. For thicker cathodes the efficiency drops. The good agreement between S0 and BLA indicates that the absorption increases in the cathode up to a thickness where all the incoming light gets absorbed. For larger values of W there is no additional generation and the loss mechanisms in transport are the cause for the efficiency drop. The shoulder appearing at ≈25 nm is a resonance peak due to the zero-frequency Fabry-Perot mode [165]. The efficiency of S1 and S2 follows a very similar trend. As expected, the dielectric photonic crystal structure helps in increasing the absorption in the cathode reaching a clear maximum at the optimal W. For these structures it is also possible to identify the zero-frequency mode at ≈ 25nm. Structure S3 only outperforms S1 and S2 in the neighborhood of the optimal W. The photonic crystal parameters are independent of W in cases S1 and S2. However, in the S3 case the GaAs cathode is nanostructured, and thus a change in cathode thickness implies a change in

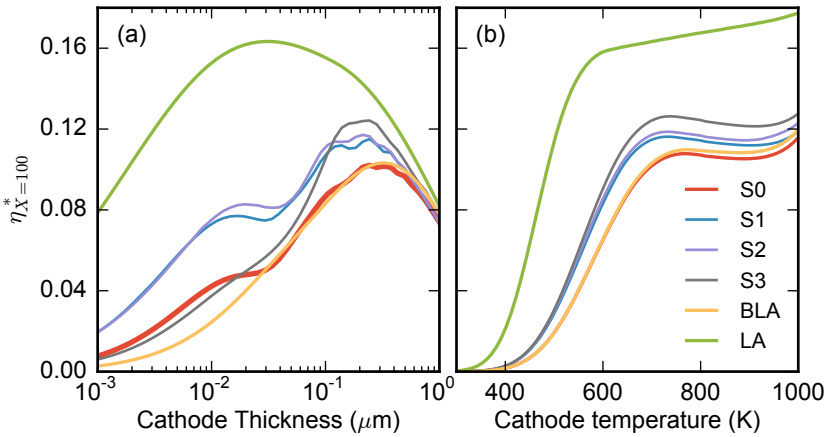

Figure 5.4: (a) Evolution of the power output with the thickness of the cathode for the four systems simulated, S0-S3. A Beer-Lambert like cathode and a Lambertian like cathode, are included as different physical limits of the absorption. The temperature is set to 700 K. (b) Evolution of the power output with the temperature of the cathode for the four systems simulated. A Beer-Lambert like cathode of thickness 350 nm and a Lambertian like cathode, thickness of 30 nm are included as different physical limits of the absorption.

the diffraction efficiency of the nanostructure. In other words, the cathode total thickness in S3 is the cylinder height and the cathode thickness, i.e. $d + W$.

The LA efficiency is above all structures and can be considered as a top physical limit. It exhibits a maximum for thinner cathodes than in all other cases. The fact that the maximum efficiency of S3 gets very close to the LA efficiency shows the good performance of the structure as anti-reflective coating. This is a known behavior of photonic crystals based on cones [46, 69, 99, 118] Finally, for $W > 1$ μm all models converge and follow the same trend.

In Fig. 5.4(b), we show the evolution of the efficiency with the cathode temperature. The shape of the curves is similar for all the structures. At low temperatures the efficiency is low because the electrons do not have enough energy to overcome the escaping barrier, (ΔE_C in Eq. 5.1) and the reverse current from the anode (at T_C = 573 K) dominates. At higher T_C, the efficiency grows exponentially in accordance with J_C up to its maximum value. From this point, the generation process is not powerful enough to keep a high current and only the LA keeps increasing with T_C. Only at very high temperatures (higher than 900 K) the n_{eq} is high enough

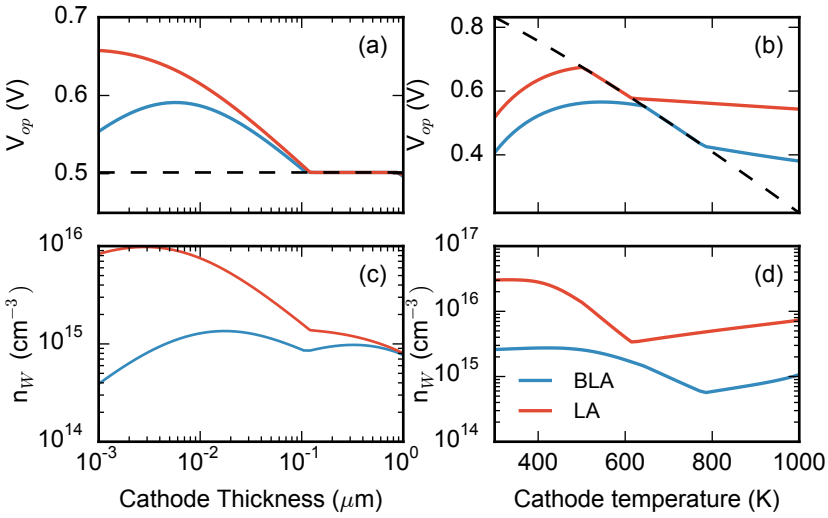

Figure 5.5: Evolution of the operating voltage with the thickness (a) and temperature (b) of the BLA (red) and the LA (blue). The dashed line corresponds to V_{fb}. Evolution of the electron density at the emission surface with the thickness (c) and temperature (d).

to allow the electrons to escape from the cathode ("purely" thermionic emission). Structures S0-S3 and BLA show a reduction in efficiency attributed to the drop in voltage. The bandgap of the semiconductor reduces with the temperature and consequently the voltage at flat-band gets also reduced. We will come back to this point when discussing the internal operation of the PETE in Fig.5.5.

To get a full understanding of the efficiency of the PETE it is customary to look at the evolution of the internal variables of the device, namely the operation current density and voltage and the carrier density at the emission surface. We have constrained this analysis to the two physical models BLA and LA, as the actual structures exhibit an intermediate behavior. The evolution of the current density follows qualitatively the same trends as the efficiency, therefore we have omitted the corresponding plots. The evolution of the voltage with T_{C} was analyzed in [154]. We show the results for the BLA and the LA in Fig. 5.5(b). Naively thinking, the operating voltage would be V_{fb}, i.e. when the barrier for the emitted electrons is minimal $\phi_{\mathrm{C}} = \phi_{\mathrm{A}}$. However, for low T_{C} the anode is hotter than the cathode and there exists a reverse current. To get a positive efficiency the system is forced to operate below V_{fb}, i.e to lower ϕ_{A}. Once the temperature difference reduces, the

operating voltage reaches the flat-band condition. At even higher T_C, n_{eq} grows and the electrons might overcome a higher energy barrier. This means that the PETE is able to operate at voltages higher than V_{fb}. The difference between the values obtained for BLA and LA is due to a higher electron density in the cathode of the Lambertian absorber. Hence, the higher the absorption, the higher the voltage.

The dependence of the voltage with W is shown in Fig. 5.5(a). In this calculation $T_C = 700$ K, meaning that n_{eq} is high enough to operate above V_{fb}. Therefore at low W the voltage is above V_{fb}. Surprisingly, at higher thicknesses the voltage drops to V_{fb}. Focusing in the LA case, the current density increases with W up to a critical thickness were the absorption saturates and the losses in the bulk reduce its value. As the current density can be seen as a loss mechanism in the boundary conditions in Eq. (5.5), it means that $n(W)$ should decrease with W. Indeed, this decrease can be seen in Fig. 5.5(c). As J_C is proportional to $n(W)$ the only way to enhance the current density is by lowering the voltage, approaching it to V_{fb}. The case of the BLA can be understood in similar terms, but the drop in voltage follows a previous rise related with "slower" increase of the current density as happens with a weaker absorber. For the sake of completeness Fig. 5.5(d) shows $n(W)$ as a function of T_C. There the situation is slightly different, because the system is restraining the reverse current density J_A at low T_C. At high T_C, there exists a threshold due to thermal excitation of electrons across the band-gap. As a final remark, the dependence of the voltage with T_C is analyzed in [154] for different concentration factors showing similar results to those of Fig. 5.5(b). Hence, a change in the concentration factor can be also interpreted as a change in the absorption strength.

5.3.3 Refractive index temperature dependence

One of the key material parameters of our study is the permittivity or, equivalently, the refractive index. GaAs is one of the few semiconductor materials thoroughly studied from an optical point of view in a broad temperature range. Its optical response is characterized by a series of high absorption peaks, related with the Van Hove singularities of its electronic band structure [166]. The impact of the temperature on the refractive index is a red shift of the resonance positions and an increase of their spectral width. An ab-initio calculation of the linear response as a function of the temperature still represents a computational challenge [167,

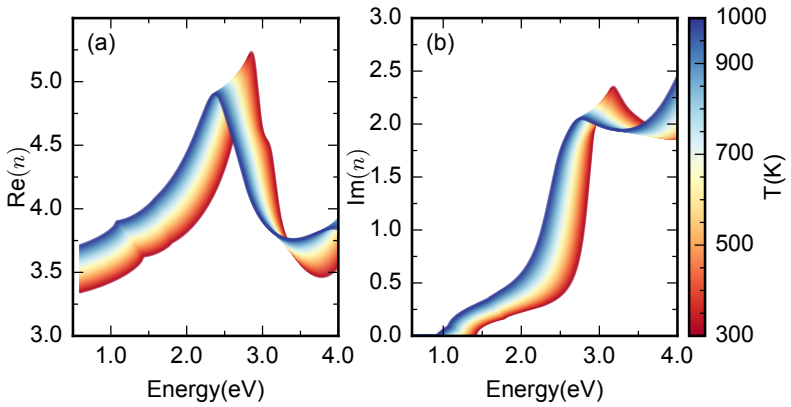

Figure 5.6: Evolution of the real (a) and imaginary (b) part of the refractive index with the temperature. The color gradient from red to blue corresponds a temperature gradient from to 300 K to 1000 K.

168] out of the scope of the present work. Nevertheless, it is possible to get an accurate description relying on a simple empirical model [169]. We have neglected the impact of excitonic effects in our analysis, given that we are targeting very high temperatures. In Figure 5.6, we show the evolution of the real and imaginary part of the refractive index with within a temperature range of 300 K to 1000 K. The most noticeable changes in the spectral range of interest is the red shift of the fundamental bandgap (Γ point, E_0 transition) and the absorption along the Γ-L line (Λ line, E_1 transition). At higher energies there are two additional transitions E_2 (X point) and E_0' (excited conduction band at the Γ point).

The change in the absorption spectrum of the optimal structures is depicted in Fig. 5.7(a)-(c). We have not shown the corresponding spectra of structure S1, because qualitatively it is similar to that of S2. It is common to all structures the red shift of the fundamental bandgap. In fact, the increase in broadening and value of $\mathrm{Im}(n)$ gets reflected as the increase in the absorption with the temperature in the low energy part of the spectrum. The rise of $\mathrm{Im}(n)$ at high energies (E_2 and E_0' transitions) is hindered by the absorption of the TiO_2, which starts to absorb from 3.2 eV onwards, as discussed above. The general trend is therefore a rise of the absorbed light with temperature for energies below 2.5 eV and an almost insensitive absorption for higher energies. The effect of the temperature on the absorption can be quantified by looking at the ultimate efficiency (η_{ue}). Fig. 5.7(c) shows the

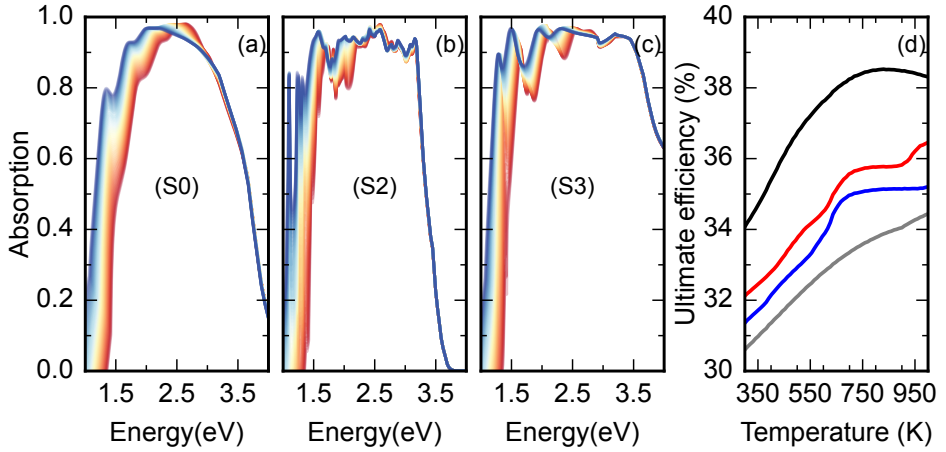

Figure 5.7: Change in the optical absorption as a function of the temperature for the optimal structures S0 (a), S2 (b) and S3 (c) defined in Table 5.2. The dependence of the complex refractive index is depicted in Fig. 5.6. The color gradient from red to blue corresponds a temperature gradient from to 300 K to 1000 K. (d) The ultimate efficiency as a function of the temperature for the optimized structures (S0 gray line, S1 blue line, S2 red line and S3 black line).

corresponding values for each of the structures. It is clearly identifiable the increase in η_{ue}, directly related with the absorption, in all structures. While the bilayer structure (S0) shows a linear-like increase with the temperature, S1 and S2 show step changes in slope. This is related with the excitation of resonances appearing at low energies [Fig. 5.7(b)]. The behavior of structure S3 instead shows a clear maximum at 800 K, very close to the temperature used in the optimization, 700 K (see Table. 5.1). Hence, the evolution of the refractive index with the temperature needs to be taken into account explicitly to get an accurate description of the optical absorption. Alternatively, one could have taken the refractive index at 300 K and shift it according to the fundamental band-edge. Such approach would imply an underestimation of the total absorbed light.

5.3.4 Charge-cloud effects

In an ideal PETE device, the totality of the emitted electrons from the cathode will reach the anode and vice versa. However, as it has been already mentioned, the vacuum gap is not a ballistic channel for the emitted electrons. Intuitively, emitted

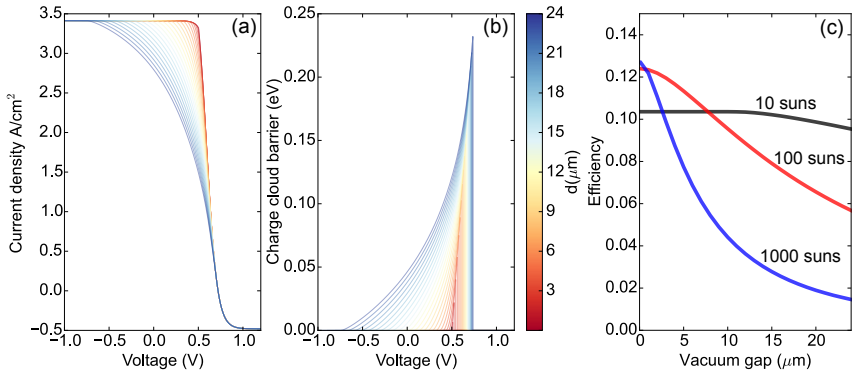

Figure 5.8: Evolution of the JV curve (a) and ϕ_e (b) of the optimal S3 PETE as a function of the vacuum gap distance. (c) Total efficiency as a function of the vacuum gap distance for three different concentration factors: 10 suns (black line), 100 suns (red line) and 1000 suns (blue line).

electrons will interact electrostatically with one another. The result is that some of the electrons reflect back to the cathode. Depending on the applied voltage, there is a point in the space between cathode and anode of maximum probability of backscattering in the steady state. Such maximum has been depicted in the energy level structure of Figure 5.1 by the electrostatic potential maximum ϕ_e. Beyond this point, the electrons reach the anode balistically. A rigorous description of this problem is based on the Langmuir space charge theory [170], which has been successfully adapted to the case of thermionic emitters [146] and PETE [160]. The value of the applied voltage plays a critical role in the final profile of the electrostatic potential and three regimes are clearly identified: (i) Saturation point: the voltage V_S is such that $\phi_C \gg \phi_A$ and ϕ_e is located within the cathode physical space; (ii) Critical point: the opposed situation, the voltage V_C is such that $\phi_C \ll \phi_A$ and ϕ_e is located within the anode physical space; (iii) Space charge limited regime: this is the intermediate regime depicted by the red line of Figure 5.1. We have followed the numerical procedure described in [146, 160] to determine the value of ϕ_e as a function of the voltage given a certain saturation current and a vacuum gap distance. However, they assumed in their work that the operating current density in the space charge limited regime is $J(V) = J_C \exp\{[-\phi_e(V)]\}$, which is valid for a thermionic emitter but only an approximation for PETE. We showed in Eq. (5.1) that the current density depends on the electron concentration n and in

Eq. (5.5) that Δn also depends on the current density. The solution of this system of equations would require a self-consistent solution scheme at each value of the voltage. Instead, we have adopted an approximate solution. We first calculate the saturation current J_C as described in Section 5.2. The potential barrier $\phi_e(V)$ is calculated only once for this maximum current density supplied by the PETE. Then, we introduce $\phi_e(V)$ in the exponential of the current density [ΔE_C in Eq. (5.1)] and recompute the JV curve.

We show in Figure 5.8(a) the change in the characteristic JV curve of the S3 PETE as a function of the vacuum gap distance and in Figure 5.8(b) the corresponding value of ϕ_e. In the limit of zero vacuum gap, the JV curve is exactly the same as that of the ideal PETE; all the emitted electrons reach the anode seamlessly. The drop in current takes place close to the flat-band voltage (indicated by the vertical line for $\phi_e = 0$). For this vacuum gap $V_S \approx V_C \approx V_{fb}$ and $\phi_e \approx 0$. When the vacuum gap distance increases, the drop in the current density takes place at lower voltages, mostly governed by the value of the saturation voltage V_S. The barrier ϕ_e starts to increase accordingly. To get a broad picture on the impact of ϕ_e on the performance of the device, we have depicted in Figure 5.8(c) the evolution of the PETE efficiency with the vacuum gap distance. The reduction in efficiency at a concentration of 100 suns (default conditions) is very slow for a very thin gap, from 0 μm to 3 μm. For wider gaps, the drop follows an almost linear decrease. This effect is tightly related with the amount of photogenerated and emitted electrons. Therefore changes in the concentration factor have a great impact on the performance of the device. Higher concentrations produce higher current densities and, in accordance, faster reductions in performance with the vacuum gap distance (see blue line for 1000 suns). The opposite behavior is found for lower concentration factors. It is possible to keep a constant performance up to 25 μm gap for 10 suns. The technology employed in the fabrication of the PETE device would critically determine the optimal concentration factor to avoid sacrificing the performance of the device. For sub-micrometer to a few micrometers gap, high concentration provides the best performance. For technology involving larger vacuum gaps a low concentration factor is mandatory. In contrast to TECs, where $T_C \neq T_A$, a PETE can operate in an isothermal configuration. Thus, a device with a narrow vacuum gap would not have a large adverse effect due to the near field heat exchange [166].

5.4 Conclusions and outlook

The description of a PETE with a light-trapping structure required a model able to cope with an arbitrary generation profile and a full description of the complex refractive index as a function of the temperature. We have focused our analysis on two parameters only, the cathode thickness and its temperature. The photonic crystal structures provides an ≈12% efficiency at thicknesses around ≈225 nm. This value is very close to the physically ideal system of non-reflective Lambertian absorber. There is still room for improvement, given that a 16% efficiency might be achieved for a very thin absorber (≈ 25 nm). Further research is required to achieve such value. At low temperatures, the PETE offers a maximum performance at smaller temperatures than the anode (≈ 525 K and 573 K, respectively). As reported in [143, 154, 157], a higher efficiency is attainable by heating up the cathode beyond 1000 K. However, such temperature regime is far beyond of the operational temperature limit of GaAs devices. The role of the charge cloud created by the emitted electrons also plays a strong constrain on reaching an efficiency above 10%. We found that the concentration factor is critical in determining the optimal vacuum gap distance. Keeping it bellow 100 suns allows for a vacuum gap narrower than 10 μm, while higher values required much narrower channels.

The efficiency values reported here are greater than those of a single junction GaAs solar cell in the SQ limit at temperatures above ≈ 1000 K. Clearly, the combination of photovoltaic and thermal conversions is critical for the PETE to outperform a standard solar cell. However, such crossover needs to be moved to lower temperatures for practical applications to be attractive. At the same time, it offers technological advantages. The extraction of electrons and holes can be done selectively and no pn junction is required [157, 171]. This prevents problems related with the migration of dopants and the removal of the built-in voltage for carrier separation. Problems related with the diffusion of contacts are common to solar cells and PETEs. A feasible way to enhance the efficiency of the PETE is to rely on semiconductors of broader bandgap. Indeed, the optimal bandgap is around 1.4 eV [143]. An additional benefit is the increase of the effective mass with the bandgap providing higher values of the Richardson-Dushman constant A^*. However, the electron-affinity also increases with the bandgap, requiring a more effective Cs treatment.

In terms of space applications, the reported PETE shows to be competitive with existing technology when targeting high intensity solar radiation and high temperatures. Even though previous tests [172] reported concentrator cells with 18% of AM0 efficiency surviving 7 minutes at 870 K, solar cells show a substantial decrease in efficiency above 370 K. For example, typical InGaP/GaAs/Ge triple junction solar cells with efficiency $\eta = 26\%$ at $T = 300$ K and with linear normalized temperature coefficient $\beta = (1/\eta)(d\eta/dT) = -4.5 \times 10^{-3}\ \mathrm{K}^{-1}$ [173] are expected to have an efficiency of 11% at 420 K (average temperature orbiting Mercury under a solar concentration factor of ~ 10 suns [141]). At 440 K the efficiency is already below 10%. Single junction GaAs on Ge solar cells with lower β show a drop of efficiency from 17.6% (300 K) to 14% (420 K) [172] and for $T = 530$ K and higher, besides the poor thermal stability of the system, the efficiency drops off below 10% resulting in decreased performance. A PETE system working at 10% efficiency would therefore be advantageous above temperatures of 570 K meaning either transit in Mercury perihelion or solar probe like missions. Further, previous studies on high temperature solar arrays [172] showed that better solar cell survivability can be achieved through changes to the contact metallization and through the use of diffusion barriers in the GaAs cells. The same improvement could be applied to PETE, in order to extend the thermal stability of the device during operation.

Chapter 6

Conclusions

In this thesis we have demonstrated that using photonic crystals can potentially increase the efficiency for III-V solar cells. Also, we have demonstrated that light trapping is fundamental for non-conventional solar thermo-ionic cells.

In Chapter 2 we have demonstrated that for a concentrator GaAs solar cell (1 μm thick) we are able to reduce optical losses by increasing the efficiency 3.6% compared to the conventional interferencial coating, and only 0.5% below an ideal solar cell with zero reflectance losses. To achieve this we have to nanostructure the front and back layer, without damaging the III-V active semiconductor. In this chapter we have also studied how the emittance of the solar cell is affected by the photonic crystals. A small voltage penalty could appear for ultra thin devices when the radiative recombination dominates.

In Chapter 3 we design a broadband antireflective nanostructure for tandem solar cells. It was a challenge because the spectral range (350-1800 nm) comprises two optical regimes, one where the photonic crystal acts as an effective index medium, and the other as a diffractive structure. The nanostructure presented was globally optimized and it was simple enough to be fabricated, as we demonstrated on Chapter 4. For this broadband scenario we have shown that, in comparison with a standard bilayer ARC, the power losses due to reflectivity can potentially be lowered by a factor of more than 4 to an absolute value below 1% of the incident power.

The fabrication presented on Chapter 4 is compatible with large-area fabrication. In particular, the laser interferometric lithography presents the fundamental advantage of being able to be easily scalable to large areas. Finally, another

advantage is that this process is mask-less which facilitates its combination with preexisting patterns on the sample such as solar cell electrical contacts. The experimental setup designed and built is detailed in Appendix A.1.

In Chapter 5 we have used a combination of the strategies presented in the other chapters to model and optimize a photo enhanced thermo-ionic emitter. This is not a typical photovoltaic device as the carriers are emitted from a semiconductor cathode to a metallic anode through a vacuum gap. These PETE devices require ARCs and light trapping nanostructures of similar characteristics to those used in photovoltaic devices. In PETE devices the light trapping schemes are necessary to achieve efficiencies above the 10%, and therefore they are needed to assure their viability.

We have learned that the benefits of photonic crystals in photovoltaic devices are based on two different effects. The first is known as the effective index. It allows to tweak the refractive index of the nanostructured layer, leaving more degrees of freedom than for homogenous materials and allows for a gradual index increase along the light propagation direction. The second effect is related to light coupling to resonant modes present in the photonic crystal, enhancing the transmission to the substrate.

It is not clear if a more complex design, like designing a quasi random structure in the k-space,[54, 55] could increase the efficiency enough to justify a more complex fabrication. In the case of using the nanostructure as an antireflective coating, and after the results presented in Chapter 3 with 99% of transmittance, there is almost no room for improvements in the design. Still, an optimized fabrication process is needed to reach the full potential of the designs here proposed. Another important point to acknowledge is that this design was done for air as incident medium. If the incident medium has a higher refractive index, like silica for example, the size of optimized the unit cell may be reduced. Therefore, to keep the resonant modes of the structure a dielectric with a higher refractive index (and possibly higher absorption losses), such as SiC, might be needed.

The case of a higher index incident medium has been explored in Chapter 5 for PETE devices. In the case of PETE devices there is a requirement for increased absorption that may be satisfied by using photonic crystals with a higher difraction efficiency. In fact, this device can achieve a 16% of efficiency using ultra thin GaAs

layers. PETEs are still in an early state of development and more research is needed to assess the viability of these devices, but one of the important tasks is to design a light trapping structure capable of near full absorption with thicknesses below 100 nm.

In summary, engineering the optical response of any solar technology is critical if we are after achieving high efficiencies. Photonic crystals are suitable for obtaining near optimal optical response, as we have a lot of leeway in the design. The results in this thesis underpin the idea that using relatively simple photonic crystals we are able to optimize the optical response of the solar cell.

Appendices

Appendix A

Experimental Methods

In this Appendix the experimental methods used in Chapter 4 are presented. In particular, the laser interferometric lithography setup is detailed, highlighting the advantages and limitations of this technique. Also, the experimental setup used for the reflectance measurement is detailed. The other techniques here presented are widely known and used in micro and nano fabrication, thus, they are briefly described. The particular process for each method used in this thesis is detailed.

A.1 Laser interferometric lithography for photonic crystal fabrication

The laser interferometric lithography (LIL) is a maskless lithography where two optical coherent beams interfere and generate a pattern. This pattern is used to expose a photoresist and to ultimately transfer the pattern by attacking the sample or by deposition and lift-off. One advantage of mask-less techniques is that they are compatible with preexisting patterns such as solar cell electrical contacts. Furthermore, it does not present the problems associated with template degradation by particle contamination that are often associated with for example nano-imprint and contact photolithography. Moreover, the main advantage of LIL compared to other maskless lithographies, as the electron beam lithography (EBL) or the focus ion beam (FIB), is the low cost when patterning large areas.[123, 124]

However, there are limitations designing the pattern. Usually two beams are used, which generate fringes, namely a 1-D grating. The sample has to be exposed twice to make a 2-D structure, rotating 90 degrees for each exposure. A combination of more than two interference beams, or incremental exposures, can be used to generate more sophisticated patterns.[174–177] However, this obviously increases the complexity of the process. In general, the pattern designs are more constrained than for example in EBL. This limitation was not a problem in this thesis as the structures optimized were square lattices and the aspect ratio and filling factor are controlled by the etching step.

The LIL used in this thesis is based on a Lloyd interferometer.[178] It was designed for relatively small areas, around the square centimeter, for prototyping. Also, we kept the size of the setup small on an optical table of 30×45 cm^2. The small distances allow us to use a relatively low power diode laser, 12 mW, with 405 nm to generate the pattern. The experimental setup was inspired on Ref. [179]. The main innovation in our set-up is the use of an integrated photodiode for exposure dose control. The total cost of the set up was below 6 k€. This section is organized as follows: firstly, the physics behind the LIL and its fundamental limitations are detailed; secondly, the particular design of the setup built with some fabrications examples and processes are presented; finally the possible improvements for this setup are discussed.

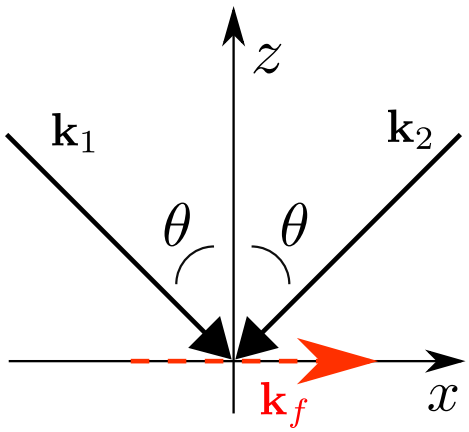

Figure A.1: Interference between two symmetric planewaves, $\mathbf{k}_1$ and $\mathbf{k}_2$, which generate an interference pattern with wavenumber $\mathbf{k}_f$.

A.1.1 Interference between two planewaves

The intensity distribution of a planewave is proportional to the square of the electric field in the medium. For a single planewave the intensity is homogeneous. However, the sum of two planewaves with different phases leads to an interference pattern. It is easy to see using the exponential form:

$$\begin{aligned} \mathbf{E}_1(\mathbf{r}) &= E_1 \exp(j\mathbf{k}_1\mathbf{r}), \\ \mathbf{E}_2(\mathbf{r}) &= E_2 \exp(j\mathbf{k}_2\mathbf{r}). \end{aligned} \tag{A.1}$$

The intensity then is:

$$\begin{aligned} I_{\text{total}} &= |\mathbf{E}_1(r) + \mathbf{E}_2(r)|^2 = \\ &= I_1 + I_2 + 2|E_1E_2| \cos[(\mathbf{k}_1 - \mathbf{k}_2)] = \\ &= I_1 + I_2 + I_{|12|}; \end{aligned} \tag{A.2}$$

where $I_1 = E_1^2$, $I_2 = E_2^2$. The interference term $I_{|12|}$ is the responsible of the pattern.

We can simplified for the particular case used, see Fig. A.1, where:

- the polarization of the electric field of both planewaves are parallel,
- the wavevector $\mathbf{k}_1$ and $\mathbf{k}_2$ are symmetric about z-axis.

In this case:

$$\begin{aligned} \mathbf{k}_1 &= k_0(k_x, 0, k_z), \\ \mathbf{k}_2 &= k_0(-k_x, 0, k_z). \end{aligned} \tag{A.3}$$

We can define a fringe-vector, $\mathbf{k}_f$:

$$\mathbf{k}_f = \mathbf{k}_1 - \mathbf{k}_2, \tag{A.4}$$

and we obtain the period of our pattern P_f:

$$P_f = \frac{2\pi}{|\mathbf{k}_f|} = \frac{\lambda}{2\sin(\theta)}. \tag{A.5}$$

we obtain P_f, which is the period of our pattern.

Thus, from Eq. (A.5) it is easy to extract the minimum period possible, which is the half wavelength, $P_{\min} = \lambda/2$. However, this period is a limit only reached asymptotically when both incident waves are parallel to the mirror.

Generally, the intensity of the pattern does not limit the lithography as the photoresist can be exposed more time if needed. Still, the definition of the pattern can be limited by the mechanical stability of the system and the background radiation. On the other hand, the intensity of each beam plays a decisive role in the interference pattern. These intensities will affect the difference between the maximum and minimum in the interference pattern, where the latter can be greater than zero. We will define the contrast C as:

$$C = \frac{I_{\max} - I_{\min}}{I_{\max} + I_{\min}}. \tag{A.6}$$

For a system with real amplitudes and $I_1 \neq I_2$: $I_{min} = I_1 + I_2 - 2|E_1E_2|$ and $I_{max} = I_1 + I_2 + 2|E_1E_2|$. Therefore, the different intensities of each beam can be a limiting factor for the lithography as the contrast depends on them. In particular, we have used the Lloyd configuration, where a mirror is used to reflect one of the electric fields and the other beam falls directly upon the sample. The reflectivity of the mirror will limit the final contrast.

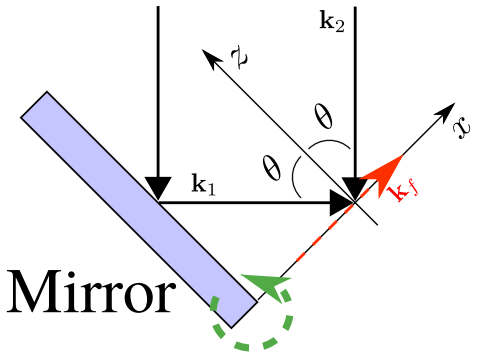

Figure A.2: Lloyd configuration to generate a interference pattern. The sample is placed at the right side of the diagram. The right angle between the sample and the mirror allows to rotate (arrow in green) and change the incident angle θ and hence the fringe period.

A.1.1.1 The Lloyd Interferometer

Typically two configurations of interferometers are used for nanopatterning, the Mach-Zhender configuration and the Lloyd configuration.[178, 180] The latter is the configuration used in this thesis. The Lloyd interferometer uses a mirror to reflect the incident wave towards the sample and create the interference pattern with these two beams. The mirror is perpendicular to the plane of interference and rotates in conjunction with the sample, see Fig. A.2. Using this configuration, the angle between the two incident waves can be changed as desired and consequently the fringe period, P_f.

The Lloyd configuration presents several advantages compared to Mach-Zhender configuration:

- It only requires one beam spatially filtered and expanded; this implies a compact set up.
- Easier modification of the period, which implies quick prototyping.
- Improved mechanical stability by design, as the mirror and sample are fixed together.

However, a typical disadvantage is the limit in area for nanopatterning the sample, as the area is limited by the size of the mirror, l_m. Obviously, the pattern will be

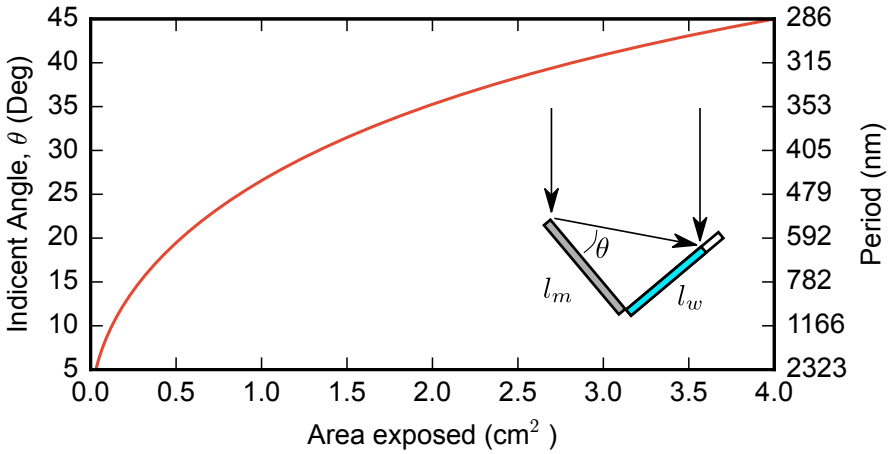

Figure A.3: The limit for the patterned area , for the interferometer system. The mirror size is , l_m = 2 cm. The area is calculated as $A = l_w^2$

generated only occurs in regions where there is a reflected beam. The area with both beams will be defined by a cutoff length, l_w:

$$l_w = l_m \tan(\theta), \tag{A.7}$$

and therefore the maximum area for exposition at each angle is $A(\theta) \propto l_w^2$. This limitation is more critical for large periods. The area usable is graphically illustrated in Fig. A.3. .

Another concern that should be addressed is the contrast in the pattern as we have already introduced. In general, the contrast is affected by not having two equally intense fields as we see in Eq. (A.6). Therefore, by using a mirror the reflected and incident field over the sample have different intensities, and consequently the contrast will decrease.[178] Still, for a metallic mirror this is usually not a problem, as the reflectivity is typically above the 90 % which translates to a contrast above the 99 %.[180] Yet, the contrast can be defined using the difference between the maximum and minimum in the pattern as in Eq. (A.6), or using the difference between minimum exposition and a threshold value. The latter definition is more adjusted to the experiment because above that threshold the photoresist will be exposed, and the minimum is not completely zero as we can expect some

background exposure apart from the effect of the intensity differences. Therefore, we can assume that at full width at half maximum of the intensity profile the photoresist is already exposed and the background can be approximated to zero when exposing short periods of time, leaving the dependence of the contrast to the different intensities between the beams. Using these assumptions the contrast is still above the 99%. But, to achieve square lattices using the Lloyd configuration we have to expose twice and this double exposure will also double the minimum intensity, whereas the maximum is already above that threshold. As we are increasing the minimum while the maximum is not modified, the contrast decreases. Still, because of the high reflectivity of a typical aluminum mirror, the contrast for a double exposure is 98%. But, incremental exposures will lower the contrast of the pattern due to this effect.

Finally, another limiting factor that can potentially lower the contrast is the coherence length of the laser. This limitation is dependant with the incident angle, as angles $\theta \ll \pi/4$ the beam should travel more distance before interfering. Therefore the contrast of the interference fringe is as a function of the optical path[180]:

$$C(l) = \exp\left(-(\pi/c)^2\sigma^2 l^2\right), \tag{A.8}$$

where l stands for the distance of the optical path difference and σ the half frequency bandwidth. The difference path between the incident wave and the reflected one is:

$$l = l_w/\sin(\theta)[1 + \cos(\pi - 2\theta)]. \tag{A.9}$$

Still, for the laser used with 160 MHz of linewidth (a coherence length around 1 m) and expanding the laser spot only 35 cm this limitation does not appear for short periods ($\theta < \pi/4$.), with contrasts above 98%. For lasers with bigger linewidths (1GHz), which implies shorter coherence length, could potentially limit the lithography resolution. [180]

To conclude, it is important to note that the incident waves upon the sample can create a stationary wave reflected perpendicular to the surface. This effect appears for any interferometric setup. The standing wave can be problematic for high reflectance samples and a photoresist antireflection layer should be used.[178] This limits the lithography on high reflecting substrates as metals, or high index

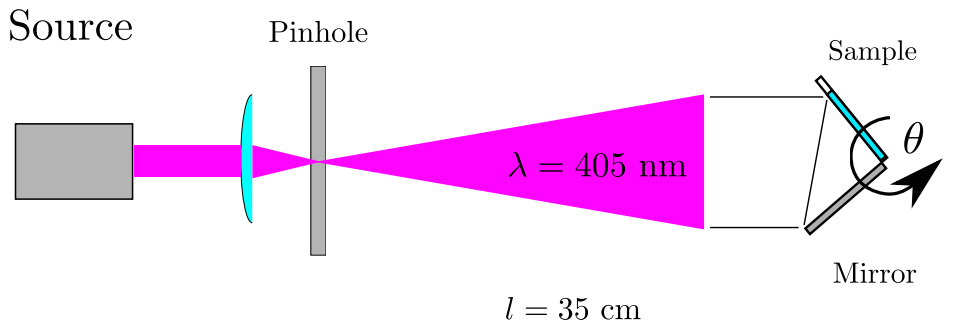

Figure A.4: Configuration of the Lloyd mirror used. The source is a laser diode of 12 mW with a wavelength of 405 nm (ONDAX CP-40X-PLR12). The lens plus the pinhole works as an spatial filter eliminating light intensity inhomogeneities at the sample. The focal length of the lens is 4 mm and the Pin hole has a 5 μm diameter. The distance between the pinhole and the center of rotation of the goniometer is l =35 cm

semiconductors. Typically, this problem is addressed by using an additional coating below the photoresist that absorbs the radiation transmitted through the photoresist.[178] However, the samples used in this thesis had low reflectance, and a photoresist antireflection layer was not needed, simplifying the fabrication process. In particular, not using a bottom photoresist helps to achieve a higher aspect ratio (height/width) for the nanostructures using the reactive ion etching, as the photoresist and the dielectric beneath have different etch rates.

A.1.2 Design of the experimental setup

The scheme of the experimental setup can be seen in Fig. A.4, where the laser diode represents the coherent source, and the Lloyd mirror is mounted on a goniometer, to control the incident angle and thus the period of the patterning.

The laser diode used has a centered wavelength of 405 nm, an output power of 12 mW, and its wavelength is stabilized with a volume holographic grating. The coherence length is longer than 1 m ($\Delta\nu$ =160 MHz) and the output beam is collimated. The polarization is TE with a polarization ratio of 100:1. The laser beam has an original radius, a_l, of $0.4 - 0.8$ cm, and it is expanded to 35 cm using an aspherical lens with a focal length, F, of 4 mm and a NA=0.6.

To eliminate the light intensity inhomogeneities at the sample we have used a

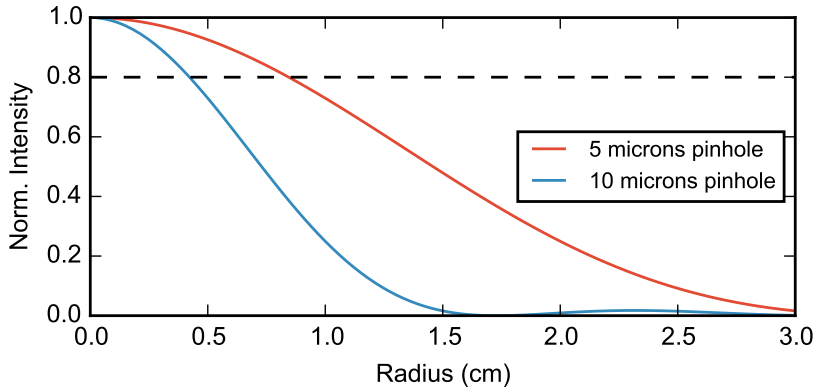

Figure A.5: Normalized intensity vs. the radius of a beam after passing a pin hole of 5 microns (red) and 10 microns (blue) at l=35 cm.

spatial filter by focusing the laser light on a small aperture. We have set the pinhole and lens specifications using the following expression:[180]

$$d_{\text{pin-hole}} = 2F\lambda/a_l, F = 4 \text{ mm} \Rightarrow d_{\text{pin-hole}} \approx 5\mu\text{m}. \tag{A.10}$$

Therefore, the spatial filter used has a pin-hole of 5 μm. Also, it is important to study the distribution of the spot after passing the spatial filter. In particular it will follow:[180]

$$I = 2\left(\frac{J_1(x)}{x}\right)^2;\ x = 2\frac{\pi}{\lambda}(D/2)(\rho/l), \tag{A.11}$$

where D stands for the pin-hole diameter, l for the distance between the pin hole and the perpendicular plane of the expanded wave, ρ for the radius of the beam at its plane, and $J_1(x)$ is the Bessel function . The intensity distribution for a 5 μm and a 10 μm pin-holes cases are graphically illustrated in Fig. A.5. This intensity profile will limit the area of exposure, in our case the useful area is approximately 1 cm^2.

The temperature of the laser will shift the wavelength used, and therefore the P_f of the pattern can be modified unintentionally. To avoid such wavelength instability we have used a thermal active mount. This active mount is mechanically attached to the spatial filter (lens and pinhole) by a 30 mm cage mount. In particular the lens is placed on Z-axis translation mount so that it can be focused on the pin hole,

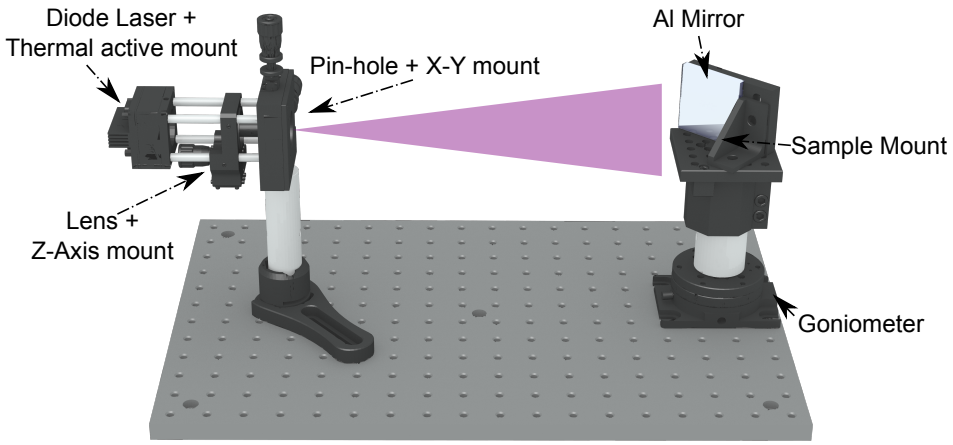

Figure A.6: Final experimental setup used in this thesis.

whereas, the pin hole itself is placed on a X-Y translation mount with micrometer screws to obtain fine adjustment. The complete optical setup can be seen in Fig. A.6.

In addition, a GaP photodiode is fixed at the sample mounting position to measure and calibrate the light exposure dose. A glass diffuser much larger than photodiode aperture is used to make the measurement independent of the angle of incidence. The samples are mounted for exposure on top of the diffuser. Using this photodiode we were able to adjust and reproduce the exposure doses between experiments. Once adjusted the laser the intensity over the sample was of 1.0 mW/m^2.

A.1.2.1 Examples of fabrication

First of all, we have to coat the sample with a photoresist to create the pattern. This photoresist is added by using spin coating, typically at 5000-6000 rpm. One important key is that the photoresists used must be photo-sensitive at 405 nm. In this thesis we have used a positive photoresist,[1] Shipley-S1805 with nominal thickness from 390-550 nm. Typically, the thickness of the photoresist will limit the smallest size we can achieve. As a rule of thumb, the thickness of the photoresist should be smaller than the smallest size of the pattern. Therefore, for patterns

[1] Negative photoresists such as MAN-1405 can be used, however the adherence problems difficult the fabrication, possibly due to lack of exposure at the interface with the substrate.

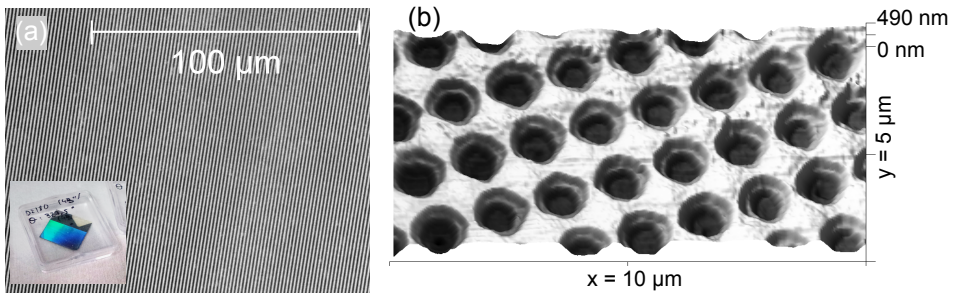

Figure A.7: (a) 1D lattice of Ni/Cr lines over optical glass with $\Lambda = 1330$ nm, inset photography of the sample. (b) Rectangular lattice of holes in S1805 over optical glass with $\Lambda = 1330$ nm.

with lattices below 400 nm we have to reduce the thickness. This can be done by diluting the photoresist with PGMEA, which allow us to have thicknesses below 200 nm.

The lattice period defined by this setup was between 1300 nm, just for testing and calibrating the setup, to 340 nm for the samples done as antireflective coatings. One important point to acknowledge is that patterns with periods smaller than 600 nm are difficult to inspect with optical microscopy. However, they can be checked using the iridescence at oblique angles. If the pattern is correctly exposed, the blue/purple tone appears in all the sample, highlighting the areas with weak diffraction efficiency, due to defects on the pattern.Another method is to put the sample again in the setup and look for the Moire patterns in the reflected beam. Yet, both checks are necessary conditions but not sufficient, as the pattern may not fully penetrate the whole photoresist layer. The definitive test is a SEM inspection of the samples.

Once the sample is exposed, we are able to transfer the nanopattern by metallization and lift-off for metallic samples, or by etching for dielectric/semiconductor samples. The former process was used to fabricate 1D metallic diffraction gratings, Fig. A.7(a), and the latter process was used for fabricating dielectric nanocones, Chapter 4, using reactive ion etching.

Also, it is interesting that despite using a positive photoresist, it is possible to obtain the *positive* or *negative* of a 2-D structure, namely nano-pillars and nano-holes respectively. This can be done by optimizing the exposure time.[135] To obtain

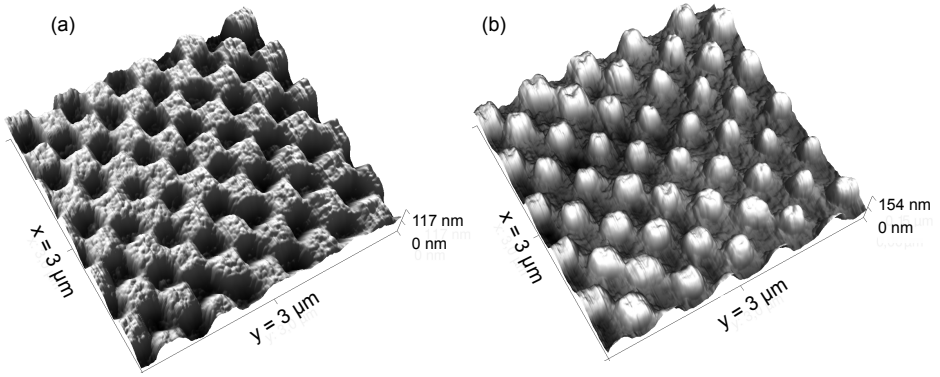

Figure A.8: (a) AFM image of a *chessy* 2D structure and (b) cylinder 2D pattern. In both cases the photoresist is positive, S1805 over Si_3N_4 and GaAs, we have only modified the exposure time (24 seconds and 26 seconds respectively).

pillars, the total exposure time is approximately twice the exposure time needed to obtain holes. In Fig. A.7(b) we demonstrate nanoholes fabricated using a positive photoresist. Also, controlling the exposure time we can control the filling factor of the photoresist, see Fig. A.8.

A.1.3 Possible improvements of this setup

The LIL setup here described had the purpose of fabricating the structures designed in Chapter 4 on small (1 cm^2) samples, and the set up has fulfilled its purpose. However, the experimental setup can be improved. One of the main problems was that the rotation was made by hand, because the steel strip mount fixes the sample position. This mount was very simple, but a ruled rotation mount allows to control the angle more finely. Indeed, the final fabricated samples has a slight tilt. These choices were justified by the low cost setup, and the limited time, but they can be easily replaced in the future, by incorporating a ruled rotation mount with a hole to incorporate the GaP photodiode.

On the other hand, the shutter of the sample was actuated by hand, hence an electro-mechanical system could improve the accuracy of the exposure time, which unleash the possibility for more complicate patterns combining this with a controlled rotation mount of the sample.[135, 174, 181]. The exposure time becomes a very critical parameter when exposing lattice parameters below the

specified resolution of the photoresist, as small increases (less than one second) of the exposure can easily lead to over-exposure. Beyond the resolution limit of the photoresist specifications there is narrowing of the parameter window for optimal contrast, thus very precise control of the exposure time becomes necessary.

Moreover, using a 355-375 nm diode laser would improve the resolution, as an smaller wavelength results in smaller patterns. Also, the contrast will improve as i-line photoresists are most sensitive at this wavelengths and consequently, the exposure time will decrease, reducing the effects of mechanical stability. A more powerful laser would also help to reduce the exposure time, and/or increase the patterned area by increasing the beam expansion.

A.2 Reflectivity Measurements

In this section the experimental setup used for measuring the reflectivity is detailed. This setup is graphically illustrated on Fig. A.9. The set up was adapted for reflectivity measurements from previous set ups that had been designed and built for other purposes by B. Alén, D. Fuster, E. San Román, and J. M. Ripalda. The basic idea is to use a monochromatic light source and two photodiodes to monitor the intensity. The light source is a halogen lamp (3000 K) dispersed by a 0.3 m focal length monochromator. The halogen lamp included a parabolic mirror and a lens to focus the duplicated image of the filament, and over the aperture of the monochromator. The mirror is used to obtain the radiation emitted on the back side. The optical intensity at the entrance of the monochromator is 1.7 W and the electric power consumption of the lamp is 100 W. The monochromator used is a Spex 270, and it is used in inverse configuration as monochromator, with the light source in the exit aperture. One of the photodiodes is placed after the monochromator to record the temporal fluctuations of the halogen lamp, it will be used as reference. The second photodiode is used to recover the intensity of the beam after the reflection on the surface of the sample. To increase the signal/noise ratio of the measurement we have used a 477 Hz chopper connected to a lock-in signal detector. This way, we are able to obtain a cleaner signal compared to just using the photodiodes. Ideally one would want to design such a set up in way that the solid angle and area of aperture of each optical element perfectly matches the

characteristics of the light beam, but in this case the source has a much larger etendue that the microscope objective used to probe the sample, and as a consequence most optical elements in the set up require to sacrifice part of the beam area and/or part of the illuminated solid angle. The entrance of the microscope objective that couples the monochromator to the optical fiber has a smaller area than the beam cross section, so part of the light that would fall outside of the lens entrance is redirected to the reference photodiode that is used to record the temporal fluctuations of the halogen lamp. The incident beam is coupled to the fiber using a 10x microscope objective (Mitutoyo) with large distance work. A 200 micron core size multi-mode optical fiber was used to allow for mechanical decoupling of the monochromator and the rest of the set up. Then the beam is expanded at the end of the fiber using an achromatic lens with a focal of 75 mm. Then, the collimated excitation beam was aligned with a Glan-Thompson polarizer at one the horizontal arms of a 45 degree beam splitter, and then focused to a 30 μm diameter spot using a Mitutoyo 20X NIR magnification objective lens (NA = 0.4) at the lower vertical arm of the beam-splitter. The beam-splitter is held by an XYZ stage with a manual micrometer screw to focus the incident beam on the sample, and stepper motors for lateral positioning. We chose optical elements optimized for visible and near infrared transmission. The sample sits below the objective lens, and the photodiode used for measuring the intensity after the reflection is above the beam splitter. The incident beam on the silicon photodiode is focused using an achromatic lens with F=60 mm. Both photodiodes have a big active area of 3.6x3.6 mm^2, so we can avoid alignment problems. One of the particularities of our setup is that we can measure the reflectivity for spots of 30μm radius, allowing us to measure locally the reflectance. Indeed, to modify the area of the spot we can change the microscope lens focusing on the sample, or the lens expanding the light from the laser fiber. Also, we have the possibility to quickly replace the reflectivity photodiode monitor with a digital camera without altering the optical alignment, allowing us to inspect the sample and locate the measurement spot before and after the measurement. In order to inspect the sample an auxiliary halogen lamp was used with an oblique angle to the sample. This auxiliary halogen lamp was shutdown during the measures. The signal from the photodiodes was acquired by a digital analog converter and a computer. In

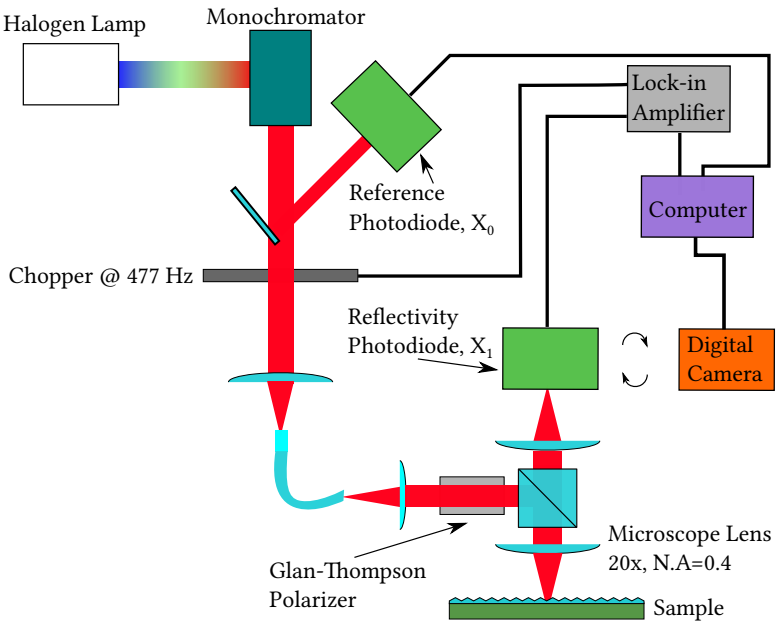

Figure A.9: Depiction of the experimental setup used for measuring the reflectivity.

particular, we have used a custom python code to control the monochromator, obtain the signal and plot the intensities. The spectral bounds of our experimental setup are limited by the wavelength response of the silicon photodiodes and the spectral distribution of our illumination source (440-1000 nm). However, in the measurements presented in Chapter 4 we are also limited by the absorption edge of the GaAs substrate (870 nm) as the transmitted light is partially reflected in the back of the GaAs sample.

Finally, the intensities obtained from the experimental setup must be calibrated using a reference sample. This way we can convert the electric signal from the photodiodes to a reflectivity. We have used a clean silicon substrate to calibrate the setup. Even though the lock-in detection is highly efficient in rejecting ambient light, there is some background signal from unwanted reflections in each of the optical elements of the set up. This background signal is measured using a 45 degrees mirror placed below the objective lens and is subtracted from the reflectivity

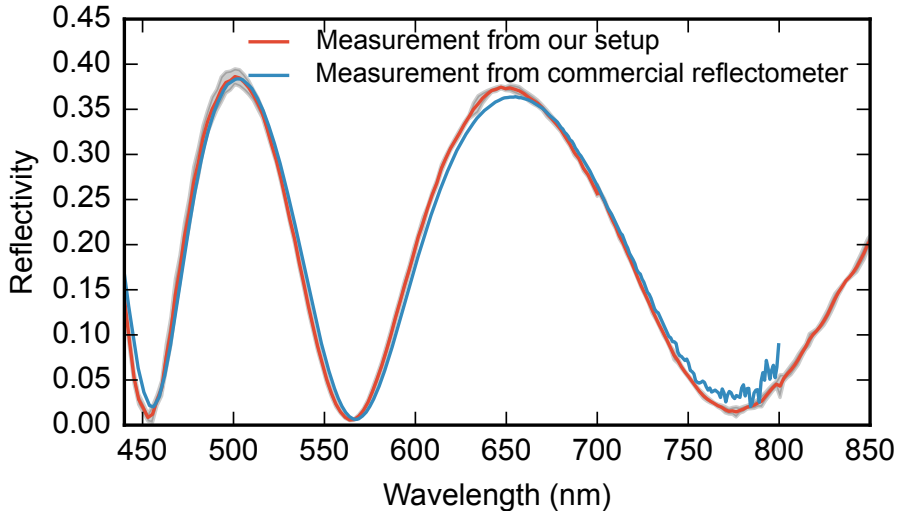

Figure A.10: Reflectivity measures of a Si_3N_4(495 nm)/Silicon sample by using our setup (red line) and a commercial reflectivity setup (blue line) (Sentech FTPAdv reflectometer).

photodiode measurement. Therefore the reflectivity of a sample m is:

$$\begin{aligned} R_m &= A\Big(X_{1,m}/X_{0,m} - X_{1,B}/X_{0,B}\Big), \\ A &= \frac{R_{\text{Si,theory}}}{(X_{1,\text{Si}}/X_{0,\text{Si}} - X_{1,B}/X_{0,B})}, \end{aligned} \tag{A.12}$$

where R_m is the reflectivity of the sample, A the correction factor of our setup, the subscript Si stands for the silicon substrate reference, X_0, i are the measures from the reference photodiode, X_1, i are the measures from the reflectivity photodiode, and subscript B stands for the background signal.

The experimental setup was validated measuring the reflectance of a GaAs substrate and silicon nitride films on top of a silicon substrate obtaining excellent agreement with measured spectra for such samples using a commercial reflectometer.

A.3 Additional Experimental Methods

In this section the additional experimental methods used in this thesis are described. These are standard micro-fabrication methods using standard

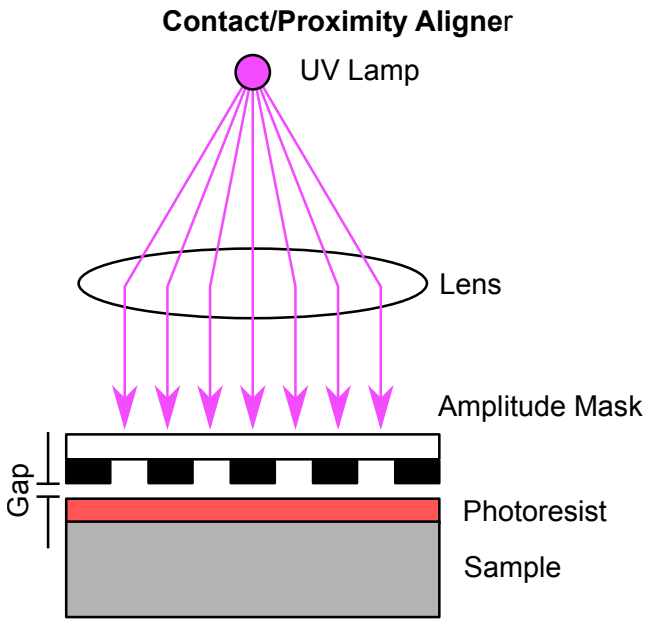

Figure A.11: Depiction of the typical setup used for UV lithography. The UV from the lamp is collimated by a lens and exposed the sample through the transparent zones of the mask. The Gap between sample and photoresist is usually the limiting factor for the resolution, smaller gaps implies higher resolution. However, the mask may suffer contamination from the sample with full contact.

commercial experimental setups. Here we present a summary of their fundamental operation and their limitations.

A.3.1 Contact/Proximity Mask Photolithography

The contact mask photolithography, or optical photolithography, is a micro-fabrication process. The pattern is transferred to the sample by exposing and developing a photoresist coating. To add the photoresist to the sample one technique used is spin coating. The sample is mounted on an rotating vacuum chuck and then the photoresist is added before/during the spinning of the sample. The rpm used are between 100-6000 rpm, depending on the photoresist type and desired thickness.

The mask defines the pattern transfered to the sample by using an UV lamp. For contact or proximity lithography the mask is in contact or in close proximity to

the sample. In a binary amplitude mask (as opposed for example to a phase shift mask) some parts are completely shaded and the UV exposes the sample through the transparent zones of the mask, see Figure A.11. The photoresist is sensitive to the light (250 to 450 nm approx.) and after the exposure the pattern is developed chemically (in either a solvent based or low pH aqueus solution developer), by immersion of the sample (alternatively spray or puddle development can be used). Two main types of photoresist exist: one positive where the photoresist exposed is removed by the developer, and negative photoresist where the non-exposed photoresist is removed with the developer. After this process, other techniques as lift-off for metals or wet/dry etchings are used to transfer the pattern from the photoresist to the sample. The resolution for this type of lithography, using amplitude masks, is physically limited by the diffraction of light from the mask, and from the proximity of the mask to the sample. The best resolution using vacuum contact exposure is typically around 500-700 nm using a conventional i-line lamp. However, more advanced setups can be used to improve this limit by using phase masks, instead of amplitude masks, deep ultra violet sources, ultra thin photoresist coatings, multiple exposures, surface plasmons masks, among other techniques. The highest possible theoretical resolution is $\lambda/20$.[182] Yet, high resolutions need full contact between the sample and the mask, which implies extremely planar and clean surfaces and vacuum contact.

In this thesis conventional photolithography was used for creating the control pattern in Chapter 4, as the photoresist used for the LIL process, S1805, can be exposed with the UV aligner. The sample was first exposed using the UV aligner and then with the LIL. Finally, the developer reveals both patterns in the sample.

A.3.2 Deposition techniques

A.3.2.1 Plasma enhanced vapour deposition

The plasma enhanced vapor deposition is a coating process based on plasma activation of gas precursors and their chemical reaction at the substrate surface (see Figure A.12). The plasma can be excited by RF or DC power supplies.

One of the advantages of this technique is that the deposition can be made at a low operation temperature (20-300 °C), making this technique compatible with

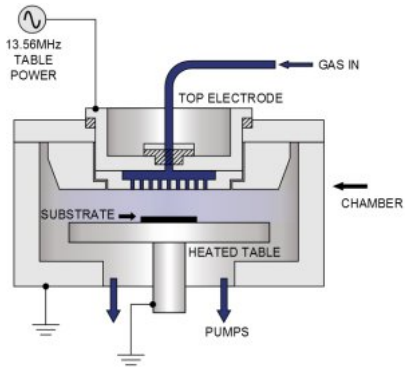

Figure A.12: Scheme of a PECVD, image from Oxford Instruments®.

electronic device fabrication. Also, it achieves good step coverage, and the deposited layers have good dielectric properties. In our lab the deposition rates are unstable, mostly due to pressure instabilities, and thus fine control of layer thickness is challenging. The most frequent applications are deposition of silicon oxide and nitride layers for passivation, insulation, and optical multilayers such as filters and anti reflection coatings. In this thesis the PECVD was used to deposit the Si_3N_4 layers of the fabricated sample in Chapter 4. The deposition conditions were SiH_4 1000 sccm and NH_3 28 sccm, at 200°C with rates of 10 nm/minute.

A.3.3 Reactive Ion Etching

The reactive ion etching (RIE) is a dry etching technology used in micro and nano fabrication. Compared to other type of etchings, like wet etching, the attack can be anisotropic or isotropic at will by modifying the conditions inside the gas chamber.

The etch is performed by a high power plasma which is chemically reactive and removes material from the sample. It consists of a vacuum chamber with a platter situated at the bottom, which is electrically insulated, see Figure A.13. The gas is introduced in the chamber under flow control. For instance, the pressures used are in the range of mTorr and the gas flow ranges from ten to a few thousand sccm.

In this thesis an inductively plasma (ICP) RIE was used, which means that the plasma is generated by a RF powered magnetic field. The oscillating electric/magnetic fields ionizes the molecules from the gas, and creates the plasma.

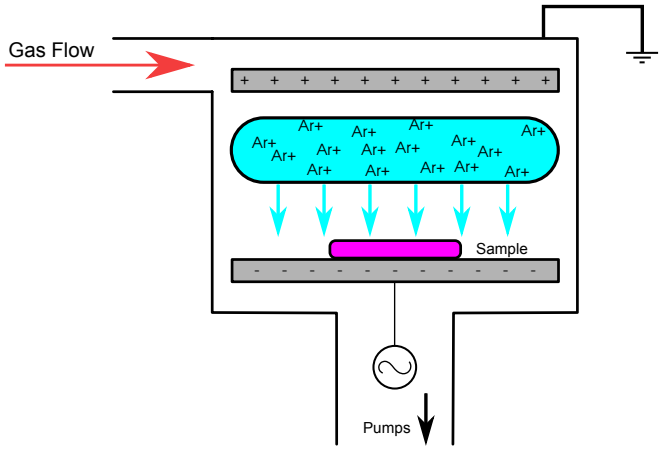

Figure A.13: Scheme of a RIE experimental setup.

The electrons from the ionized gas are accelerated to the walls of the chamber and to the platter. The chamber walls are connected to ground, so this charge disappears, whereas the platter is isolated and a negative charge gets accumulated. In fact, a negative DC voltage, typically around a hundred volts, appears in the platter. The positive ions from the plasma are electrically attracted by the DC field to the platter and attack the sample. This plasma removes material from the surface because of the kinetic energy from the ions and because of the chemical reactions between the plasma and the sample surface.

This technique is used to transfer the photoresist pattern to the sample. The photoresist mask is also attacked by the plasma, thus the etch rates for the substrate and the photoresist need to be experimentally determined to find the optimal experimental conditions. The objective is to achieve an attack ratio much slower for the mask than for the sample. The photoresist will also pyrolyze, making it difficult to remove after the etch. Because of this, when using a photoresist as mask is desirable to attack the sample using cooling pauses, for example by leaving the sample in vacuum for some time to cool it down, or by introducing nitrogen to cool it.

In this thesis, we have developed an anisotropic etching for Si_3N_4 using the S1805 photoresist as mask. The conditions are 200 W, 460 V, 10 mTorr plasma with a gas flow of 25 sccm of N_2 and 25 sccm of CHF_3. It was inspired from the work in Ref. [136]. However, to achieve a more directional etching the pressure and flow

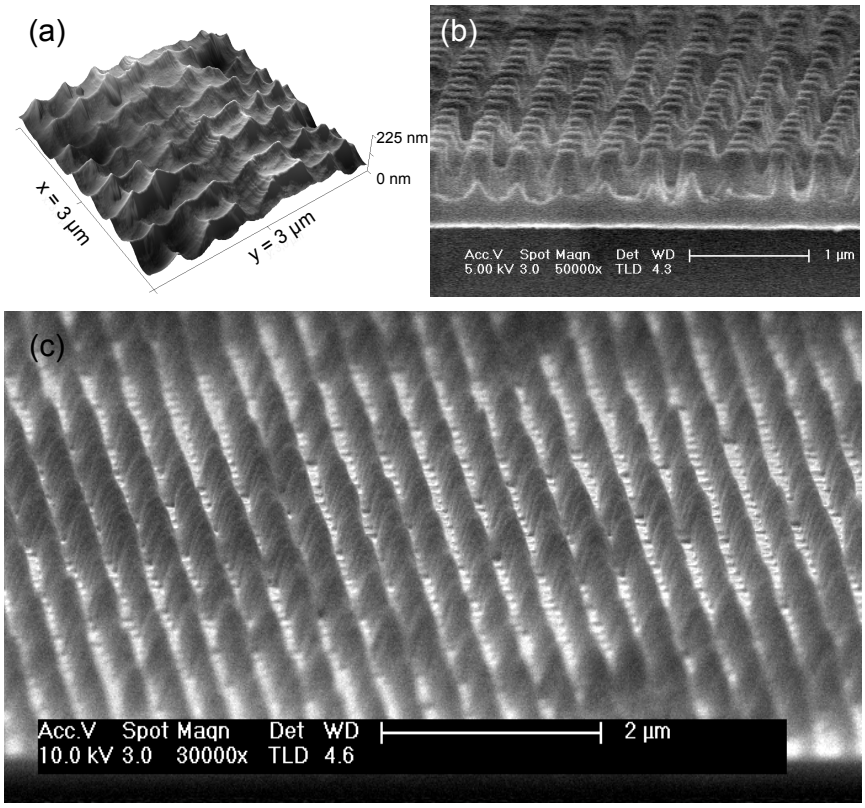

Figure A.14: (a) AFM image of the firsts attempts to fabricate the nanostructure using an etching without N_2 (a), which improves the selectivity. (b) An incomplete etch before using a pulsed attack. The photoresist may pyrolyze and the etching depth is not controlled. (c) Nanocones fabricated transferring the LIL nanopattern to Si_3N_4 using the optimized RIE etching (Sample characterized in Chapter 4).

were lower than in [136]. The ratio between CHF_3 and N_2 was also optimized for attacking more rapidly the nitride than the photoresist. The attack rates obtained were 55-60 nm/min for the Si_3N_4 and 15-20 nm/min for the photoresist. Another modification to the original recipe is that we have introduced a pulsed attack, in order to avoid excessive thermal damage to the photoresist. It followed a periodic sequence of 30 seconds of plasma, 2 minutes of vacuum, 1 minute of N_2 flux and 1 minute of vacuum. To complete the dry etching of the samples the loop was repeated 20 times, namely 10 minutes of plasma. The optimized etch allowed us to fabricate the nanocones of Chapter 4, see Fig. A.14(c).

Appendix B

Numerical Methods: RCWA

The rigorous coupled wave analysis (RCWA) is the method used in this thesis to model the photonic structures. This method is part of the so called computational electromagnetic methods (CEMs), that solve numerically the Maxwell equations. An introduction to the RCWA method is presented in this chapter with emphasis on its main practical advantages and limitations in comparison to other methods.

B.1 Introduction to RCWA

The earliest RCWA works focused on studying diffractions gratings for holograms.[183–185] The core principles of the RCWA were summarized and formulated by Moharam and Gaylord.[186, 187]. Afterwards, the original formulation was generalized to two-dimensionally periodic structures as the computational power was improved. [188, 189]

Typically the RCWA method is also called Fourier modal method (FMM) [190] or scattering matrix method (SMM) [81, 189, 191–193]. Besides, it is important to clarify that the scattering matrix formalism has been popular since the 1960s, [194, 195] and it is not exclusive of the RCWA or CEMs. To avoid any confusion, we will call RCWA the whole computational method, where the Maxwell equations are solved by the FMM and the device is fully constructed with scattering matrices.

The RCWA method is best suited for structures that can be approximated by a stack of layers. In each layer, the permittivity and permeability do not need to be homogeneous. The layers are defined by its thickness and a unit cell. They are finite in the normal direction but they are periodic (infinite) in the other plane. The permittivity distributions within the unit cell can be anything, but must be constant in the normal direction. Overall, the basic idea behind the RCWA is to solve numerically the in-plane directions, whereas the normal direction is solved analytically. The former is achieved by using the FMM, and the latter by using the SMM.

The first formulations suffered from very slow convergence with the number of Fourier series terms used when analyzing metallic gratings under the TM polarization.[196] Besides, a simple reformulation of the dielectric matrix could obtain improved convergence.[197, 198] The physical problem underneath is that there are different boundary conditions for the tangential and normal electric field components at an interface.[190, 199]. As a consequence, the permittivity in the reciprocal space needs of proper Fourier factorization rules.[200–202]

B.2 RCWA Formulation

CEMs algorithms solve numerically the well known Maxwell equations.[203]:

$$\begin{aligned} \nabla \cdot \mathbf{D} &= r, \\ \nabla \cdot \mathbf{B} &= 0, \\ \frac{\partial \mathbf{B}}{\partial t} &= -\nabla \times \mathbf{E}, \\ \frac{\partial \mathbf{E}}{\partial t} &= -\nabla \times \mathbf{H} - J_e. \end{aligned} \tag{B.1}$$

In the first place, we are going to express the fields in time-harmonic form, namely assuming $\exp(-i\omega t)$ time dependence. For simplicity, we are also going to assume that all the materials are linear and non-magnetic. In addtition, we will use Lorenz-Heaviside units, namely $\sqrt{\mu_0/\epsilon_0} = 1$, $c = 1$. Therefore, the time-harmonic Maxwell equations are reduced to:

$$\begin{aligned} \nabla \times \mathbf{H} &= -i\omega\epsilon\mathbf{E}, \\ \nabla \times \mathbf{E} &= i\omega\mathbf{H}. \end{aligned} \tag{B.2}$$

The structure is approximated by a laminar arrangement, with N layers, see Fig.Fig. B.1. To simplify the discussion, the coordinate system is oriented such as the laminar structure is periodic in the x-y plane, and with layers normal to z. In this section we focus only on layer l with thickness d. The layer l is placed between z_i and $z_i + d$ an the unit cell will be defined by $\epsilon_l(x, y)$. In the following section we will combine the solutions of the Maxwell equations of the different layers via a scattering matrix. For simplicity, let us assume l has a rectangular grating, with real space lattice $\mathbf{L}_r$ and its reciprocal lattice $\mathbf{L}_k$:

$$\begin{aligned} \mathbf{L}_r &= \begin{bmatrix} \mathbf{l}_{r,1} \\ \mathbf{l}_{r,2} \end{bmatrix}, \\ \mathbf{L}_k &= 2\pi[\mathbf{L}_r^{-1}]^T = 2\pi \begin{bmatrix} \mathbf{l}_{k,1} \\ \mathbf{l}_{k,2} \end{bmatrix}. \end{aligned} \tag{B.3}$$

Because of the layers periodicity in x and y, and the separability of the z axis due

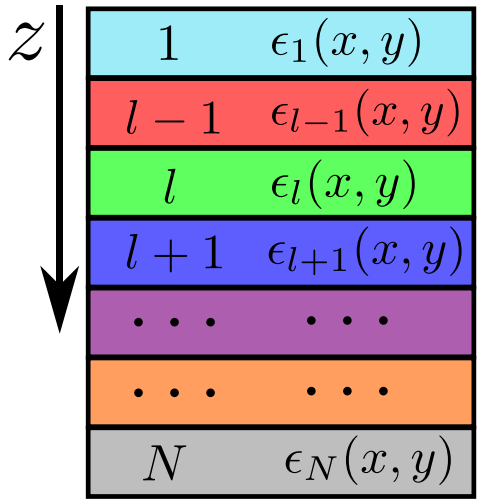

Figure B.1: The generalised structure solved in RCWA. It has N layers with a periodic permittivity distribution $\epsilon(x,y)$ with the same lattice parameter.

to the invariance in permittivity within the layer, the fields can be expressed as series in the reciprocal space:

$$\begin{aligned}
\mathbf{E}(\mathbf{r},z) &= \sum_{\mathbf{G}} \mathbf{E}_{\mathbf{G}}(z)\exp(i(\mathbf{k}+\mathbf{G})\cdot\mathbf{r}),\\
\mathbf{H}(\mathbf{r},z) &= \sum_{\mathbf{G}} \mathbf{H}_{\mathbf{G}}(z)\exp(i(\mathbf{k}+\mathbf{G})\cdot\mathbf{r}),\\
\mathbf{G}_{\mathbf{m},\mathbf{n}} &= \frac{2\pi m}{|\mathbf{l}_{1,r}|}\mathbf{l}_{1,k} + \frac{2\pi n}{|\mathbf{l}_{2,r}|}\mathbf{l}_{2,k};\\
m,n &= 0,\pm1,\pm2,\ldots,\infty.
\end{aligned} \tag{B.4}$$

where $\mathbf{r} = \mathbf{x} + \mathbf{y}$, $\mathbf{G}$ is a vector of the reciprocal lattice and $\mathbf{k}$ is the in-plane component of the wave vector set by the excitation. Equation (B.4) represents the expansion used in RCWA. What is more, in Eq. (B.4) appears the fundamental numeric approximation, as we cannot use infinite $\mathbf{G}$ vectors. As a consequence, we have to truncate the series and the upper vector $\mathbf{G}_{\max}$ must be set by us. Clearly, the convergence of the simulation will depend on its value. For 1D unit cells the truncation is straight forward, but not for 2D unit cells. In fact, the truncation in the reciprocal space in 2D can be set by a circular rule $|m^2+n^2| \leq R^2$ being R the upper limit radius, or a rectangular rule $|m|^2 + |n|^2 \leq L^2$ being L the upper limit

side of a square. The choice would depend on the geometry of the unit cell.

Assuming that $\mathbf{G}_{\max}$ is fixed, we define $\mathbf{e}(z) \equiv [\mathbf{E}_{\mathbf{G}_1}, \mathbf{E}_{\mathbf{G}_2}, \cdots]$, and $\mathbf{h}(z) \equiv [\mathbf{H}_{\mathbf{G}_1}, \mathbf{H}_{\mathbf{G}_2}, \cdots]$. One important concern is that the ordering of the vectors in the reciprocal space $\mathbf{G}$ must be consistent throughout the algorithm.

Next, we have to couple the fields, $\mathbf{e}(z)$ and $\mathbf{h}(z)$, to the periodic structure we want to simulate. The permittivity is in general a tensor but we will assume isotropic materials, namely it will be an scalar. Therefore, the permittivity in the real space $\epsilon(\mathbf{r})$ is translated in the reciprocal space as:

$$\begin{aligned} \epsilon(\mathbf{r}) &= \sum_{\mathbf{G}} \epsilon_{\mathbf{G}} \exp(i(\mathbf{k}+\mathbf{G})\cdot\mathbf{r}), \\ \epsilon_{\mathbf{G}} &= \frac{1}{|L_r|}\int_{\text{cell}} \epsilon(\mathbf{r}) \exp(-i\mathbf{G}\cdot\mathbf{r})\mathrm{d}\mathbf{r}, \end{aligned} \tag{B.5}$$

where the integral is over one unit cell of the lattice. This integral can be done by using the closed form of the Fourier transform or using the fast Fourier transform (FFT) of a spatial sampling image of $\epsilon(\mathbf{r})$. Now, we can form the matrix[1] that will be used to couple $\mathbf{e}(z)$ and $\mathbf{h}(z)$ to the unit cell:

$$\widehat{\epsilon}_{mn} = \epsilon_{(\mathbf{G}_m - \mathbf{G}_n)}, \tag{B.6}$$

where it is used the superscript $\widehat{(\,)}$ to refer operators acting in $\mathbf{G}$ space. Thus, we introduce $\widehat{\epsilon}$ in Eq. (B.2):

$$\begin{aligned} i\widehat{k}_y h_z(z) - h_y'(z) &= -i\omega\widehat{\epsilon}e_x(z), \\ h_x'(z) - i\widehat{k}_x h_z(z) &= -i\omega\widehat{\epsilon}e_y(z), \\ i\widehat{k}_x h_y(z) - i\widehat{k}_y h_x(z) &= -i\omega\widehat{\epsilon}e_z(z); \\ i\widehat{k}_y e_z(z) - e_y'(z) &= i\omega h_x(z), \\ e_x'(z) - i\widehat{k}_x e_z(z) &= i\omega h_y(z), \\ i\widehat{k}_x e_y(z) - i\widehat{k}_x e_x(z) &= i\omega h_z(z), \end{aligned} \tag{B.7}$$

[1] Formally, the block Toeplitz matrix.

where $\widehat{k_u} = \mathrm{diag}(k_u + G_{1u}, k_u + G_{2u}, \cdots)$ $u = x, y$ represents the field wave-number in the $\mathbf{G}$ space. Then, we can eliminate the z components $(h_z(z), e_z(z))$. As result, we reformulate Eq. (B.7) to obtain:

$$(\omega^2 \mathbf{I} - \kappa) \begin{bmatrix} h_x(z) \\ h_y(z) \end{bmatrix} = -i\omega \begin{bmatrix} -e_y'(z) \\ e_x'(z) \end{bmatrix}, \tag{B.8a}$$

$$(\omega^2 \mathcal{E} - \mathcal{K}) \begin{bmatrix} -e_y(z) \\ e_x(z) \end{bmatrix} = -i\omega \begin{bmatrix} h_x'(z) \\ h_y'(z) \end{bmatrix}, \tag{B.8b}$$

where,

$$\mathcal{E} = \begin{bmatrix} \hat{\epsilon} & 0 \\ 0 & \hat{\epsilon} \end{bmatrix}, \tag{B.9a}$$

$$\kappa \equiv \begin{bmatrix} \hat{k}_y & \hat{k}_y \\ -\hat{k}_x & -\hat{k}_x \end{bmatrix} \mathcal{E}^{-1} \begin{bmatrix} \hat{k}_y & 0 \\ 0 & -\hat{k}_x \end{bmatrix}, \tag{B.9b}$$

$$\mathcal{K} \equiv \begin{bmatrix} \hat{k}_x \hat{k}_x & \hat{k}_x \hat{k}_y \\ \hat{k}_y \hat{k}_x & \hat{k}_y \hat{k}_y \end{bmatrix}. \tag{B.9c}$$

Once we have set Eq. (B.8), which are just the Maxwell equations in matrix form, we have to express the fields as a superposition of eigenmodes. Consequently, we have to set the z dependence proportional to $\exp(iqz)$, being q some complex number. Also, we will impose $\boldsymbol{\nabla} \cdot \mathbf{H} = 0$ in the expansion. Following from the expression Eq. (B.4) the magnetic field can be expressed as:

$$\begin{aligned} \mathbf{H}(\mathbf{r}, z) = \sum_{\mathrm{G}} \Big[& \Phi_{\mathrm{G},x}\, \mathbf{x} + \Phi_{\mathrm{G},y}\, \mathbf{y} \\ & - \frac{(k_x + G_x)\Phi_{\mathrm{G},x} + (k_y + G_y)\Phi_{\mathrm{G},y}}{q} \mathbf{z} \Big] \exp(i(\mathbf{k} + \mathbf{G}) \cdot \mathbf{r} + iqz) \end{aligned} \tag{B.10}$$

where $\mathbf{x}$, $\mathbf{y}$, and $\mathbf{z}$ are the Cartesian unit vectors and $\Phi_{\mathrm{G},x}$ and $\Phi_{\mathrm{G},y}$ are the expansion coefficients. This form satisfies $\boldsymbol{\nabla} \cdot \mathbf{H} = 0$ as we have expressed the z axis coefficients as function of x and y. We can do analogously for the electric

field, using equations (B.4) and (B.10). Also, we can group this coefficients as vectors: $\Phi_x = [\Phi_{G_1,x}, \Phi_{G_2,x}, \cdots]$ and similarly for Φ_y. Next, we can substitute Eq. (B.10) in Eq. (B.8) to drop the z dependence and combine both equations eliminating the fields:

$$\begin{aligned} (\mathcal{E}(\omega^2 - \kappa) - \mathcal{K})\Phi &= \Phi \mathbf{q}^2, \\ \Phi &= [\Phi_{x,n}, \Phi_{y,n}]^\intercal, \end{aligned} \tag{B.11}$$

where $\mathbf{q}^2$ is a diagonal matrix with the eigenvalues q_n^2. Obviously, this equation can be solved as an eigenvalue problem. Generally, finding the eigenmodes of each layer will be the computational time bottleneck. Now, we are able to recover the in-plane fields, i.e. the transverse components e_t and h_t of a layer l_i between z_i and $z_i + d_i$:

$$\begin{aligned} \begin{bmatrix} e_t(z) \\ h_t(z) \end{bmatrix} &= \begin{bmatrix} \Theta & -\Theta \\ \Phi & \Phi \end{bmatrix} \times \begin{bmatrix} f(z) & 0 \\ 0 & f(d-z) \end{bmatrix} \begin{bmatrix} a \\ b \end{bmatrix}, \\ \Theta &\equiv (\omega^2 \mathbf{I} - \kappa)\Phi \mathbf{q}^{-1}, \end{aligned} \tag{B.12}$$

where a and b are the coefficient of the forward (towards z positive) and backward propagating waves at $z = z_i$ and at $z = z_i + d$ respectively, and $f(z)$ is a diagonal matrix operator with entries $f(z)_{nn} = \exp(iq_n z)$. Finally the z components of the fields are recovered by substituting Eq. (B.12) in Eq. (B.7).

In summary, we have solved the time-harmonic Maxwell equations in matrix form, Eq. (B.8), by using a Fourier basis, Eq. (B.10) to finally obtain an eigenvalue problem, Eq. (B.11). In order to obtain the fields we substitute in Eq. (B.7). Yet, we have solved the fields for one layer only. It follows that we have to use some matrix formalism to solve the whole structure, in our case the scattering matrix.

B.2.1 The Scattering Matrix

Even though we will use the scattering matrix to couple the different layers of the device, it is important to clarify that the scattering matrix is not the only matrix that can be used to solve the structure. Chiefly, there are two other types of matrices

typically used. Such as the transfer matrix [204–206], and the impedance matrix [207]. However, the transfer matrix is numerically unstable, whereas the impedance matrix is less used by the CEM community, leaving the scattering matrix as the *state-of-the-art*.[208]

For the sake of simplicity, lets assume the n layer is between two layers, 0 and M, see Fig. B.2.

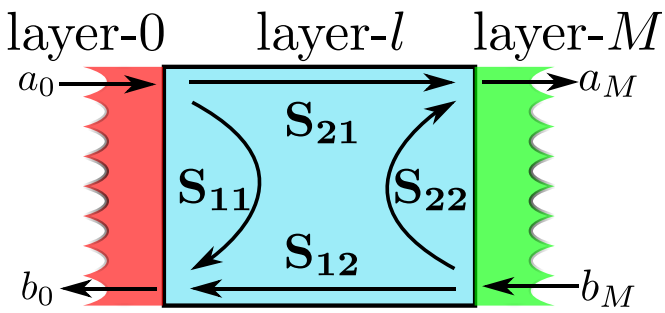

Figure B.2: The amplitudes coefficients of the scattering matrix related to its coefficients for a l layer between layers 0 and M.

In addition, we assume these latter layers have no thickness, as they represent the front and back dielectric media. The scattering matrix of the l layer is defined by linking the forward in z channels $\mathbf{a} = [a_0, a_M]$ to the backward channels $\mathbf{b} = [b_0, b_M]$:

$$\begin{bmatrix} b_0 \\ a_M \end{bmatrix} = \begin{bmatrix} \mathrm{S}_{11} & \mathrm{S}_{12} \\ \mathrm{S}_{21} & \mathrm{S}_{22} \end{bmatrix} \begin{bmatrix} a_0 \\ b_M \end{bmatrix}, \tag{B.13}$$

The calculation of the S-matrix comprises a series of steps. First and foremost, we have to to obtain the eigenvalues of the l layer, Eq. (B.11). Then, generate the block matrices, and proceed to couple this layer by imposing the transmission boundary

conditions:

$$\begin{bmatrix} \Theta_0 & -\Theta_0 \\ \Phi_0 & \Phi_0 \end{bmatrix} \begin{bmatrix} a_0 \\ b_0 \end{bmatrix} = \begin{bmatrix} \Theta_l & -\Theta_l \\ \Phi_l & \Phi_l \end{bmatrix} \begin{bmatrix} \mathbf{I} & 0 \\ 0 & f_l(d) \end{bmatrix} \begin{bmatrix} a_l \\ b_l \end{bmatrix},$$
$$\begin{bmatrix} \Theta_l & -\Theta_l \\ \Phi_l & \Phi_l \end{bmatrix} \begin{bmatrix} f_l(d) & 0 \\ 0 & \mathbf{I} \end{bmatrix} \begin{bmatrix} a_l \\ b_l \end{bmatrix} = \begin{bmatrix} \Theta_M & -\Theta_M \\ \Phi_M & \Phi_M \end{bmatrix} \begin{bmatrix} a_M \\ b_M \end{bmatrix} \tag{B.14}$$

We can use Eq. (B.14) to establish the blocks of the scattering matrix, Eq. (B.13) (S_{11}, S_{12}, S_{21} and S_{22}). This process can be easily generalized for a multi-layered device to generate the global scattering matrix, S. Namely, we construct S by *multiplying* each scattering matrix of N layers using the Redheffer's star product:

$$\mathrm{S} = \mathrm{S}^{(\mathrm{ref})} \otimes \mathrm{S}^{(1)} \otimes \mathrm{S}^{(2)} \ldots \otimes \mathrm{S}^{(N)} \otimes \mathrm{S}^{(\mathrm{trm})}, \tag{B.15}$$

where (ref) and (trm) stands for reflected and transmitted mediums, for the simple case of one layer ref=0, N=1, and trm=M.[2]

In addition, one computational trick that can be used is to incorporate zero thickness layers between each layers.[208, 209] If the l layer fulfill the same boundary conditions at the front and back interfaces, i.e. the front and back materials are the same and it is composed of materials that themselves obey reciprocity, then the scattering matrix of the l layer is symmetric: $S_{12} = S_{21}$, and $S_{11} = S_{22}$. The use of zero thickness layers complicates the calculus, but the memory footprint of the algorithm is reduced. What is more, by using these layers the S matrix of each *real* layer can be arbitrarily interchanged and therefore *r*ecycled. Also, if the transmitted and incident media are the same as the zero thickness layers there is no need to couple the device to external regions.

Once we generate the global S-matrix, we can obtain the reflectivity and transmission spectra. By analyzing Equation (B.13) it is clear which blocks of the scattering matrix can be associated to real physical meanings. If light is coming

[2]The scattering matrix of the incident mediums can be found using Eq. (B.13). For example, if the incident medium is air/vacuum: $S^{ref} = \begin{bmatrix} 0 & I \\ I & 0 \end{bmatrix}$.

from the left, $b_M = 0$, $\mathbf{S_{11}} \equiv$ the *reflection*, and $\mathbf{S_{12}} \equiv$ the *transmission*, of the l layer, see Fig. B.2.[3]

To obtain the reflectivity by an incident plane wave we have to translate the amplitude vectors $(\mathbf{a}, \mathbf{b})$ into *experimental* waves with an angle and polarization. This translation is done by using Eq. (B.12) and a_0. In fact, as we are exciting only the propagation on $a_0(G_1)$, the zero order, because it will be the only non-zero component. Assuming the layers are 0 and M the transverse components are:

$$\begin{aligned} e_{t,\text{inc}} &= \Theta_0 a_0, \\ e_{t,\text{ref}} &= -\Theta_0 b_0, \\ e_{t,\text{trm}} &= \Theta_N a_M. \end{aligned} \tag{B.16}$$

And using Eq. (B.13):

$$\begin{aligned} b_0 &= \mathbf{S_{11}} a_0, \\ b_M &= \mathbf{S_{21}} a_0. \end{aligned} \tag{B.17}$$

Combining Eq. (B.16) and Eq. (B.17) we could obtain the transverse component of the output fields:

$$\begin{aligned} r_t &= e_{t,\text{ref}} = -\Theta_0 \mathbf{S_{11}} \Theta_0^{-1} a_0, \\ t_t &= e_{t,\text{trm}} = \Theta_0 \mathbf{S_{21}} \Theta_0^{-1} a_0. \end{aligned} \tag{B.18}$$

where r_t and t_t correspond to the transverse reflected and transmitted fields. The longitudinal part of this fields, r_z and t_z, are obtained by the divergence equation of the electric field, and substituting $\widehat{k}_{s,z};\ s = \text{ref,trm}$. Hence, the reflected and transmitted fields vectors are: $\mathbf{r} = (r_t, r_z)$ and $\mathbf{t} = (t_t, t_z)$ respectively. Then, assuming a unit amplitude source, the reflection and transmission are:

$$\begin{aligned} R &= \sum_{\mathbf{G=0}}^{\mathbf{G_{max}}} \mathbf{R} = \sum_{\mathbf{G=0}}^{\mathbf{G_{max}}} \left(\text{Re}\left[\frac{-\widehat{k}_{z,\text{ref}}}{\widehat{k}_{z,\text{inc}}} \right] |\mathbf{r}|^2 \right), \\ T &= \sum_{\mathbf{G=0}}^{\mathbf{G_{max}}} \mathbf{T} = \sum_{\mathbf{G=0}}^{\mathbf{G_{max}}} \left(\text{Re}\left[\frac{\widehat{k}_{z,\text{trm}}}{\widehat{k}_{z,\text{inc}}} \right] |\mathbf{t}|^2 \right). \end{aligned} \tag{B.19}$$

[3] In this section we have used the same formulation as in [208]. Other conventions like the ones used in [189, 199] interchange the equivalences of the scattering matrix blocks with the reflectivity and transmittance. Both conventions are physically equivalent. However, the former present some advantages as the S-matrix of each layer is symmetric if the layer is surrounded by two identical layers, and, as R. Rumpf noted in [208], it is the *standard* convention used in other research areas, previously to CEM implementations.

To obtain the total reflection and transmission, R and T, we have to add all the reflection and transmission coefficients of each $\mathbf{G}_i$. Besides, if the structure reflects or transmits at high orders, the simulation will only converge for a large $\mathbf{G}_{\max}$, hence increasing the computation time. In same cases it is interesting to obtain the diffraction efficiencies for each diffraction order, $\mathbf{G}_i$, by using $\mathbf{R}$ and $\mathbf{T}$.

In summary, the S-matrix can be used to obtain the fields, the reflection and transmission of a photonic structure. Another feature we have not mentioned is that it is possible to find the modes of the whole structure by finding the poles of the determinant of the global S-matrix.[81]

B.2.2 FMM formulations

In the preceding sections we have described the RCWA algorithm without hesitation on how to construct the $\mathcal{E}$ matrix, which physically represents the permittivity in the Fourier space. Therefore, we are after a matrix that relate the displacement, d_t, and electric field, e_t:

$$\begin{aligned} \mathbf{d}_t &= \mathcal{E}\mathbf{e}_t, \\ \begin{bmatrix} d_x \\ d_y \end{bmatrix} &= \begin{bmatrix} \widehat{\epsilon} & \\ & \widehat{\epsilon} \end{bmatrix} \begin{bmatrix} e_x \\ e_y \end{bmatrix} \end{aligned} \tag{B.20}$$

where ϵ is generated by Eq. (B.5) and the $\widehat{\ }$ corresponds to the spatial Fourier transform.

However, if the electric field has a significant normal component to the in-plane material interface, the convergence is very slow in the number of $\mathbf{G}$. For example this happens for the TM mode in metallic 1D gratings.

Fourier factorization rules were introduced in Ref. [199] and they dictate that the displacement and electric field components are built different for the normal and tangential directions of the electric field to the dielectric permittivity within the unit cell:

$$\begin{aligned} d_{\parallel} &= \widehat{\epsilon}\, e_{\parallel}, \\ d_{\perp} &= \widehat{\eta}\, d_{\perp}, \end{aligned} \tag{B.21}$$

where $\eta = \epsilon^{-1}$. In other words, the inverse of the permittivity for the normal components to the interface is done in the real space, namely before the Fourier transform. When the structure is 1D and the x and y directions are separable, it is straight forward to apply this rule:

$$e_y = \widehat{\epsilon^{-1}} d_y = \widehat{\eta} d_y. \tag{B.22}$$

However, when the structure is 2D, x-y directions are no longer separable. Therefore, we have to generate a coordinate system (a vector field) where the parallel and perpendicular components are independent, a dubbed fast Fourier factorization (FFF) [200]:

$$\mathcal{E} = \widehat{\mathcal{T}} \begin{bmatrix} \widehat{\epsilon} & \\ & \widehat{\eta}^{-1} \end{bmatrix} \widehat{\mathcal{T}^{-1}} \tag{B.23}$$

where $\mathcal{T}$ is the change of basis matrix to the field vector $\mathbf{t}$ which is periodic (like the unit cell) and with separable tangent and normal components to all material interfaces inside the unit cell. Besides, in the literature there are different approaches to find this change of basis. [101, 200, 210, 211] Basically, they differ on when to apply the Fourier transform to the change of basis, and how to find the $\mathcal{T}$ matrix. The different formulations of FFF are reviwed and implemented in [101].

B.3 An outlook on RCWA and a comparison with other methods

We have detailed the RCWA method in the previous sections, as it is the method used in this thesis. Some of the most notable alternatives to RCWA are finite difference in the time and frequency domain (FDTD [212] and FDFD [213]) , the finite elements method (FEM) [214], and the C-method [215, 216]. All of them can be used to solve the the electromagnetic fields for the photonic nanostructures proposed in this thesis. The structures presented in this thesis are 3-D, dielectric, periodic and laminar; the RCWA is thus particularly suited because of its Fourier basis representation. One characteristic constrain of the RCWA method is that each layer only has structure in the lateral directions, and such structure must be periodic. The nano-cones arrays proposed in Chapter 3, must then be sliced in a

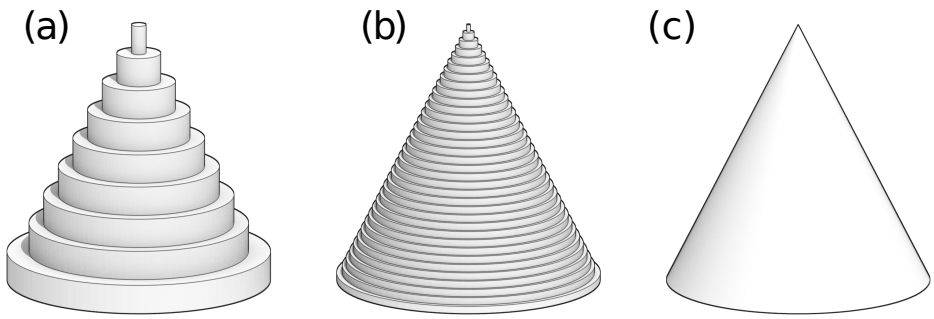

Figure B.3: Approximation used in the RCWA method to generate a cone. The cone is sliced into layers, and made up with concentric cylinders. Using few layers like in (a) is desirable for optimizations to reduce the computation time, but an accurate result needs more layers like in (b) to make the simulation converge to the ideal cone (c).

multilayer of cylinders of increasing radii, see Fig. B.3, and it can be calculated accurately by increasing the number of layers, but the drawback is the computation time increases. Still, the RCWA is a fast and direct method to obtain the reflectivity and transmission, being both magnitudes fundamental for the development of this thesis. In contrast, other methods such as FEM or FDTD need further post-processing for these two magnitudes. Besides, it is important to compare this method to other CEMs and clarify its practical advantages and disadvantages. I will center on comparing RCWA to FDTD, FEM and the C-method as they are the more typical CEMs.

FDTD is a very popular and flexible method. It can be used for metallic and dielectric gratings, and there are quite popular commercial and open source implementations.[217, 218] However, one simple advantage of RCWA would be that materials permittivities can be introduced directly as RCWA is solved in the frequency domain. In contrast, time domain algorithms, as FDTD, typically need a fitting to dispersion models to simulate real materials. Another positive consequence of operating in the frequency domain is that it is very easy to parallelize a spectrum, as each frequency can be calculated in a separated CPU process. In fact, RCWA typically needs less computational resources than FDTD. A 3D calculus in RCWA is generally faster than in FDTD because RCWA solves numerically only two space dimensions, whereas FDTD solves three space dimensions plus the propagation time. Also, if the unit cell is correctly described

with few reciprocal vectors, the sampling needed is lower than the sampling used in the real space as in FDTD. Therefore, the unit cell data can be numerically *compressed*, as in computer science, by choosing a few reciprocal vectors. This later advantage disappears if a lot of reciprocal vectors are excited in the strucutre, a typical situation found in the case of big unit cells.

FEM is another very flexible and popular method, in particular for plasmonics. It is also typically solved in the frequency domain like RCWA. However, in comparison, RCWA does not require to define an explicit mesh, allowing a quick modification of the structure. This is critical when the objective is to make a global optimization of the initial structure. Some workis in the literature combine RCWA with FEM to reduce the staircasing problem and increase the convergence with metals.[219, 220]

Another method formally close to RCWA (frequency domain and EM fields expressed in diffraction orders) that should be treated separately is the C-method. The C-method uses a coordinate transformation and it does not require any slicing, or meshing. Also, the computation time is similar to the RCWA for a few layers, or even quicker.[221] Its main advantage in contrast to RCWA is that complex structures in z can be simulated without an stair-case approximation. However, the dielectric interface has to be described parametrically, namely as a function. As a result, the problematic geometric structures are sort of opposite compared to RCWA, as steep profiles need to increase the sampling. This problem can be overcome by using an additional coordinate transformation, namely an adaptive resolution method.[222] Still, the strengths of both methods can be combined if they are introduced into the same S-matrix.[223]

Nonetheless, RCWA presents some unavoidable disadvantages apart from the staircasing already mentioned. Relaying on the Fourier transform of the dielectric structure implies that it will require a high number of reciprocal vectors for high permittivity contrast structures, as a metal-dielectric structure, and it can be adversely affected by ill-conditioned matrices and the Gibbs phenomenon.[199] Another consequence of using the Fourier transform is that each layer must have the same periodicity, unless some kind of perfect matching layer (PML) is used to isolate each nanostructure.[224, 225] Then again, the normal components of the fields in metal grids are difficult to handle even with proper Fourier factorization

rules, which generally increase the computation time. Using RCWA for this type of structures may require a huge sampling in the reciprocal space and the simulation convergence is not assured [101]. As result, metals are generally simulated using FEM or FDTD. Moreover, from a practical view, the energy conversion is granted even for non accurate results. This implies that every RCWA calculus will have to be tested by increasing the number of reciprocal vectors until the calculus converges.

Lastly, from a more practical point of view, we chose to use RCWA as it is a well known robust algorithm and it is quite easy to find several open source codes with an active community.[101, 208, 226] In fact, in this thesis we have mainly used the implementation by V. Liu,[101], because we were able to combine this implementation with other numerical packages,[109, 227, 228] within the same code, overall simplifying the process.

Above all, the flexibility and speed of this method, let us draft, optimize and analyze several structures before finding the best ones for our applications.

Bibliography

1. *World Population Prospects* Key findings & advance tables (Department of Economic and Social Affairs, United Nations, New York, USA, 2015).
2. T. Team. Solar Star Project, Japan DG Demand Drive SunPower's Q3. *Forbes* (2016).
3. SunPower. *Solar Star Projects* https://us.sunpower.com/utility-scale-solar-power-plants/solar-energy-projects/solar-star-projects/. Text. 2014.
4. *Large-Scale Photovoltaic Power Plants - Top 50* http://www.pvresources.com/en/top50pv.php.
5. *SolarGIS Poster Maps: Solar Radiation Data (GHI, DNI, PV)* http://solargis.info/doc/postermaps.
6. C. Fritts. On a New Form of Selenium Photocell. *American J. of Science* **26,** 465 (1883).
7. D. M. Chapin, C. S. Fuller & G. L. Pearson. A New Silicon p-n Junction Photocell for Converting Solar Radiation into Electrical Power. *Journal of Applied Physics* **25,** 676–677 (1954).
8. A. Luque & S. Hegedus. in *Handbook of photovoltaic science and engineering* (eds A. Luque & S. Hegedus) 1–41 (Wiley, Hoboken, NJ, 2003).
9. M. A. Green, K. Emery, Y. Hishikawa, W. Warta & E. D. Dunlop. Solar cell efficiency tables (version 43). *Progress in Photovoltaics: Research and Applications* **22,** 1–9 (2014).
10. K. J. Arrow. The Economic Implications of Learning by Doing. *The Review of Economic Studies* **29,** 155 (1962).
11. R. M. Swanson. A vision for crystalline silicon photovoltaics. *Progress in Photovoltaics: Research and Applications* **14,** 443–453 (2006).

12. J. D. Farmer & F. Lafond. How predictable is technological progress? *Research Policy* **45,** 647–665 (2016).

13. IRENA. *IRENA REthinking Energy* tech. rep. 2 (IRENA – The International Renewable Energy AgencyInternational, 2015).

14. W. Shockley & H. J. Queisser. Detailed Balance Limit of Efficiency of p-n Junction Solar Cells. *Journal of Applied Physics* **32,** 510–519 (1961).

15. A. D. Vos. Detailed balance limit of the efficiency of tandem solar cells. *Journal of Physics D: Applied Physics* **13,** 839 (1980).

16. A. Martí & G. L. Araújo. Limiting efficiencies for photovoltaic energy conversion in multigap systems. *Solar Energy Materials and Solar Cells* **43,** 203–222 (1996).

17. W. Shockley & W. T. Read. Statistics of the Recombinations of Holes and Electrons. *Physical Review* **87,** 835–842 (1952).

18. R. N. Hall. Electron-Hole Recombination in Germanium. *Physical Review* **87,** 387–387 (1952).

19. P. Auger. Sur les rayons beta; secondaires produits dans un gaz par des rayons X. *C.R.A.S.* **177,** 169–171 (1923).

20. E. Yablonovitch. Statistical ray optics. *Journal of the Optical Society of America* **72,** 899–907 (1982).

21. M. A. Green. Lambertian light trapping in textured solar cells and light-emitting diodes: analytical solutions. *Progress in Photovoltaics: Research and Applications* **10,** 235–241 (2002).

22. Z. Yu, A. Raman & S. Fan. Fundamental limit of nanophotonic light trapping in solar cells. *Proceedings of the National Academy of Sciences* **107,** 17491–17496 (2010).

23. E. Yablonovitch. Inhibited Spontaneous Emission in Solid-State Physics and Electronics. *Physical Review Letters* **58,** 2059–2062 (1987).

24. S. John. Strong localization of photons in certain disordered dielectric superlattices. *Physical Review Letters* **58,** 2486–2489 (1987).

25. J. D. Joannopoulos, R. D. Meade & J. N. Winn. *Photonic Crystals: Molding the Flow of Light* (Princeton University Press, 1995).

26. T. F. Krauss. Slow Light in Photonic Crystal Waveguides. *Journal of Physics D: Applied Physics* **40,** 2666–2670 (2007).

27. T. Baba. Slow Light in Photonic Crystals. *Nature Photonics* **2,** 465–473 (2008).

28. C. Wiesmann, K. Bergenek, N. Linder & U. Schwarz. Photonic crystal LEDs - designing light extraction. *Laser & Photonics Review* **3,** 262–286 (2009).

29. H. Soda, K.-i. Iga, C. Kitahara & Y. Suematsu. GaInAsP/InP Surface Emitting Injection Lasers. *Japanese Journal of Applied Physics* **18,** 2329 (1979).

30. O. Painter, J. Vučkovič & A. Scherer. Defect modes of a two-dimensional photonic crystal in an optically thin dielectric slab. *Journal of the Optical Society of America B* **16,** 275–285 (1999).

31. S. Zanotto, M. Liscidini & L. C. Andreani. Light trapping regimes in thin-film silicon solar cells with a photonic pattern. *Optics Express* **18,** 4260–4274 (2010).

32. Y. Park, E. Drouard, O. El Daif, X. Letartre, P. Viktorovitch, A. Fave, A. Kaminski, M. Lemiti & C. Seassal. Absorption enhancement using photonic crystals for silicon thin film solar cells. *Optics Express* **17,** 14312–14321 (2009).

33. K. Q. Le, A. Abass, B. Maes, P. Bienstman & A. Alù. Comparing Plasmonic and Dielectric ratings for Absorption Enhancement in Thin-Film Organic Solar Cells. *Optics Express* **20,** A39–A50 (2012).

34. A. Bozzola, M. Liscidini & L. C. Andreani. Photonic light-trapping versus Lambertian limits in thin film silicon solar cells with 1D and 2D periodic patterns. *Optics Express* **20,** A224–A244 (S2 2012).

35. N. Huang, C. Lin & M. L. Povinelli. Broadband absorption of semiconductor nanowire arrays for photovoltaic applications. *Journal of Optics* **14,** 024004 (2012).

36. L. C. Andreani, A. Bozzola, P. Kowalczewski & M. Liscidini. Photonic light trapping and electrical transport in thin-film silicon solar cells. *Solar Energy Materials and Solar Cells. EMRS 2014 Spring Meeting – Advanced materials and characterization techniques for solar cells II* **135,** 78–92 (2015).

37. J. Eisenlohr, N. Tucher, H. Hauser, M. Graf, J. Benick, B. Bläsi, J. C. Goldschmidt & M. Hermle. Efficiency Increase of Crystalline Silicon Solar Cells with Nanoimprinted Rear Side Gratings for Enhanced Light Trapping. *Solar Energy Materials and Solar Cells* **155,** 288–293 (2016).

38. M. Hussein, M. F. O. Hameed, N. F. F. Areed, A. Yahia & S. S. A. Obayya. Funnel-shaped silicon nanowire for highly efficient light trapping. *Optics Letters* **41,** 1010 (2016).

39. D. Maystre. in *Plasmonics* (eds S. Enoch & N. Bonod) (Springer Berlin Heidelberg, Berlin, Heidelberg, 2012).

40. H.-P. Wang, K.-T. Tsai, K.-Y. Lai, T.-C. Wei, Y.-L. Wang & J.-H. He. Periodic Si nanopillar arrays by anodic aluminum oxide template and catalytic etching for broadband and omnidirectional light harvesting. *Optics Express* **20,** A94–A103 (S1 2012).

41. K. X. Wang, Z. Yu, V. Liu, A. Raman, Y. Cui & S. Fan. Light trapping in photonic crystals. *Energy & Environmental Science* **7,** 2725–2738 (2014).

42. O. Gunawan, K. Wang, B. Fallahazad, Y. Zhang, E. Tutuc & S. Guha. High performance wire-array silicon solar cells. *Progress in Photovoltaics: Research and Applications* **19,** 307–312 (2010).

43. D. Zhou & R. Biswas. Photonic crystal enhanced light-trapping in thin film solar cells. *Journal of Applied Physics* **103,** 093102 (2008).

44. Y. Lu & A. Lal. High-Efficiency Ordered Silicon Nano-Conical-Frustum Array Solar Cells by Self-Powered Parallel Electron Lithography. *Nano Letters* **10,** 4651–4656 (2010).

45. K. X. Wang, Z. Yu, V. Liu, Y. Cui & S. Fan. Absorption Enhancement in Ultrathin Crystalline Silicon Solar Cells with Antireflection and Light-Trapping Nanocone Gratings. *Nano Letters* **12,** 1616–1619 (2012).

46. J. Tommila, A. Aho, A. Tukiainen, V. Polojärvi, J. Salmi, T. Niemi & M. Guina. Moth-eye antireflection coating fabricated by nanoimprint lithography on 1 eV dilute nitride solar cell. *Progress in Photovoltaics: Research and Applications* **21,** 1158–1162 (2013).

47. J. Tommila, V. Polojärvi, A. Aho, A. Tukiainen, J. Viheriälä, J. Salmi, A. Schramm, J. Kontio, A. Turtiainen, T. Niemi & M. Guina. Nanostructured broadband antireflection coatings on AlInP fabricated by nanoimprint lithography. *Solar Energy Materials and Solar Cells* **94,** 1845–1848 (2010).

48. I. Prieto, B. Galiana, P. A. Postigo, C. Algora, L. J. Martínez & I. Rey-Stolle. Enhanced quantum efficiency of Ge solar cells by a two-dimensional photonic crystal nanostructured surface. *Applied Physics Letters* **94,** 191102 (2009).

49. C.-M. Hsu, S. T. Connor, M. X. Tang & Y. Cui. Wafer-Scale Silicon Nanopillars and Nanocones by Langmuir–Blodgett Assembly and Etching. *Applied Physics Letters* **93,** 133109 (2008).

50. S. Basu Mallick, M. Agrawal, A. Wangperawong, E. S. Barnard, K. K. Singh, R. J. Visser, M. L. Brongersma & P. Peumans. Ultrathin Crystalline-Silicon Solar Cells with Embedded Photonic Crystals. *Applied Physics Letters* **100,** (2012).

51. A. Bozzola, M. Liscidini & L. C. Andreani. Broadband Light Trapping with Disordered Photonic Structures in Thin-Film Silicon Solar Cells. *Progress in Photovoltaics: Research and Applications* **22,** 1237–1245 (2014).

52. Y. Shi, X. Wang & F. Yang. Disorder Improves Light Absorption in Thin Film Silicon Solar Cells with Hybrid Light Trapping Structure. *International Journal of Optics* **2016,** e9371608 (2016).

53. C. Trompoukis, I. Massiot, V. Depauw, O. El Daif, K. Lee, A. Dmitriev, I. Gordon, R. Mertens & J. Poortmans. Disordered nanostructures by hole-mask colloidal lithography for advanced light trapping in silicon solar cells. *Optics Express* **24,** A191 (2016).

54. E. R. Martins, J. Li, Y. Liu, V. Depauw, Z. Chen, J. Zhou & T. F. Krauss. Deterministic quasi-random nanostructures for photon control. *Nature Communications* **4** (2013).

55. K. Vynck, M. Burresi, F. Riboli & D. S. Wiersma. Photon Management in Two-Dimensional Disordered Media. *Nature Materials* **11,** 1017–1022 (2012).

56. S. A. Boden & D. M. Bagnall. Optimization of moth-eye antireflection schemes for silicon solar cells. *Progress in Photovoltaics: Research and Applications* **18,** 195–203 (2010).

57. A. Mellor, I. Tobías, A. Martí, M. Mendes & A. Luque. Upper limits to absorption enhancement in thick solar cells using diffraction gratings. *Progress in Photovoltaics: Research and Applications* **19,** 676–687 (2011).

58. Z. Fan, H. Razavi, J.-w. Do, A. Moriwaki, O. Ergen, Y.-L. Chueh, P. W. Leu, J. C. Ho, T. Takahashi, L. A. Reichertz, S. Neale, K. Yu, M. Wu, J. W. Ager & A. Javey. Three-Dimensional Nanopillar-Array Photovoltaics on Low-Cost and Flexible Substrates. *Nature Materials* **8,** 648–653 (2009).

59. R. Biswas, J. Bhattacharya, B. Lewis, N. Chakravarty & V. Dalal. Enhanced nanocrystalline silicon solar cell with a photonic crystal back-reflector. *Solar Energy Materials and Solar Cells* **94,** 2337–2342 (2010).

60. A. P. Vasudev, J. A. Schuller & M. L. Brongersma. Nanophotonic light trapping with patterned transparent conductive oxides. *Optics Express* **20,** A385–A394 (S3 2012).

61. E. E. Perl, W. E. McMahon, J. E. Bowers & D. J. Friedman. Design of antireflective nanostructures and optical coatings for next-generation multijunction photovoltaic devices. *Optics Express* **22,** A1243 (S5 2014).

62. E. E. Perl, W. E. McMahon, R. M. Farrell, S. P. DenBaars, J. S. Speck & J. E. Bowers. Surface Structured Optical Coatings with Near-Perfect Broadband and Wide-Angle Antireflective Properties. *Nano Letters* **14,** 5960–5964 (2014).

63. C.-H. Sun, B. J. Ho, B. Jiang & P. Jiang. Biomimetic subwavelength antireflective gratings on GaAs. *Optics Letters* **33,** 2224–2226 (2008).

64. Y. M. Song, Y. Jeong, C. I. Yeo & Y. T. Lee. Enhanced power generation in concentrated photovoltaics using broadband antireflective coverglasses with moth eye structures. *Optics Express* **20,** A916–A923 (S6 2012).

65. K.-S. Han, J.-H. Shin, W.-Y. Yoon & H. Lee. Enhanced performance of solar cells with anti-reflection layer fabricated by nano-imprint lithography. *Solar Energy Materials and Solar Cells* **95,** 288–291 (2011).

66. E. S. Román, A. Vitrey, J. Buencuerpo, I. Fernández, I. Prieto, B. Alén, A. García-Martín, J. M. Llorens, S. R. J. Brueck & J. M. Ripalda. High transmission nanowire contact arrays with subwavelength spacing. *physica status solidi (RRL) – Rapid Research Letters* **10,** 164–167 (2016).

67. E. San Román, A. Vitrey, J. Buencuerpo, I. Prieto, J. M. Llorens, A. García-Martín, B. Alén, A. Chaudhuri, A. Neumann, S. R. J. Brueck & et al. Cloaking of solar cell contacts at the onset of Rayleigh scattering. *Scientific Reports* **6,** 28669 (2016).

68. J. Buencuerpo, J. M. Llorens, M. L. Dotor & J. M. Ripalda. Photon management with nanostructures on concentrator solar cells. *Applied Physics Letters* **103,** 083901–083901 (2013).

69. J. Buencuerpo, J. M. Llorens, M. L. Dotor & J. M. Ripalda. Broadband antireflective nano-cones for tandem solar cells. *Optics Express* **23,** A322 (2015).

70. X. Yan, D. J. Poxson, J. Cho, R. E. Welser, A. K. Sood, J. K. Kim & E. F. Schubert. Enhanced Omnidirectional Photovoltaic Performance of Solar Cells Using Multiple-Discrete-Layer Tailored- and Low-Refractive Index Anti-Reflection Coatings. *Advanced Functional Materials* **23,** 583–590 (2013).

71. P. Pignalosa, H. Lee, L. Qiao, M. Tseng & Y. Yi. Graded index and randomly oriented core-shell silicon nanowires for broadband and wide angle antireflection. *AIP Advances* **1,** 032124 (2011).

72. M. Otto, M. Algasinger, H. Branz, B. Gesemann, T. Gimpel, K. Füchsel, T. Käsebier, S. Kontermann, S. Koynov, X. Li, V. Naumann, J. Oh, A. N. Sprafke, J. Ziegler, M. Zilk & R. B. Wehrspohn. Black Silicon Photovoltaics. *Advanced Optical Materials* **3,** 147–164 (2015).

73. H. A. MacLeod. *Thin-Film Optical Filters, Third Edition* 682 pp. (CRC Press, 2001).

74. S. Kurtz & J. Geisz. Multijunction solar cells for conversion of concentrated sunlight to electricity. *Optics Express* **18,** A73–A78 (S1 2010).

75. W. H. Southwell. Gradient-index antireflection coatings. *Optics Letters* **8,** 584–586 (1983).

76. E. B. Grann, M. G. Moharam & D. A. Pommet. Optimal design for antireflective tapered two-dimensional subwavelength grating structures. *Journal of the Optical Society of America A* **12,** 333–339 (1995).

77. 4859280 (1989).

78. P. Campbell & M. A. Green. Light trapping properties of pyramidally textured surfaces. *Journal of Applied Physics* **62,** 243–249 (1987).

79. J. Zhao, A. Wang, M. A. Green & F. Ferrazza. 19.8% efficient "honeycomb" textured multicrystalline and 24.4% monocrystalline silicon solar cells. *Applied Physics Letters* **73,** 1991 (1998).

80. E. B. Grann, M. G. Moharam & D. A. Pommet. Artificial uniaxial and biaxial dielectrics with use of two-dimensional subwavelength binary gratings. *Journal of the Optical Society of America A* **11,** 2695–2703 (1994).

81. S. G. Tikhodeev, A. L. Yablonskii, E. A. Muljarov, N. A. Gippius & T. Ishihara. Quasiguided modes and optical properties of photonic crystal slabs. *Physical Review B* **66,** 045102 (2002).

82. M. A. Green, K. Emery, Y. Hishikawa, W. Warta & E. D. Dunlop. Solar cell efficiency tables (version 39). *Progress in Photovoltaics: Research and Applications* **20,** 12–20 (2012).

83. L. Hu & G. Chen. Analysis of Optical Absorption in Silicon Nanowire Arrays for Photovoltaic Applications. *Nano Letters* **7,** 3249–3252 (2007).

84. J. Buencuerpo, L. E. Munioz-Camuniez, M. L. Dotor & P. A. Postigo. Optical absorption enhancement in a hybrid system photonic crystal-thin substrate for photovoltaic applications. *Optics Express* **20,** A452–A464 (S4 2012).

85. G. L. Araújo & A. Martí. Absolute limiting efficiencies for photovoltaic energy conversion. *Solar Energy Materials and Solar Cells* **33,** 213–240 (1994).

86. M. Li, Z. Y. Li, K.-M. Ho, J. R. Cao & M. Miyawaki. High-efficiency calculations for three-dimensional photonic crystal cavities. *Optics Letters* **31,** 262–264 (2006).

87. M. Li, X. Hu, Z. Ye, K.-M. Ho, J. Cao & M. Miyawaki. Higher-order incidence transfer matrix method used in three-dimensional photonic crystal coupled-resonator array simulation. *Optics Letters* **31,** 3498–3500 (2006).

88. E. D. Palik. *Handbook of optical constants of solids II* 1117 pp. (Academic Press, 1991).

89. M. J. D. Powell. Direct search algorithms for optimization calculations. *Acta Numerica* **7,** 287–336 (1998).

90. J. E. Lugo, J. A. del Rio & J. Tagüeña-Martínez. Influence of surface coverage on the effective optical properties of porous silicon modeled as a Si-wire array. *Journal of Applied Physics* **81,** 1923–1928 (1997).

91. O. D. Miller, E. Yablonovitch & S. R. Kurtz. Strong Internal and External Luminescence as Solar Cells Approach the Shockley #x2013;Queisser Limit. *IEEE Journal of Photovoltaics* **2,** 303–311 (2012).

92. D. Ding, S. R. Johnson, S.-Q. Yu, S.-N. Wu & Y.-H. Zhang. A semi-analytical model for semiconductor solar cells. *Journal of Applied Physics* **110,** 123104 (2011).

93. J. M. Olson, D. J. Friedman & S. Kurtz. in *Handbook of Photovoltaic Science and Engineering* (eds A. Luque, S. Hegedus, A. Luque & S. Hegedus) 375–377 (Wiley, 2003).

94. C. Algora & V. Díaz. Modelling of GaAs solar cells under wide angle cones of homogeneous light. *Progress in Photovoltaics: Research and Applications* **7,** 379–386 (1999).

95. M. Victoria, C. Domínguez, I. Antón & G. Sala. Antireflective coatings for multijunction solar cells under wide-angle ray bundles. *Optics Express* **20,** 8136–8147 (2012).

96. S.-Y. Lien, D.-S. Wuu, W.-C. Yeh & J.-C. Liu. Tri-layer antireflection coatings (SiO2/SiO2–TiO2/TiO2) for silicon solar cells using a sol–gel technique. *Solar Energy Materials and Solar Cells* **90,** 2710–2719 (2006).

97. J.-Q. Xi, M. F. Schubert, J. K. Kim, E. F. Schubert, M. Chen, S.-Y. Lin, W. Liu & J. A. Smart. Optical thin-film materials with low refractive index for broadband elimination of Fresnel reflection. *Nature Photonics* **1,** 176–179 (2007).

98. P. Yeh. *Optical Waves in Layered Media* 428 pp. (Wiley, 2005).

99. J. W. Leem, J. Su Yu, D.-H. Jun, J. Heo & W.-K. Park. Efficiency improvement of III–V GaAs solar cells using biomimetic TiO2 subwavelength structures with wide-angle and broadband antireflection properties. *Solar Energy Materials and Solar Cells* **127,** 43–49 (2014).

100. M.-M. Hung, H.-V. Han, C.-Y. Hong, K.-H. Hong, T.-T. Yang, P. Yu, Y.-R. Wu, H.-Y. Yeh & H.-C. Huang. Compound biomimetic structures for efficiency enhancement of $Ga_{0.5}In_{0.5}P$/GaAs/Ge triple-junction solar cells. *Optics Express* **22,** A295–A300 (2014).

101. V. Liu & S. Fan. S4 : A free electromagnetic solver for layered periodic structures. *Computer Physics Communications* **183,** 2233–2244 (2012).

102. F. Dimroth, M. Grave, P. Beutel, U. Fiedeler, C. Karcher, T. N. D. Tibbits, E. Oliva, G. Siefer, M. Schachtner, A. Wekkeli, A. W. Bett, R. Krause, M. Piccin, N. Blanc, C. Drazek, E. Guiot, B. Ghyselen, T. Salvetat, A. Tauzin, T. Signamarcheix, A. Dobrich, T. Hannappel & K. Schwarzburg. Wafer bonded four-junction GaInP/GaAs//GaInAsP/GaInAs concentrator solar cells with 44.7% efficiency. *Progress in Photovoltaics: Research and Applications* **22,** 277–282 (2014).

103. *Solar Spectral Irradiance: ASTM G-173* http://rredc.nrel.gov/solar/spectra/am1.5/.

104. H. Kato, S. Adachi, H. Nakanishi & K. Ohtsuka. Optical Properties of (AlxGa1-x)0.5In0.5P Quaternary Alloys. *Japanese Journal of Applied Physics* **33,** 186 (1994).

105. S. Tanemura, L. Miao, P. Jin, K. Kaneko, A. Terai & N. Nabatova-Gabain. Optical properties of polycrystalline and epitaxial anatase and rutile TiO2 thin films by rf magnetron sputtering. *Applied Surface Science* **212–213,** 654–660 (2003).

106. *Ioffe Institute, n,k database* http://www.ioffe.ru/SVA/NSM/nk/index.html.

107. Y. Zhang, C. Li & M. Loncar. Optimal broadband antireflective taper. *Optics Letters* **38,** 646–648 (2013).

108. W. L. Price. Global optimization by controlled random search. *Journal of Optimization Theory and Applications* **40,** 333–348 (1983).

109. *NLopt - AbInitio* http://ab-initio.mit.edu/wiki/index.php/NLopt.

110. J. van de Groep & A. Polman. Designing dielectric resonators on substrates: Combining magnetic and electric resonances. *Optics Express* **21,** 26285 (2013).

111. S. Giordano. Effective medium theory for dispersions of dielectric ellipsoids. *Journal of Electrostatics* **58,** 59–76 (2003).

112. S. Fan & J. D. Joannopoulos. Analysis of guided resonances in photonic crystal slabs. *Physical Review B* **65,** 235112 (2002).

113. R. Fuchs, K. L. Kliewer & W. J. Pardee. Optical Properties of an Ionic Crystal Slab. *Physical Review* **150,** 589–596 (1966).

114. S. L. Diedenhofen, G. Grzela, E. Haverkamp, G. Bauhuis, J. Schermer & J. G. Rivas. Broadband and omnidirectional anti-reflection layer for III/V multi-junction solar cells. *Solar Energy Materials and Solar Cells* **101,** 308–314 (2012).

115. R. Dewan, S. Fischer, V. B. Meyer-Rochow, Y. Özdemir, S. Hamraz & D. Knipp. Studying nanostructured nipple arrays of moth eye facets helps to design better thin film solar cells. *Bioinspiration & Biomimetics* **7,** 016003 (2012).

116. R. Sanatinia, K. M. Awan, S. Naureen, N. Anttu, E. Ebraert & S. Anand. GaAs nanopillar arrays with suppressed broadband reflectance and high optical quality for photovoltaic applications. *Optical Materials Express* **2,** 1671–1679 (2012).

117. K.-C. Park, H. J. Choi, C.-H. Chang, R. E. Cohen, G. H. McKinley & G. Barbastathis. Nanotextured Silica Surfaces with Robust Superhydrophobicity and Omnidirectional Broadband Supertransmissivity. *ACS Nano* **6,** 3789–3799 (2012).

118. S. Ji, K. Song, T. B. Nguyen, N. Kim & H. Lim. Optimal Moth Eye Nanostructure Array on Transparent Glass Towards Broadband Antireflection. *ACS Applied Materials & Interfaces* (2013).

119. F. L. Gonzalez, D. E. Morse & M. J. Gordon. Importance of diffuse scattering phenomena in moth-eye arrays for broadband infrared applications. *Optics Letters* **39,** 13–16 (2014).

120. E. E. Perl, C.-T. Lin, W. E. McMahon, D. J. Friedman & J. E. Bowers. Ultrabroadband and Wide-Angle Hybrid Antireflection Coatings With Nanostructures. *IEEE Journal of Photovoltaics* **4,** 962–967 (2014).

121. S. Chattopadhyay, Y. Huang, Y. Jen, A. Ganguly, K. Chen & L. Chen. Anti-reflecting and photonic nanostructures. *Materials Science and Engineering: R: Reports* **69,** 1–35 (2010).

122. Y. Da & Y. Xuan. Role of surface recombination in affecting the efficiency of nanostructured thin-film solar cells. *Optics Express* **21,** A1065 (S6 2013).

123. D. Xia, Z. Ku, S. C. Lee & S. R. J. Brueck. Nanostructures and Functional Materials Fabricated by Interferometric Lithography. *Advanced Materials* **23,** 147–179 (2011).

124. B. Bläsi & H. Hauser. Large-area patterning using interference and nanoimprint lithography. *SPIE Newsroom* (2016).

125. J. A. van Delft, D. Garcia-Alonso & W. M. M. Kessels. Atomic layer deposition for photovoltaics: applications and prospects for solar cell manufacturing. *Semiconductor Science and Technology* **27,** 074002 (2012).

126. P. R. Chalker, P. A. Marshall, S. Romani, J. W. Roberts, S. J. C. Irvine, D. A. Lamb, A. J. Clayton & P. A. Williams. Atomic layer deposition of Ga-doped ZnO transparent conducting oxide substrates for CdTe-based photovoltaics. *Journal of Vacuum Science & Technology A: Vacuum, Surfaces, and Films* **31,** 01A120 (2013).

127. A. C. Jones & P. R. Chalker. Some recent developments in the chemical vapour deposition of electroceramic oxides. *Journal of Physics D: Applied Physics* **36,** R80 (2003).

128. H. Nagel, A. G. Aberle & R. Hezel. Optimised antireflection coatings for planar silicon solar cells using remote PECVD silicon nitride and porous silicon dioxide. *Progress in Photovoltaics: Research and Applications* **7,** 245–260 (1999).

129. L. Dobrzański, M. Szindler, A. Drygała & M. Szindler. Silicon solar cells with Al2O3 antireflection coating. *Open Physics* **12** (2014).

130. S. M. George. Atomic Layer Deposition: An Overview. *Chemical Reviews* **110,** 111–131 (2010).

131. A. K. Katiyar, S. Mukherjee, M. Zeeshan, S. K. Ray & A. K. Raychaudhuri. Enhancement of Efficiency of a Solar Cell Fabricated on Black Si Made by Inductively Coupled Plasma-Reactive Ion Etching Process: A Case Study of a n-CdS/p-Si Heterojunction Cell. *ACS Applied Materials & Interfaces* **7,** 23445–23453 (2015).

132. M. Shearn, X. Sun, M. D. Henry, A. Yariv & A. Scherer. *Advanced plasma processing: etching, deposition, and wafer bonding techniques for semiconductor applications* (Intech, 2010).

133. S. H. Zaidi, D. S. Ruby & J. M. Gee. Characterization of random reactive ion etched-textured silicon solar cells. *IEEE Transactions on Electron Devices* **48,** 1200–1206 (2001).

134. P. N. K. Deenapanray, C. S. Athukorala, D. Macdonald, W. E. Jellett, E. Franklin, V. E. Everett, K. J. Weber & A. W. Blakers. Reactive ion etching of dielectrics and silicon for photovoltaic applications. *Progress in Photovoltaics: Research and Applications* **14,** 603–614 (2006).

135. Q. Xie, M. H. Hong, H. L. Tan, G. X. Chen, L. P. Shi & T. C. Chong. Fabrication of nanostructures with laser interference lithography. *Journal of Alloys and Compounds* **449,** 261–264 (2008).

136. Y. X. Li, P. J. French & R. F. Wolffenbuttel. Selective reactive ion etching of silicon nitride over silicon using CHF3 with N2 addition. *Journal of Vacuum Science & Technology B* **13,** 2008–2012 (1995).

137. M. Schubert, V. Gottschalch, C. M. Herzinger, H. Yao, P. G. Snyder & J. A. Woollam. Optical constants of GaxIn1-xP lattice matched to GaAs. *Journal of Applied Physics* **77,** 3416–3419 (1995).

138. M. Burresi, F. Pratesi, K. Vynck, M. Prasciolu, M. Tormen & D. S. Wiersma. Two-Dimensional Disorder for Broadband, Omnidirectional and Polarization-Insensitive Absorption. *Optics Express* **21,** A268–A275 (2013).

139. H. Ding, L. Lalouat, B. Gonzalez-Acevedo, R. Orobtchouk, C. Seassal & E. Drouard. Design Rules for Net Absorption Enhancement in Pseudo-Disordered Photonic Crystal for Thin Film Solar Cells. *Optics Express* **24,** A650 (2016).

140. J. Buencuerpo, J. M. Llorens, P. Zilio, W. Raja, J. Cunha, A. Alabastri, R. P. Zaccaria, A. Martí & T. Versloot. Light-trapping in photon enhanced thermionic emitters. *Optics Express* **23,** A1220 (2015).

141. C. Zimmermann, C. Nömayr, W. Köstler, A. Caon, E. Fernández, C. Baur & H. Fiebrich. *Photovoltaic technology development for the Bepi Colombo mission* in *Proceedings of the 9th European Space Power Conference, Saint Raphaël, France* (2011).

142. V. Kuznetsov. Solar and heliospheric space missions. *Advances in Space Research* **55.** Cosmic Magnetic Fields, 879–885 (2015).

143. J. W. Schwede, I. Bargatin, D. C. Riley, B. E. Hardin, S. J. Rosenthal, Y. Sun, F. Schmitt, P. Pianetta, R. T. Howe, Z.-X. Shen & N. A. Melosh. Photon-enhanced thermionic emission for solar concentrator systems. *Nature Materials* **9,** 762–767 (2010).

144. A. F. Ioffe. *Semiconductor Thermoelements and Thermoelectric Cooling* (Infosearch, London, 1957).

145. H. J. Goldsmid. *Introduction to Thermoelectricity* (Springer Berlin Heidelberg, 2010).

146. G. Hatsopoulos & E. Gyphtopoulos. *Thermionic Energy Conversion: Theory, technology and application* **v. 2** (MIT Press, 1979).

147. K. Reck & O. Hansen. Thermodynamics of photon-enhanced thermionic emission solar cells. *Applied Physics Letters* **104,** 023902 (2014).

148. G. Segev, Y. Rosenwaks & A. Kribus. Limit of efficiency for photon-enhanced thermionic emission vs. photovoltaic and thermal conversion. *Sol. Energ. Mat. Sol. Cells* **140,** 464–476 (2015).

149. S. Sze. *Physics of Semiconductor Devices* 2nd (Wiley, New York, USA, 1981).

150. J. M. Olson, R. K. Ahrenkiel, D. J. Dunlavy, B. Keyes & A. E. Kibbler. Ultralow recombination velocity at Ga0.5In0.5P/GaAs heterointerfaces. *Applied Physics Letters* **55,** 1208–1210 (1989).

151. W. Tang, W. Yang, Y. Yang, C. Sun & Z. Cai. GaAs film for photon-enhanced thermionic emission solar harvesters. *Materials Science in Semiconductor Processing. Special topical issue on Materials for Green Energy and the Environment* **25,** 143–147 (2014).

152. J. W. Schwede, T. Sarmiento, V. K. Narasimhan, S. J. Rosenthal, D. C. Riley, F. Schmitt, I. Bargatin, K. Sahasrabuddhe, R. T. Howe, J. S. Harris, N. A. Melosh & Z.-X. Shen. Photon-enhanced thermionic emission from heterostructures with low interface recombination. *Nature Communications* **4,** 1576 (2013).

153. A. Varpula & M. Prunnila. Diffusion-emission theory of photon enhanced thermionic emission solar energy harvesters. *Journal of Applied Physics* **112,** 044506 (2012).

154. A. Varpula, K. Tappura & M. Prunnila. Si, GaAs, and InP as cathode materials for photon-enhanced thermionic emission solar cells. *Solar Energy Materials and Solar Cells* **134,** 351–358 (2015).

155. K. Sahasrabuddhe, J. W. Schwede, I. Bargatin, J. Jean, R. T. Howe, Z.-X. Shen & N. A. Melosh. A model for emission yield from planar photocathodes based on photon-enhanced thermionic emission or negative-electron-affinity photoemission. *Journal of Applied Physics* **112,** 094907 (2012).

156. G. Segev, A. Kribus & Y. Rosenwaks. High performance isothermal photo-thermionic solar converters. *Sol. Energ. Mat. Sol. Cells* **113,** 114–123 (2013).

157. G. Segev, Y. Rosenwaks & A. Kribus. Loss mechanisms and back surface field effect in photon enhanced thermionic emission converters. *Journal of Applied Physics* **114,** 044505 (2013).

158. G. Segev, Y. Rosenwaks & A. Kribus. Efficiency of photon enhanced thermionic emission solar converters. *Solar Energy Materials and Solar Cells* **107,** 125–130 (2012).

159. Wolfram Research, Inc. *Mathematica 10.0* 2014.

160. S. Su, Y. Wang, T. Liu, G. Su & J. Chen. Space charge effects on the maximum efficiency and parametric design of a photon-enhanced thermionic solar cell. *Sol. Energ. Mat. Sol. Cells* **121,** 137–143 (2014).

161. S. Adachi. *Properties of Group-IV, III-V and II-VI Semiconductors* (Wiley, 2005).

162. V. L. Berkovits, D. Paget, A. N. Karpenko, V. P. Ulin & O. E. Tereshchenko. Soft Nitridation of GaAs(100) by Hydrazine Sulfide Solutions: Effect on Surface Recombination and Surface Barrier. *Applied Physics Letters* **90,** 022104 (2007).

163. S. E. Han & G. Chen. Toward the Lambertian Limit of Light Trapping in Thin Nanostructured Silicon Solar Cells. *Nano Letters* **10,** 4692–4696 (2010).

164. B. C. P. Sturmberg, K. B. Dossou, L. C. Botten, A. A. Asatryan, C. G. Poulton, R. C. McPhedran & C. Martijn de Sterke. Nanowire array photovoltaics: Radial disorder versus design for optimal efficiency. *Applied Physics Letters* **101,** (2012).

165. J. M. Llorens, J. Buencuerpo & P. A. Postigo. Absorption features of the zero frequency mode in an ultra-thin slab. *Applied Physics Letters* **105,** 231115 (2014).

166. J.-H. Lee, I. Bargatin, N. A. Melosh & R. T. Howe. Optimal emitter-collector gap for thermionic energy converters. *Applied Physics Letters* **100,** 173904 (2012).

167. Z. A. Ibrahim, A. I. Shkrebtii, M. J. G. Lee, K. Vynck, T. Teatro, W. Richter, T. Trepk & T. Zettler. Temperature dependence of the optical response: Application to bulk GaAs using first-principles molecular dynamics simulations. *Physical Review B* **77,** 125218 (2008).

168. A. I. Shkrebtii, Z. A. Ibrahim, T. Teatro, W. Richter, M. J. Lee & L. Henderson. Theory of the temperature dependent dielectric function of semiconductors: from bulk to surfaces. Application to GaAs and Si. *Physical status solidi (b)* **247,** 1881–1888 (2010).

169. S. Adachi. Excitonic effects in the optical spectrum of GaAs. *Physical Review B* **41,** 1003–1013 (1990).

170. I. Langmuir. The effect of space charge and initial velocities on the potential distribution and thermionic current between parallel plane electrodes. *Physical Review* **21,** 419–435 (1923).

171. Y. Yang, W. Yang, W. Tang & C. Sun. High-temperature solar cell for concentrated solar-power hybrid systems. *Applied Physics Letters* **103,** 083902 (2013).

172. R. Raffaelle & S. Bailey. in *Handbook of Photovoltaic Science and Engineering* (eds A. Luque & S. Hegedus) 413–446 (Wiley, Hoboken, NJ, 2003).

173. N. S. Fatemi, H. E. Pollard, H. Q. Hou & P. R. Sharps. *Solar array trades between very high-efficiency multi-junction and Si space solar cells* in *Photovoltaic Specialists Conference, 2000. Conference Record of the Twenty-Eighth IEEE* (2000), 1083–1086.

174. N. D. Lai, W. P. Liang, J. H. Lin, C. C. Hsu & C. H. Lin. Fabrication of Two- and Three-Dimensional Periodic Structures by Multi-Exposure of Two-Beam Interference Technique. *Optics Express* **13,** 9605–9611 (2005).

175. J. de Boor, N. Geyer, U. Gösele & V. Schmidt. Three-Beam Interference Lithography: Upgrading a Lloyd's Interferometer for Single-Exposure Hexagonal Patterning. *Optics Letters* **34,** 1783–1785 (2009).

176. X. Zhang, M. Theuring, Q. Song, W. Mao, M. Begliarbekov & S. Strauf. Holographic Control of Motive Shape in Plasmonic Nanogap Arrays. *Nano Letters* **11,** 2715–2719 (2011).

177. B. Bläsi, H. Hauser, O. Höhn, V. Kübler, M. Peters & A. J. Wolf. Photon Management Structures Originated by Interference Lithography. *Energy Procedia* **8,** 712–718 (2011).

178. H. van Wolferen & L. Abelmann. in (ed T. C. Hennessy) 133–148 (Nova Science Pub Inc, New York, 2011).

179. C. P. Fucetola, H. Korre & K. K. Berggren. Low-cost interference lithography. *Journal of Vacuum Science & Technology B: Microelectronics and Nanometer Structures* **27,** 2958 (2009).

180. Michael E. Walsh. *On the design of lithographic interferometers and their application .pdf* PhD thesis (Massachusetts Institute of Technology, 2014), 101–130.

181. A. Hassanzadeh, M. Mohammadnezhad & S. Mittler. Multiexposure laser interference lithography. *Journal of Nanophotonics* **9,** 093067–093067 (2015).

182. S. J. McNab & R. J. Blaikie. Contrast in the evanescent near field of $\lambda/20$ period gratings for photolithography. *Applied Optics* **39,** 20–25 (2000).

183. H. Kogelnik. Coupled Wave Theory for Thick Hologram Gratings. *Bell System Technical Journal* **48,** 2909–2947 (1969).

184. F. G. Kaspar. Diffraction by thick, periodically stratified gratings with complex dielectric constant. *Journal of the Optical Society of America* **63,** 37 (1973).

185. K. Knop. Rigorous diffraction theory for transmission phase gratings with deep rectangular grooves. *Journal of the Optical Society of America* **68,** 1206 (1978).

186. M. G. Moharam & T. K. Gaylord. Rigorous coupled-wave analysis of planar-grating diffraction. *Journal of the Optical Society of America* **71,** 811 (1981).

187. M. G. Moharam, T. K. Gaylord, D. A. Pommet & E. B. Grann. Stable implementation of the rigorous coupled-wave analysis for surface-relief gratings: enhanced transmittance matrix approach. *Journal of the Optical Society of America A* **12,** 1077 (1995).

188. R. Bräuer & O. Bryngdahl. Electromagnetic diffraction analysis of two-dimensional gratings. *Optics Communications* **100,** 1–5 (1993).

189. D. M. Whittaker & I. S. Culshaw. Scattering-matrix treatment of patterned multilayer photonic structures. *Physical Review B* **60,** 2610–2618 (1999).

190. L. Li. New formulation of the Fourier modal method for crossed surface-relief gratings. *Journal of the Optical Society of America A* **14,** 2758 (1997).

191. M. Liscidini, D. Gerace, L. C. Andreani & J. E. Sipe. Scattering-matrix analysis of periodically patterned multilayers with asymmetric unit cells and birefringent media. *Physical Review B* **77,** 035324 (2008).

192. B. Caballero, A. García-Martín & J. C. Cuevas. Generalized Scattering-Matrix Approach for Magneto-Optics in Periodically Patterned Multilayer Systems. *Physical Review B* **85,** 245103 (2012).

193. A. García-Martín, G. Armelles & S. Pereira. Light Transport in Photonic Crystals Composed of Magneto-Optically Active Materials. *Physical Review B* **71,** 205116 (2005).

194. E. W. Matthews. The Use of Scattering Matrices in Microwave Circuits. *IRE Transactions on Microwave Theory and Techniques* **3,** 21–26 (1955).

195. K. Kurokawa. Power Waves and the Scattering Matrix. *IEEE Transactions on Microwave Theory and Techniques* **13,** 194–202 (1965).

196. L. Li & C. W. Haggans. Convergence of the coupled-wave method for metallic lamellar diffraction gratings. *Journal of the Optical Society of America A* **10,** 1184 (1993).

197. P. Lalanne & G. M. Morris. Highly improved convergence of the coupled-wave method for TM polarization. *Journal of the Optical Society of America A* **13,** 779 (1996).

198. G. Granet & B. Guizal. Efficient implementation of the coupled-wave method for metallic lamellar gratings in TM polarization. *Journal of the Optical Society of America A* **13,** 1019 (1996).

199. L. Li. Use of Fourier series in the analysis of discontinuous periodic structures. *Journal of the Optical Society of America A* **13,** 1870 (1996).

200. E. Popov & M. Nevière. Maxwell equations in Fourier space: fast-converging formulation for diffraction by arbitrary shaped, periodic, anisotropic media. *Journal of the Optical Society of America A* **18,** 2886 (2001).

201. B. Chernov, M. Nevière & E. Popov. Fast Fourier factorization method applied to modal analysis of slanted lamellar diffraction gratings in conical mountings. *Optics Communications* **194,** 289–297 (2001).

202. P. Boyer, E. Popov, M. Nevière & G. Tayeb. Diffraction theory in TM polarization: application of the fast Fourier factorization method to cylindrical devices with arbitrary cross section. *Journal of the Optical Society of America A* **21,** 2146 (2004).

203. M. Born, E. Wolf, A. B. Bhatia, P. C. Clemmow, D. Gabor, A. R. Stokes, A. M. Taylor, P. A. Wayman & W. L. Wilcock. in *Principles of Optics: Electromagnetic Theory of Propagation, Interference and Diffraction of Light* 7th edition, 54–70 (Cambridge University Press, Cambridge ; New York, 1999).

204. J. B. Pendry. Photonic Band Structures. *Journal of Modern Optics* **41,** 209–229 (1994).

205. D. W. Berreman. Optics in Stratified and Anisotropic Media: 4×4-Matrix Formulation. *Journal of the Optical Society of America* **62,** 502 (1972).

206. Z.-Y. Li & L.-L. Lin. Photonic band structures solved by a plane-wave-based transfer-matrix method. *Physical Review E* **67,** 046607 (2003).

207. L. Li. Formulation and comparison of two recursive matrix algorithms for modeling layered diffraction gratings. *Journal of the Optical Society of America A* **13,** 1024 (1996).

208. R. C. Rumpf. Improved formulation of scattering matrices for semi-analytical methods that is consistent with convention. *Progress In Electromagnetics Research B* **35,** 241–261 (2011).

209. M. G. Moharam & A. B. Greenwell. in (ed F. Wyrowski) 57 (2004).

210. T. Schuster, J. Ruoff, N. Kerwien, S. Rafler & W. Osten. Normal vector method for convergence improvement using the RCWA for crossed gratings. *Journal of the Optical Society of America A* **24,** 2880 (2007).

211. R. Antos. Fourier factorization with complex polarization bases in modeling optics of discontinuous bi-periodic structures. *Optics Express* **17,** 7269 (2009).

212. A. Taflove & S. C. Hagness. *Computational Electrodynamics: The Finite-Difference Time-Domain Method, Third Edition* 3 edition (Artech House, Boston, 2005).

213. J.-M. Jin. *The Finite Element Method in Electromagnetics* 3 edition. English (Wiley-IEEE Press, 2014).

214. G. Veronis, R. W. Dutton & S. Fan. Method for sensitivity analysis of photonic crystal devices. *Optics Letters* **29,** 2288 (2004).

215. J. Chandezon, G. Raoult & D. Maystre. A new theoretical method for diffraction gratings and its numerical application. *Journal of Optics* **11,** 235 (1980).

216. L. Li, J. Chandezon, G. Granet & J.-P. Plumey. Rigorous and efficient grating-analysis method made easy for optical engineers. *Applied Optics* **38,** 304 (1999).

217. A. F. Oskooi, D. Roundy, M. Ibanescu, P. Bermel, J. Joannopoulos & S. G. Johnson. Meep: A flexible free-software package for electromagnetic simulations by the FDTD method. *Computer Physics Communications* **181,** 687–702 (2010).

218. *Lumerical Solutions, Inc. | Optical and photonic design and engineering software products* 2011.

219. M. Besbes, J. P. Hugonin, P. Lalanne, S. van Haver, O. Janssen, A. M. Nugrowati, M. Xu, S. F. Pereira, H. P. Urbach, A. S. van de Nes, P. Bienstman, G. Granet, A. Moreau, S. Helfert, M. Sukharev, T. Seideman, F. I. Baida, B. Guizal & D. Van Labeke. Numerical analysis of a slit-groove diffraction problem. *Journal of the European Optical Society: Rapid Publications* **2** (2007).

220. J.-P. Hugonin, M. Besbes & P. Lalanne. Hybridization of electromagnetic numerical methods through the G-matrix algorithm. *Optics Letters* **33,** 1590–1592 (2008).

221. N. P. Van Der Aa. in *Progress in Industrial Mathematics at ECMI 2004* 99–103 (Springer, 2006).

222. G. Granet, J. Chandezon, J.-P. Plumey & K. Raniriharinosy. Reformulation of the coordinate transformation method through the concept of adaptive spatial resolution Application to trapezoidal gratings. *Journal of the Optical Society of America A* **18,** 2102 (2001).

223. J. Bischoff. *Improved diffraction computation with a hybrid C-RCWA-Method* in *SPIE Advanced Lithography* (International Society for Optics and Photonics, 2009), 72723Y–72723Y.

224. E. Silberstein, P. Lalanne, J.-P. Hugonin & Q. Cao. Use of grating theories in integrated optics. *Journal of the Optical Society of America A* **18,** 2865 (2001).

225. M. Pisarenco, J. Maubach, I. Setija & R. Mattheij. Aperiodic Fourier modal method in contrast-field formulation for simulation of scattering from finite structures. *Journal of the Optical Society of America A* **27,** 2423 (2010).

226. *openTMM 0.0.1 : Python Package Index*

227. K. J. Millman & M. Aivazis. Python for Scientists and Engineers. *Computing in Science Engineering* **13,** 9–12 (2011).

228. S. v. d. Walt, S. C. Colbert & G. Varoquaux. The NumPy Array: A Structure for Efficient Numerical Computation. *Computing in Science Engineering* **13,** 22–30 (2011).

Publications List

The work presented in this thesis is based on the following publications.

1. **J. Buencuerpo**, J. M. Llorens, M. L. Dotor & J. M. Ripalda. Photon management with nanostructures on concentrator solar cells. *Applied Physics Letters* **103,** 083901–083901 (2013).
2. **J. Buencuerpo**, J. M. Llorens, M. L. Dotor & J. M. Ripalda. Broadband antireflective nano-cones for tandem solar cells. *Optics Express* **23,** A322 (2015).
3. **J. Buencuerpo**, J. M. Llorens, P. Zilio, W. Raja, J. Cunha, A. Alabastri, R. P. Zaccaria, A. Martí & T. Versloot. Light-trapping in photon enhanced thermionic emitters. *Optics Express* **23,** A1220 (2015).
4. **J. Buencuerpo**, L. Torné, R. Álvaro, J. Llorens, M. Dotor & J. M. Ripalda. Nanocones for broadband light coupling to high index substrates. *Submitted* (2016).

Other related publications.

5. **J. Buencuerpo**, L. E. Munioz-Camuniez, M. L. Dotor & P. A. Postigo. Optical absorption enhancement in a hybrid system photonic crystal-thin substrate for photovoltaic applications. *Optics Express* **20,** A452–A464 (S4 2012).
6. J. M. Llorens, **J. Buencuerpo** & P. A. Postigo. Absorption features of the zero frequency mode in an ultra-thin slab. *Applied Physics Letters* **105,** 231115 (2014).
7. E. S. Román, A. Vitrey, **J. Buencuerpo**, I. Fernández, I. Prieto, B. Alén, A. García-Martín, J. M. Llorens, S. R. J. Brueck & J. M. Ripalda. High transmission nanowire contact arrays with subwavelength spacing. *physica status solidi (RRL) – Rapid Research Letters* **10,** 164–167 (2016).

8. E. San Román, A. Vitrey, **J. Buencuerpo**, I. Prieto, J. M. Llorens, A. García-Martín, B. Alén, A. Chaudhuri, A. Neumann, S. R. J. Brueck & et al. Cloaking of solar cell contacts at the onset of Rayleigh scattering. *Scientific Reports* **6,** 28669 (2016).
9. E. López, A. Martí, J. M. Llorens, **J. Buencuerpo** & T. Versloot. Optimum Single-Gap Solar Cells for Missions to Mercury. *Journal of Spacecraft and Rockets* **53,** 787–791 (2016).